DESIGN AND IMPLEMENTATION OF AN EXPERIMENTAL AND NUMERICAL FRAMEWORK FOR POWDER RECOATING RESEARCH IN SELECTIVE LASER MELTING

by

2LT Johannes Weinberg, USAF
B.S. Mechanical Engineering, Distinguished Graduate
United States Air Force Academy, 2016

Submitted to the Department of Mechanical Engineering
in Partial Fulfillment of the Requirements for the Degree of
Master of Science in Mechanical Engineering at the
MASSACHUSETTS INSTITUTE OF TECHNOLOGY

June 2018

Signature of Author:

_____

Johannes Weinberg
Department of Mechanical Engineering
May 18, 2018

Certified by:

_____

A. John Hart
Professor of Mechanical Engineering
Thesis Supervisor

Accepted by:

_____

Rohan Abeyaratne
Chairman, Department Committee on Graduate Theses

This page intentionally left blank

Design and Implementation of an Experimental and Numerical Framework for Powder Recoating Research in Selective Laser Melting

by

2LT Johannes Weinberg, USAF

Submitted to the Department of Mechanical Engineering
on May 18, 2018 in Partial Fulfillment of the Requirements
for the Degree of Master of Science in Mechanical Engineering

ABSTRACT

Selective Laser Melting (SLM) of powders remains one of the most captivating methods to additively manufacture fully dense, 3-dimensional metal parts. The process occurs largely in two steps. First a metal powder is spread in a thin layer on a powder bed. Second the powder is radiated by a laser. Most SLM research has focused on the second step, despite the powder bed being the foundation of the lasing process. Research has shown that the powder bed properties, such as packing density and uniformity are key to creating robust SLM parts.

This thesis aims to explore the powder recoating process and establish a framework for research. The thesis focuses on experimental and computational methods to study powder recoating. An instrumented recoater was built with the capability to measure forces and vary important recoating parameters, such as recoating velocity, blade height and blade geometry. The instrumented recoater was then manufactured, assembled, tested and incorporated into an academic SLM testbed. On the computational side, a Discrete Element Method (DEM) code was calibrated to account for the cohesive forces present in SLM powder. Simulations using the code were able to demonstrate the significance of cohesive forces in the powder recoating process and demonstrate the influence of recoating parameters on powder bed properties. The experimental and computational work presented in this thesis lay the foundation for future powder bed research.

Thesis Supervisor: A. John Hart

Title: Professor of Mechanical Engineering

This page intentionally left blank

ACKNOWLEDGEMENTS[1]

I would like to thank my A. John Hart, who served as my thesis supervisor and included me in his lab group (the MechanoSynthesis group) for the past two years. He has a contagious work ethic and sets the standard high. He instills a culture of responsibility, teamwork and excellence.

I would like to thank those at MIT, especially those within the MechanoSynthesis group. They have mentored me and guided me through the academic process. I thank those that I worked with directly on the HAMR team: Nick Dee, Jon Gibbs, Nigamaa Nayakanti, Dan Oropeza and Ryan Penny. I also thank those that I worked with on the computational work: Christoph Meier and Reimar Weißbach.

I would like to thank those at Lincoln Laboratory, especially those within Group 74. They have helped mentor me and have exposed me to the great research that happens at Lincoln Laboratory. I would like to thank Ethan Parsons for supporting me and helping me to bridge the gap between Lincoln Laboratory and MIT.

I am grateful for the United States Air Force for funding me and allowing me to complete this degree. Graduate school has been a period of tremendous growth, which has changed how I approach most problems.

I would like to thank my girlfriend, Heather. She has supported me through the most stressful times of this thesis. She even read through the whole thesis and provided grammar and formatting help.

I would like to thank my friends and family for their support. They have made my time in Boston enjoyable and memorable.

---

[1] DISTRIBUTION STATEMENT A. Approved for public release. Distribution is unlimited

This material is based upon work supported by the Assistant Secretary of Defense for Research and Engineering under Air Force Contract No. FA8702-15-D-0001. The views expressed in this thesis are those of the author and do not reflect the official policy or position of the United States Air Force, Department of Defense, or the U.S. Government.

This page intentionally left blank

TABLE OF CONTENTS

This page intentionally left blank

LIST OF FIGURES

This page intentionally left blank

LIST OF TABLES

This page intentionally left blank

1 INTRODUCTION

This chapter introduces the motivation for the research, objective of the research and an overview of the following chapters in this thesis.

1.1 Motivation

Additive manufacturing (AM) allows parts to be built layer by layer, in contrast to subtractive manufacturing, which removes material to create parts. Additive manufacturing is expected to drastically transform the field of manufacturing and design. AM allows for the near-net shape production of a wide range of geometries, which allows for more organic and efficient designs and less material waste [1]. Lighter and less complex components can be generated, leading to large weight savings. In the business of spacecraft, the weight savings can translate to $25,000 dollars per kilogram (Figure 1.1).

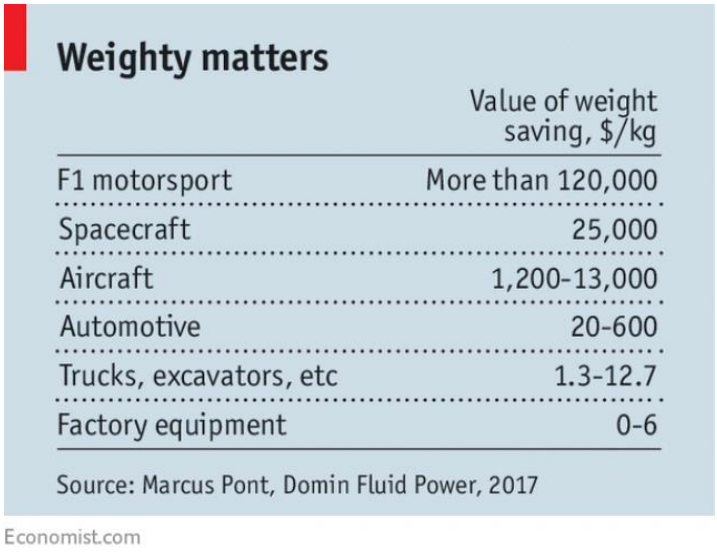

Figure 1.1: Weight savings per industry [2]

Additive manufacturing is well established for polymers. Yet polymers are often not sufficient for the high strength, temperature and fatigue conditions required for the aerospace industries [3]. Therefore, metal additive manufacturing is desired. Powder Bed Fusion (PBF) processes allow for the production of metallic parts from a wide range of materials, such as steel, titanium and

aluminium [4]. Out of these PBF processes, Selective Laser Melting (SLM) has garnered much scientific attention, due to its relative simplicity and capability to precisely vary the microstructure within a part [5].

SLM is driven by a wide range of operating parameters, and a suboptimal parameter choice results in defects and poor mechanical properties [6]. Therefore, the utilization of SLM remains largely in the field of rapid prototyping, as resulting parts are subject to variability and their characteristics are not always fully understood. This variability discourages high performance industries, which would most greatly benefit from this technology, from investing in transitions to the technology [7].

Traditional research in SLM has focused on the optimal energy densities for given materials, which is a combination of the laser power, laser scanning speed and layer height [8]. Little research has focused on the independent powder recoating process, which forms the foundation for the laser melting process. The quality and reliability of the final part is directly tied to the quality of the powder bed.

Research has shown that the properties of an additively manufactured part are influenced by powder bed properties, and a suboptimal powder bed will lead to part defects such as porosity [9]. Optimizing powder bed parameters, such as the powder and recoating method used, may also lead to improved results in the part density, mechanical properties, microstructure and surface quality [10]. Yet this field of research is relatively new and not yet well understood.

1.2 Objective

This research seeks to further the research communities' understanding of the powder recoating process. A long-term goal of this research would be to optimize the processing parameters for powder bed uniformity and tight packing density. Several of these parameters include the powder size distribution, height of the recoating blade, the blade geometry, recoating speed and induced vibration.

A two-pronged approach is planned for this research through a combination of simulations and experiments. Simulations enable quick iterations through processing parameters and allow the measurement of powder bed properties, which are difficult to measure experimentally. Experiments allow these simulations to be validated and allow the research community to realize

the viability of simulation parameters. Furthermore, an experimental powder recoating setup in an SLM system allows the effect of recoating parameters for multiple layers and SLM parts to be assessed.

The simulations use the Discrete Element Method (DEM), which calculates each particle movement and interaction for a set number of time steps. These simulations have proven effective for various scenarios to predict particle flow, and several simulations have been employed for powder recoating. With small particles, as present with AM powders, adhesive forces are larger than the force of gravity and these interparticle forces become significant. When small powders are used, these adhesive forces lead to agglomerates that tend to decrease flowability of the powder and packing density of the powder bed. Many of the current DEM simulations do not incorporate these adhesive forces, therefore these simulations may not accurately represent the powder recoating process. A portion of this research will focus on incorporating adhesive forces to a DEM code and calibrating the code to AM powders.

The experimental framework was established with a custom-built, instrumented powder recoating system. The powder recoating system allows the fine-tuning of important recoating parameters: blade geometry, recoating speed, blade height and blade vibration. The blade height feature provides the added capability to apply a compaction force to the powder bed during powder recoating. Strain rosettes placed on the recoater measure force in the normal and shear directions of the recoater. These features and capabilities allow the recoater to replicate scenarios produced from the simulations and verify their validity.

The combination of simulations and experiments enable novel powder recoating research. With this combination a new recoating system can be designed that optimizes powder bed packing fraction and uniformity. Furthermore, the impact of recoating parameters on SLM can be assessed.

1.3 Thesis Outline and Summary

- Chapter 2 covers powder and powder recoating in greater depth. The chapter explains how AM powder is made and important powder properties considered in additive manufacturing;commercial and academic recoating systems are discussed and a literature review of powder recoating research is conducted.

- Chapter 3 covers the design of the instrumented recoater and its subsystems, including the force sensing, blade positioning and linear motion capability.
- Chapter 4 covers the manufacturing and assembly of the instrumented recoater, the software development and the testing of these subsystems.
- Chapter 5 introduces the simulation model for powder recoating; the calibration of this simulation model with particle and bulk measurement is discussed; and exemplerary results from the simulation are provided.
- Chapter 6 concludes the thesis. A summary of the previous chapters and future work in the field are discussed.

2 REVIEW OF POWDER RECOATING

The purpose of this section is to establish a background understanding for the field of selective laser melting, additive manufacturing powder and powder deposition. The section begins by classifying powder bed fusion additive manufacturing processes and the impact of the powder bed on these processes. Then the important powder bed parameters (the powder and the recoater) are discussed. Finally, a literature review is conducted on the topic.

2.1 Powder Bed Fusion Processes

Additive manufacturing (AM) encompasses a variety of processes, which generally involve selective deposition of material or energy to create solid parts from computer-aided design (CAD) files. The layer by layer deposition makes AM largely appealing by allowing for geometric flexibility and minimal material waste [1]. Additive manufacturing requires a material, from which the part is made, and an energy source, which restructures the material into a single, solid geometry. AM processes are mainly differentiated based on their material and energy source. Several variants of AM, mainly involving plastics, have been scaled and marketed for direct consumer use [11]. Metal AM has attracted much attention due to the enhanced mechanical properties of metals over plastics. Yet commercialization and research in metal AM has been limited by the cost and complexity of the process. Metal additive manufacturing can be further subdivided into the form of metal feedstock used in the process.

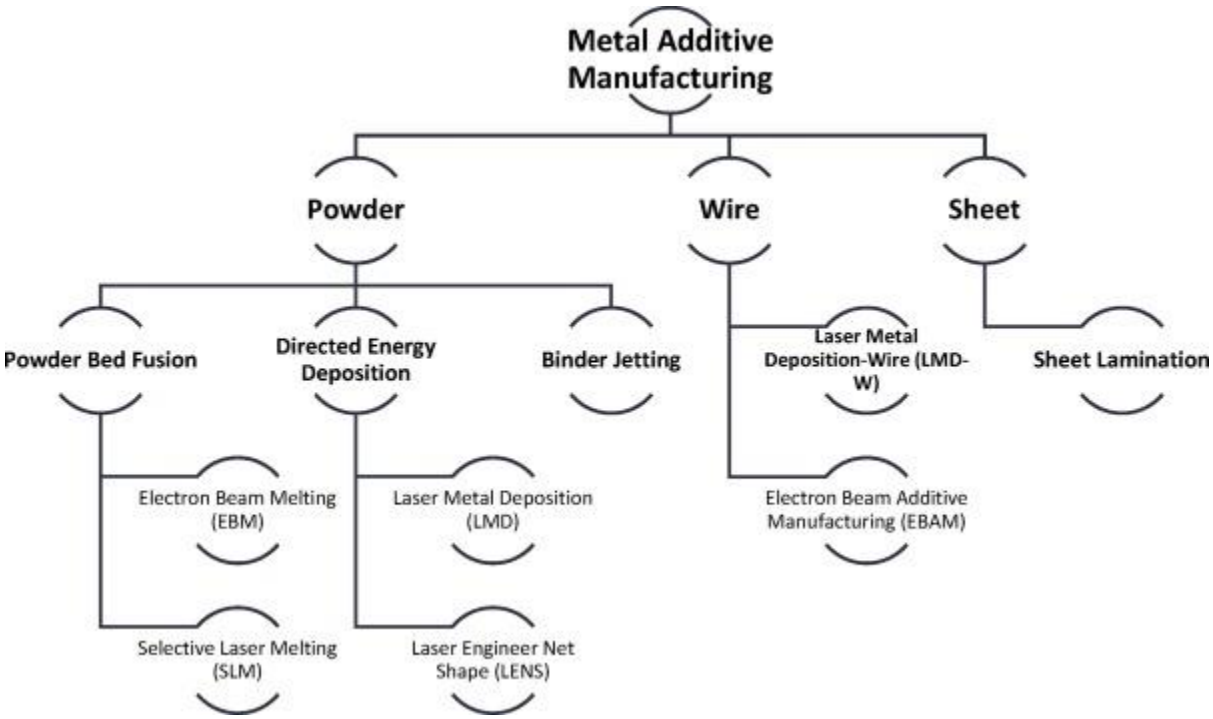

Figure 2.1: Metal additive manufacturing processes [10]

Figure 2.1 illustrates the division of metal additive processes based on their feedstock. A broad class of the methods involves depositing powder into a thin layer. The area in which powder is deposited is generally referred to as the powder bed or build platform. After deposition, the powder is fused via the energy source. For this reason, these processes are generally referred to as Powder Bed Fusion (PBF) processes. PBF includes Electron Beam Melting (EBM) and Selective Laser Melting (SLM). As their names suggest, EBM uses an electron beam, whereas SLM uses a laser beam [4].

This research focuses on SLM, largely due to the SLM capabilities in the Mechanosynthesis Group at MIT [12]. Furthermore, metal AM research is largely focused on SLM, due to its relative simplicity compared to other processes. SLM occurs in two steps. In the first step, metal powder feedstock is spread in thin layers across a build platform. In the second step, a high-energy laser scans the powder layer, melting the powders. The molten metal coalesces and solidifies on the build platform or the previous layer. The powder application and laser exposure processes repeat, forming a 3D geometry. These steps are illustrated in Figure 2.2.

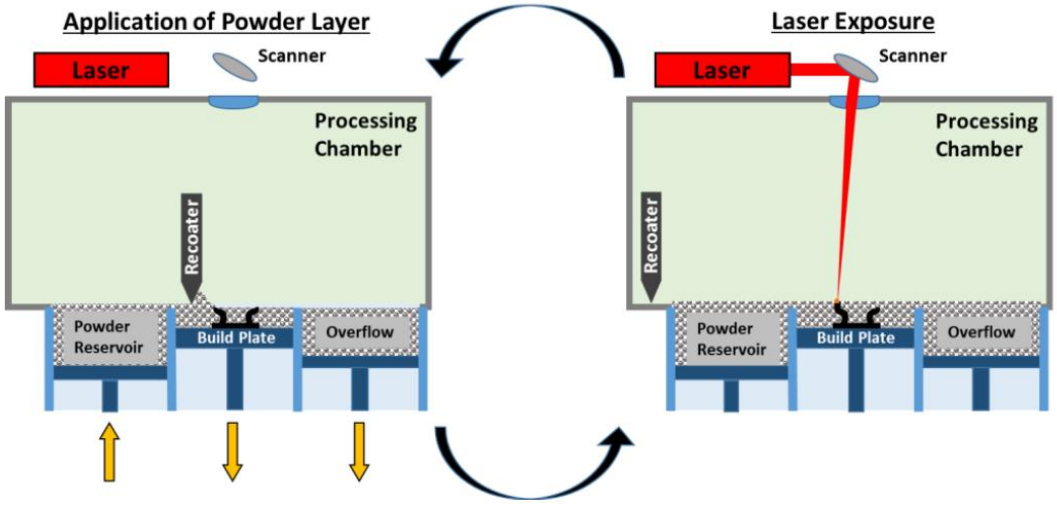

Figure 2.2: SLM workflow. First a layer is recoated then the layer is radiated by a laser [9]

This research mainly focuses on the powder recoating process, which is ubiquitous in all other powder bed processes. Aspects of this research may be more generally applied to other powder bed processes such as EBM and binder jetting. The distinction between other processes is made, since the operating range or relative importance of given parameters may vary between processes. For example, EBM typically uses larger particle size distributions, between 45-100 µm [13]. Binder jetting, on the other hand, largely employs rollers as opposed to blades, in their commercial machines [14]. These distinctions are due to the inherent differences between the processes and are attempts to optimize production given these distinctions. In Section 2.2, powder bed properties relevant to SLM will be discussed. The section reveals the reasoning behind several key design choices for PBF, such as powder size distribution or recoating method.

2.2 Powder Bed Metrics and Their Impact on SLM

SLM is a multiphysics process and can be explored at the macro, meso and microscale (Figure 2.3). At the macroscale, the focus is the cyclic heating of the part and temperature gradients in the part. If these variables are excessive then the build will fail. At the mesoscale the focus becomes the interaction of the laser with the individual particles. As the laser traverses across the powder bed, a melt pool forms, which solidifies onto the previous layer. At the microscale, the focus becomes the solidification of the melt pool. The metal will from grains based on the melt pool's

thermal and geometric boundary conditions [15]. This section will show the influence of the powder bed at each of these length scales.

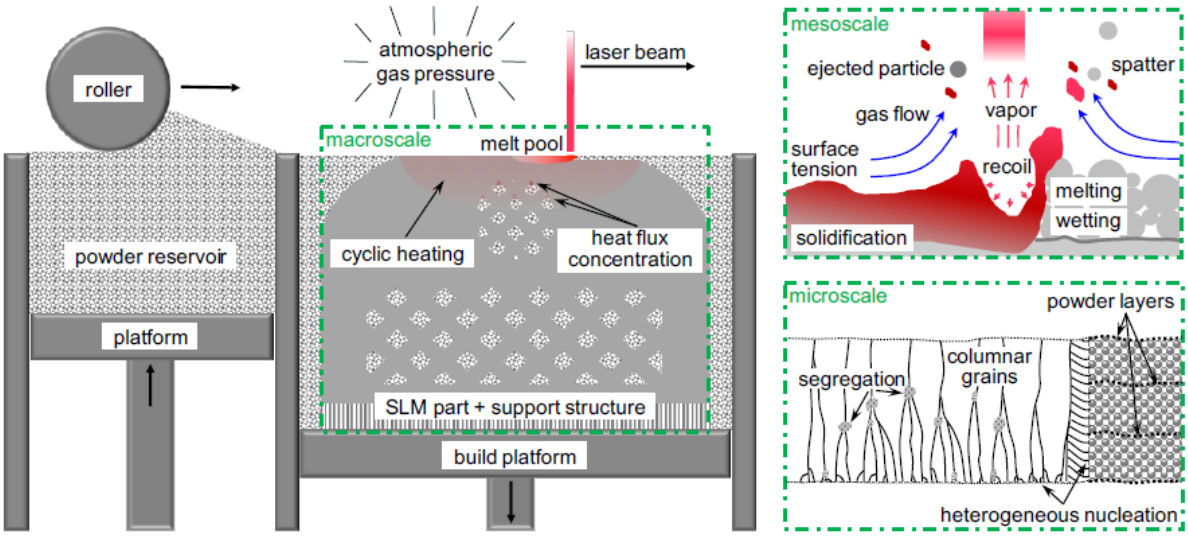

Figure 2.3: Selective laser melting at different length scales [15]

PBF powder layers are made from the combination of powder (Section 2.3) and the powder delivery system (Section 2.4). Layers are characterized by their thickness, uniformity and density. All of these characteristics impact the PBF process.

Layer thickness is defined as the minimum distance the heat source must travel through the powder to reach the previous layer. For commercial systems this property is configured with the platform displacement between layers, which is not always representative of the actual layer thickness [16]. Commercial SLM systems are generally capable of 20-150 μm layers [1]. Generally thinner layers are desired, as deformities may average out with multiple layers. Thinner layers also lead to higher resolution [1]. Layer thickness is limited by the powder size distribution being coated. Multiple studies recommend coating layers that are thicker than the maximum particle size [13]. Furthermore, layer thickness has a significant effect on the surface roughness and packing fraction of the powder bed.

Surface roughness is defined as the variation in the peak height of powder particles across the powder bed [17]. Surface roughness may result from powder agglomerating or objects being dragged across the powder bed [16]. Surface roughness creates variations in layer thickness and heat absorptivity, which may lead to printing defects. A high surface roughness has been shown

experimentally and computationally to cause defects in SLM parts [9], [18]. It is not well known the exact degree to which surface roughness affects part, especially since the laser melting process roughens the powder layer with spatter [19].

Packing fraction is defined as the ratio of the mass of the powder in a given layer to the mass of the bulk material of the same volume. Typically, the powder bed packing fraction is in the range of 30-60% and is driven by the recoating method, the powder morphology and the range of the powder size distribution [20]. With a wider size range of particles, smaller particles may be rearranged to fit between the voids of larger particles. Agitation or compaction from the recoater may help facilitate particle rearrangement [21]. A loose powder bed may cause melt pool discontinuities [22]. Denser powder beds have been shown to produce denser final parts with better mechanical properties [23]. An illustration of packing fraction and surface roughness are shown in Figure 2.4. As the figure shows, the two properties are not necessarily dependent.

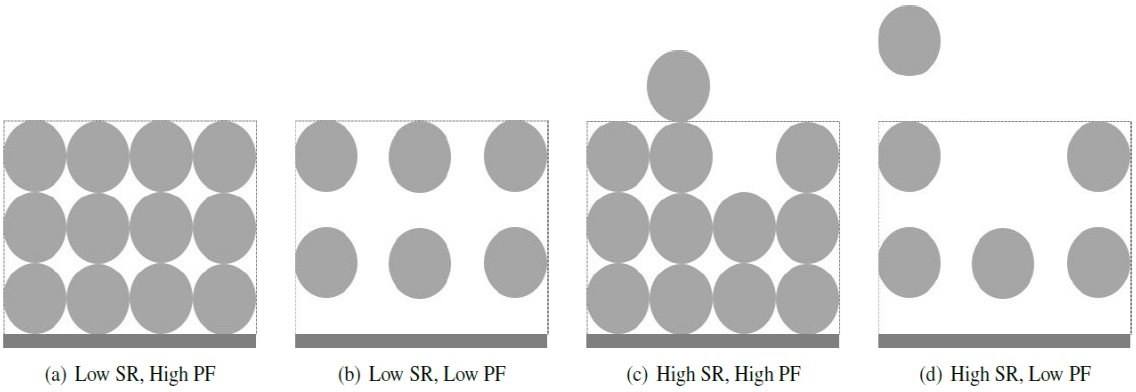

Figure 2.4: Illustration of packing fraction (PF) and surface roughness (SR) [24]

Uniformity of the particle size distribution is also desired. Powder may segregate during handling and during the recoating process. The granular segregation of particles is often compared to the brazil nut effect where larger particles tend to segregate to the surface of the mixture [25]. The local particle size distribution impacts the absorptivity of the powder. A varied size distribution will lead to varied thermal effects through the part and residual stresses as a result.[26]

2.3 Metal AM Powder

Metal powder is the foundation on which PBF occurs and is therefore critical in the process. Powder is manufactured and post-processed to meet the specifications of the AM process. These

specifications are a large driving factor of the powder cost. Powder may be characterized to determine its propensity to perform well in the given process. Yet, the role of these specifications on the resulting process outputs is not well documented in PBF literature.

2.3.1 Powder Manufacturing

The powder manufacturing method largely determines the individual particle properties and the cost of the resulting powders. Powder produced for additive manufacturing is produced largely in two ways: atomization and mechanically. Other methods exist, such as electrolysis, but the yielded powder is generally more expensive and used for niche research. User requirements define which powder is required for the given application [27].

Atomization uses the kinetic energy from a high-pressure liquid or gas to break apart a molten stream of metal into small particles. As the molten droplets fall, the surface energy of the liquid uniformly pulls the droplet together, effectively forming spheres. By the time the droplets reach the bottom of the atomization chamber, they have solidified into spherical or ellipsoid shapes [28]. Atomization has been used for multiple metals, such as titanium, aluminium and steel, and their alloys. Naturally, the atomization processing parameters, such as gas output and melting temperature, are varied across metals to account for their different properties [29]. This process described is illustrated in Figure 2.5

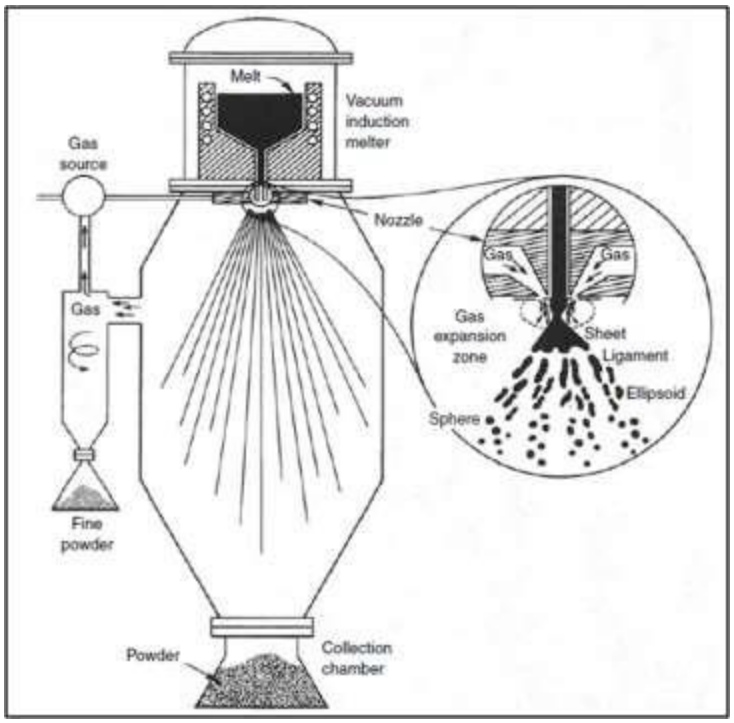

Figure 2.5: Schematic of the gas atomization process [28]

Atomization is often differentiated by the medium that is used to break the metal apart. Atomization may occur with water, gas or plasma. The cost and quality increase from water to gas to plasma atomization, where a higher quality infers a more spherical, less rough particle with a low level of contamination. Each of these processes yield different powder morphologies and size distributions of powders.

Atomization creates a wide size distribution between 0-500 μm [27]. The powder is segregated through sieving into narrower size distributions, determined by customer requirements [29]. Water atomization generally produces irregular and rough particles due to the rapid quenching rates of the metal with water [30]. Gas and plasma atomized powders produce highly spherical particles. These powders are preferred in SLM due to their improved flowing and packing behavior [27].

Mechanical processes involve crushing or grinding large particles until they meet the desired size. The process usually yields particles with irregular morphology, but the resulting powders are much cheaper than atomized powders [31]. The process of creating the initial material to be ground varies, but usually includes some chemical process, such as oxide reduction or hydride-dehydride. The chemical process creates a more brittle material, which is more prone to break into smaller particles and not recombine [27]. The duration of the process defines the size and morphology of

the resulting powders. Mechanical processes have also gained attention through their utilization to create composite powders for metal matrix composite production in SLM [32]. The morphological differences between these powders can be seen in Figure 2.6.

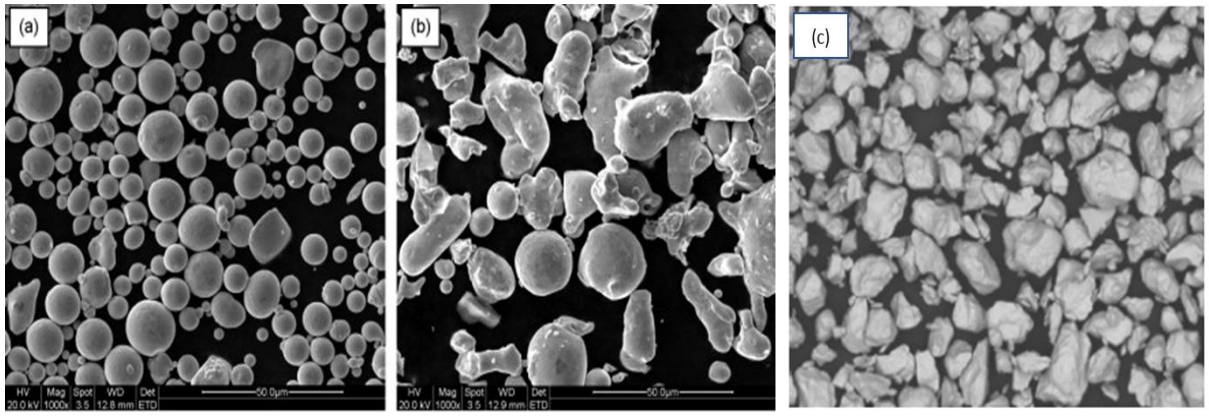

Figure 2.6: SEM images of (a) gas atomized powder (b) water atomized powder [33] **(c) hydride-dehydride powder** [27]

Powder may be chosen based on the application or material. In some cases, a given material may not be compatible with a powder processing technique or there may not be enough demand for the powder. For high quality parts, such as those required in the medical industry, only high-quality plasma atomized powder will be used. A comparison between the processes is a useful tool towards selecting the right powder. A summary of the advantages and disadvantages of these processes as well as their common uses is provided in Figure 2.7.

Manufacturing Process	Particle size, µm	Advantages	Disadvantages	Common uses
Water atomisation	0–500	High throughput Range of particle sizes Only requires feedstock in ingot form	Post processing required to remove water Irregular particle morphology Satellites present Wide PSD Low yield of powder between 20–150 µm	Non-reactive
Gas atomisation (inc. EIGA)	0–500	Wide range of alloys available Suitable for reactive alloys Only requires feedstock in ingot form High throughput Range of particle sizes Use of EIGA allows for reactive powders to be processed Spherical particles	Satellites present Wide PSD Low yield of powder between 20–150 µm	Ni, Co, Fe, Ti (EIGA), Al
Plasma atomisation	0–200	Extremely spherical particles	Requires feedstock to either be in wire form or powder form High cost	Ti (Ti64 most common)
Plasma rotating electrode process	0–100	High purity powders Highly spherical powder	Low productivity High cost	Ti Exotics
Centrifugal atomisation	0–600	Wide range of particle sizes with very narrow PSD	Difficult to make extremely fine powder unless very high speed can be achieved	Solder pastes, Zinc of alkaline batteries, Ti and steel shot
Hydride–dehydride process	45–500	Low cost option	Irregular particle morphology High interstitial content (H, O)	Ti6/4 Limited to metals which form a brittle hydride

Figure 2.7: Differentiators between powder manufacturing processes [27]

2.3.2 Powder Particle Properties

As mentioned previously, powder manufacturing has a large influence on the powder properties. The key particle properties, which influence the powders bulk behavior, are morphology and size distribution.

Morphology describes the shape and surface of particles. Morphology is usually described qualitatively, looking at the characteristic shape of the particles. Morphology can also be described in further depth with terms such as aspect ratio, sphericity or elongation. Referring to the previous figures, 2.6a would be described as mostly spherical, 2.6b as rough and elongated and 2.6c as rough and jagged. Morphology can be assessed with scanning electron microscope (SEM) images of the powder.

Each powder production process creates a wide size distribution of metal particles. Granulometry is the measurement of this size distribution. To create a narrower size distribution, powders are sieved through a fine mesh. The distribution of particle sizes may vary within a sieved range. To document this distribution, the D10, D50 and D90 are reported. These values report that 10, 50 or 90%, respectively, of powder by mass or volume is below a diameter. Measurement of the granulometry is conducted with optical or light-scattering instruments that measure the diameter and frequency of particles. From this measurement, the D10, 50, and 90 can be calculated and a histogram can be created which plots the volume percent versus a logarithmic scale of particle diameter [13]. For atomized powders, these plots show a log-normal distribution of powders with varying standard deviations.

2.4 Powder Delivery Methods

PBF relies on three different mechanisms for powder delivery: a blade, roller or a hopper [34]. See Figure 2.8. AM literature does not denote a large significance between the three mechanisms; however, different powder bed fusion processes generally prefer one method.

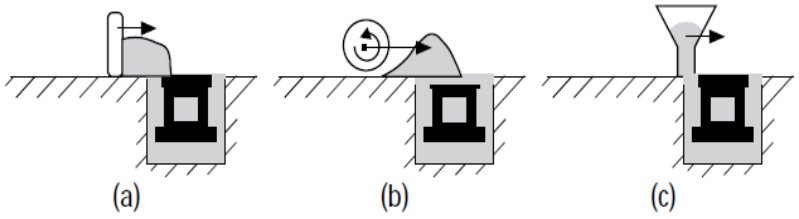

Figure 2.8: Powder deposition techniques [34]

The blade mechanism is more prevalent in commercial and academic SLM systems, likely due to their simplicity, lower cost, and faster recoating capabilities. The geometry and material of blades vary in commercial machines. The blades commonly used have an arbitrary bevel and are moved with the beveled side facing away from the powder being coated. Stiff blades must be moved at a fixed distance above the surface plate to avoid recoater interference with the substrate or solidified regions of the powder bed. Compliant blades may also be used, but these blades provide less layer height certainty [35].

The recoating process also varies from machine to machine. Some machines pass over the powder bed once before lasing the powder and others use multiple blades. Often in large commercial

machines, a large and stiff recoater is used with a noncompliant blade, as shown in Figure 2.9. This design enables the machine to create repeatable layer heights over a large area and remove solidified material when there is recoater interference.

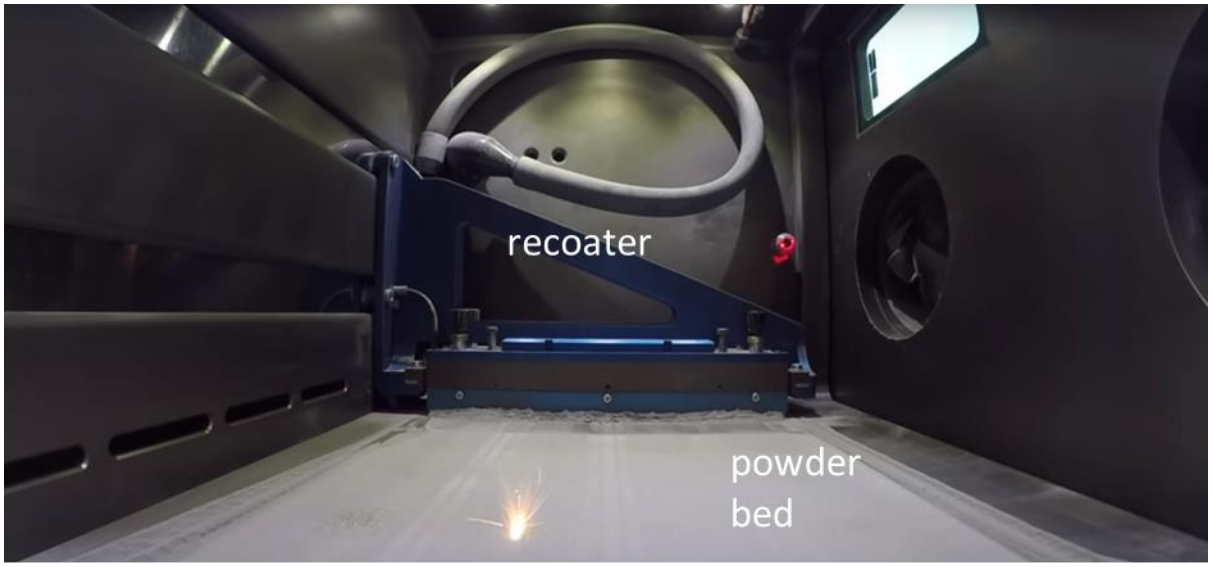

Figure 2.9: Recoater Design in LASERTEC 30 SLM powder bed machine [36]

Other methods have been incorporated into these standard recoating designs to maximize the packing density of the powder bed. These methods are usually employed for machines designed for small powders, where agglomerations become a concern. Roy et al. [37] uses a two-phase approach with both a blade and vibrating, counter-rotating roller. The blade deposits the powder, whereas the roller breaks up the agglomerates and packs the powder. Exner et al. [38] covers the build platform with a lid and uses the build platform to apply pressure to the powder, forcing their rearrangement.

2.5 Powder Recoating Literature

This thesis will cover powder recoating from an experimental and computational perspective. Often the different approaches focus on different quantifiable metrics. For this reason, the literature review is divided between computational and experimental results.

2.5.1 Computational Recoating Studies

With increasing computational power, complex DEM simulations have become more feasible. The majority of AM powder simulations have been published in the last few years. These simulations have been able to track the entire recoating process. This includes powder being poured into the powder reservoir, blade or roller recoating and powder settling in the build platform. Computational recoating research focuses on the effects of different parameters on the powder bed (PB). The three major publications in this topic were published between 2015-2018 and come from: Mindt et al [16], Parteli et al [17], Herbold et al [39]and Haeri et al [40], [41].

Mindt et al. studied the effect of the blade to build platform displacement on the PB uniformity. The authors found that decreasing the blade gap led to lower packing densities, due to large particles being dragged across the powder bed. By running the numerical PBs through their melt pool simulations, the researchers showed that powder bed discontinuities lead to melt pool discontinuities and thus rougher parts.

Parteli et al. focused on the influence of the particle size distribution and roller speed on the uniformity and packing density of the powder bed. This publication was novel in several respects. They were able to recreate irregular powder geometries based on a commercially available powder. The influence of recoating over a solid part was studied by creating a discontinuity on the build platform. The force of cohesion at particle-particle contact was included to account for the formation of agglomerations. The authors also included the force that the part experiences during recoating. The research showed that the uniformity of the powder bed decreases nonlinearly with speed. The study also showed that the use of finer particles leads to a less dense powder bed.

Herbold et al. worked to validate that the internal Lawrence Livermore GEODYN-L solver could be used to produce realistic powder beds. The solver differs from LAMPPS and other DEM solvers, as it can incorporate ellipsoid particles and uses an FEM solver for particle-particle impact. The authors also noted the presence of layer-layer mixing during the recoating process. While the authors discussed the significance of rolling resistance and cohesive forces, these forces were not included in the model.

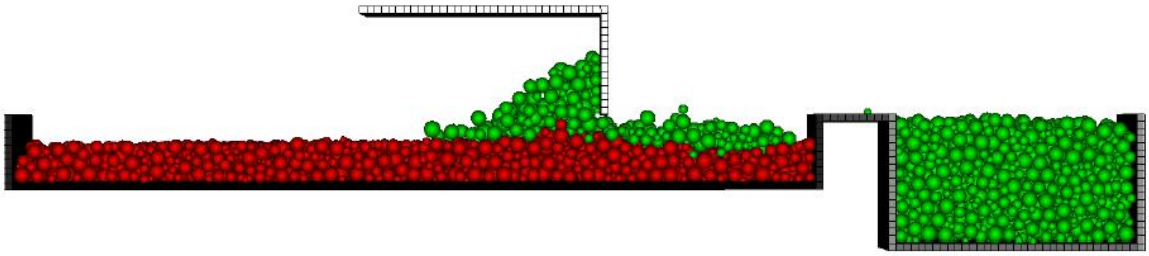

Figure 2.10: DEM powder recoating simulation architecture [39]

Haeri et al. [40] performed similar analysis to Parteli, but focused on rod shaped particles, similar to those created through milling. The simulation geometries were created by bounding several spherical particles together in a line. Similar to Parteli, Haeri found that greater recoater translational speed and more oblong particles result in a lower powder bed quality, defined by surface roughness and volume fraction. Haeri et al. [41] studied the effects of the blade geometry on the powder bed properties. In summary, it was found that the blade geometry could have a large impact on the surface roughness and packing density.

2.5.2 Experimental Recoating Studies

Most experimental SLM powder bed literature focuses on the effects of powder morphologies and granulometry in commercial machines. These effects are measured by sampling a section of the powder bed or creating an SLM test sample. From a morphology stand point it is stated that a more spherical powder generally leads to a more uniform and tightly packed powder bed [13], [42]. The granulometry also has a large effect on the powder bed. In general, a wider size distribution leads to an improved powder bed density, but these powders are harder to spread [33]. As a result, wider size distributions may lead to a larger surface roughness or may not coat at all [13]. As far as the author is aware, no experimental literature exists which measures the influence of different recoating parameters with metal powders, such as recoating speed, blade geometry and blade height.

This page intentionally left blank

3 Design of an Instrumented Powder Recoater

The instrumented recoater offers in situ control and measurement during powder coating within the Hybrid Additive Manufacturing Recoater (HAMR) system. The control capabilities, the blade and the blade positioning are designed to enable precise control of recoating parameters to ensure a densely packed and uniform powder bed. The force measurement capability enables further insight into the powder recoating process and provides a link between powder recoating and powder bed outcomes. This chapter will cover the design of the instrumented recoater system through discussion of system overview, design requirements, key design choices, and theoretical system performance.

3.1 Recoater System Overview and Anatomy

The recoater system is enclosed within a machine called the Hybrid Additive Manufacturing Recoater (HAMR). The system is named for its additive manufacturing capabilities of "hybrid" material deposition from a recoating and inkjet system. In addition to these deposition systems, HAMR is capable of atmospheric control and advanced optics. Intricate details of the other HAMR system will not be covered in this thesis, as they are not relevant to powder recoating or the instrumented recoater.

All of the recoater and inkjet components sit on a plate of steel referred to as the datum A plate, since most measurements of precision are in reference to this plate. The datum A plate has a removable section, which slides in and out to allow the operator to access the build platform from the side. The datum A plate is fixed to an optical breadboard with four posts to provide vibration stability. Underneath the datum A plate are the pistons for the platforms and miscellaneous electrical wiring and components. An airtight steel box encloses this entire volume. Another steel plate houses the optical components and is aligned to the top of the datum A plate with three kinematic couplings. Three cable penetrators in the steel box connect the electrical components in

the box to a control box. A computer near the HAMR system communicates with the control box using LabVIEW. An overview of the system CAD model is shown in Figure 3.1.

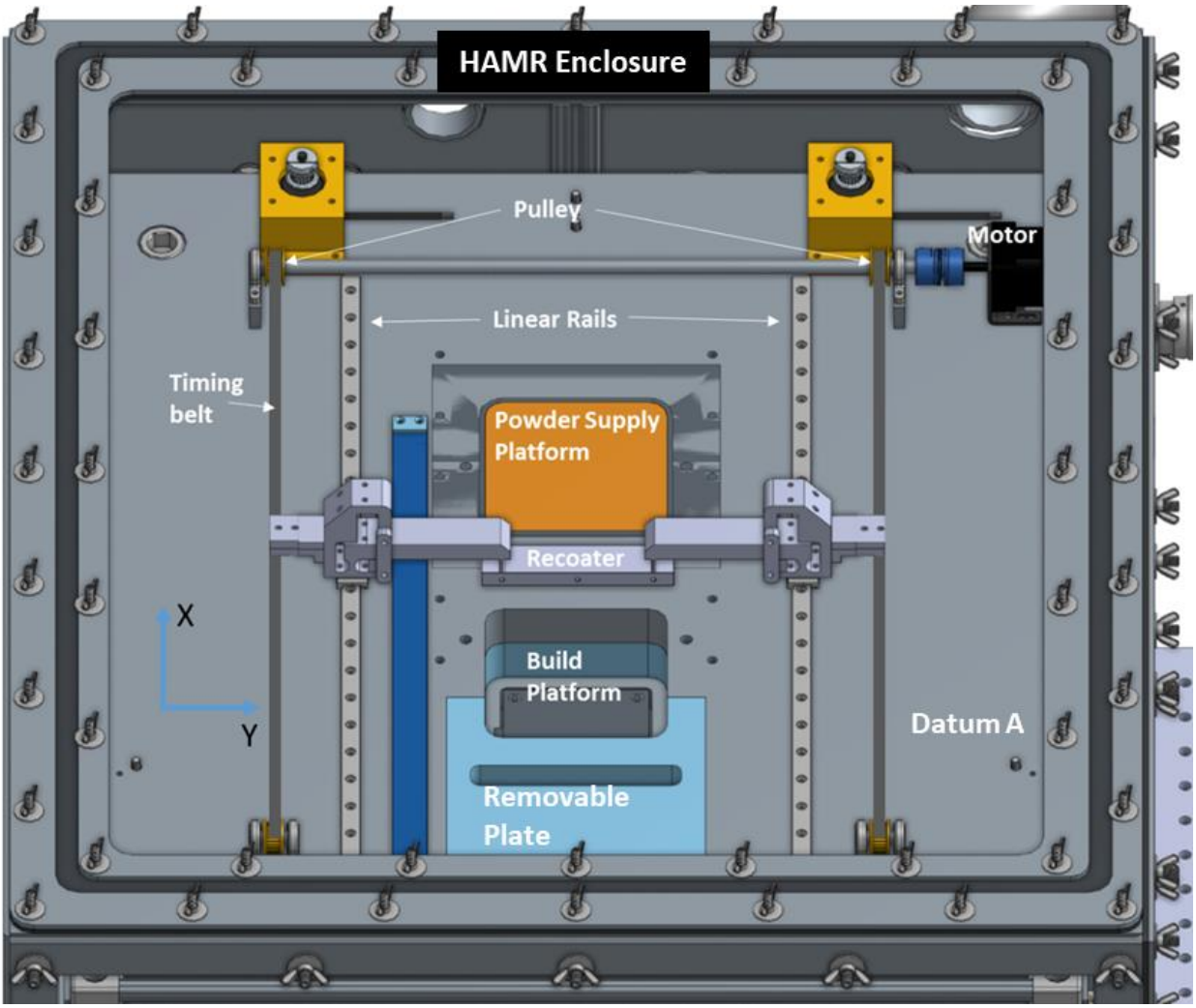

Figure 3.1: HAMR and recoater system overview

The recoater system operates similar to many conventional metal AM recoaters. A blade moves powder from a powder resupply platform and coats a thin powder layer over the build platform. Excess powder is deposited in a powder overflow bin. The recoater is actuated using a timing belt system, comprised of a motor, rod, bearings and pulleys (Section 3.5). Repeatable linear movement is assured with linear rails.

The recoater was designed to recoat different layer heights with configurable blade geometries, while sensing the amount of force the blade experiences. To ensure experimental repeatability and

maximize layer uniformity, the recoater was designed with an error budget of less than 15 μm. The design incorporates piezoelectric stack actuators for precise adjustment of the blade height, strain gauge rosettes to measure forces during recoating and a planar constrained blade mount to allow multiple blades of different geometries to be mounted. Figure 3.2 provides a brief diagram of these module subsystems.

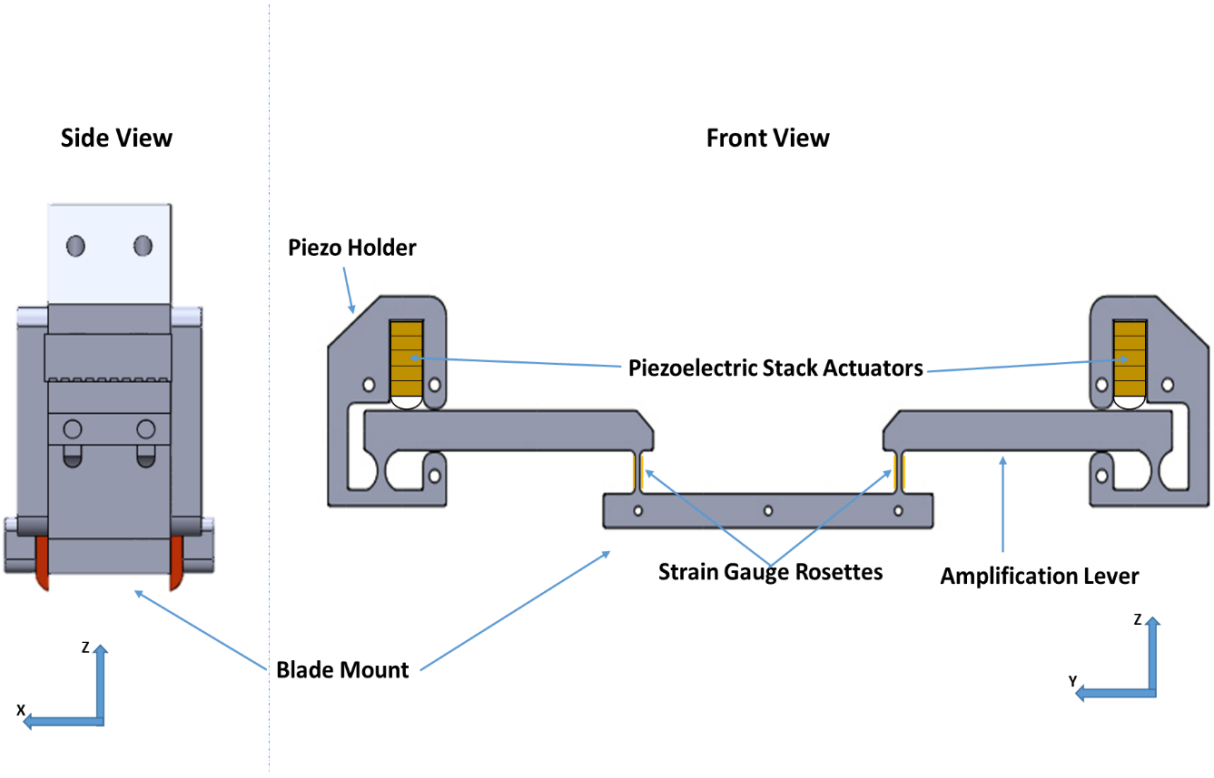

Figure 3.2: Recoater system overview

The capabilities of these subsystems are summarized in Table 3.1. The motivations for these capabilities are discussed in Section 3.2.

Table 3.1: Recoater design specifications

Parameter	Specification
Blade Displacement Stroke	200 μm
Horizontal Force Resolution	4 mN
Vertical Force Resolution	0.5 mN
Layer Height	20-200 μm
Recoater Blade Position	$\pm$ 2 μm

The subsystems, their capabilities and their design will be discussed in this chapter. Section 3.2 Motivation for Design Requirements will discuss the different design considerations for the recoater. Section 3.3 Blade Positioning, will cover the piezoelectric and flexure system for changing the blade height. Section 3.4 Force Sensing, will cover the strain gauge rosette and Wheatstone bridge design for measuring recoating force. Section 3.5 Horizontal Linear Motion will discuss the linear motion system that moves the recoater across the powder and build platforms. Section 3.6 Error Budget will discuss the error modelling and the designed level of precision for HAMR.

3.2 Design Requirements

The design of the recoater was driven by user interface, other HAMR subsystems and research capabilities. These design requirements include blade vertical positioning, force sensing at blade, blade exchange flexibility and ease, velocity range, precise movement, modularity and geometric constraints. The reasoning for these design requirements and their impact on the design will be discussed in this section.

There is a large demand for in situ monitoring of SLM, as it would allow process defects to be detected during the process instead of afterwards. In situ monitoring relies on high speed optical or infrared monitoring of the melt pool [43]. Resolution can be increased if the distance from the measuring device and the melt pool is minimized. To maximize imaging resolution in HAMR, the distance between the datum A plate and optical components was kept at 60 mm. For this reason,

all components on the datum A plate, including the recoater and inkjet, were designed to be less than 60 mm in total height.

Mindt et al [16] explored the influence of blade height on powder recoating. Mindt found that the blade height had a large influence on the powder layer. Too small of a blade height would result in particles dragged across the powder layer in a process referred to as "corn rowing", resulting in a less dense powder bed. Too large of a blade height would result in thick layers, resulting in poor resolution. Furthermore, it is well-documented that the recoater may collide with the SLM part during printing. The laser melting and solidification process may lead to an elevated height during melt pool solidification, which can result in recoater interference and collision. These blade collisions may result in blade damage and in turn a nonuniform powder bed [9]. For these reasons, it was desired that the blade be able to move 2-3 times the maximum layer height, approximately 200-300 μm, during recoating.

Parteli et al [17] created a discrete element model of the powder recoating process. In this study, they cite that large fluctuations in recoating forces demonstrate the dynamics of force distribution through the powder. These forces provide insight into the granular mechanics of the process, essentially how the particles flow and settle into their packing configuration [21]. Understanding these forces would enable researchers to design blades or recoating mechanisms, which evenly distribute force through the powder bed to create uniformity and high packing density. Furthermore, empirically measured forces could be compared to forces measured in a simulation, as in [17], to validate the model. As far as the author is aware, no studies have attempted to measure the forces of the recoating process empirically. For these reasons, it was desired that the recoater be able to measure force in the normal and transverse directions of recoating, as discussed in Section 3.4.

As discussed in Chapter 2, a variety of recoater blades have already been employed in commercial systems. Several machines employee multiple blades (LaserTec 30) [36]. The differences between these blades and blade configurations is not well understood. Haeri et al [41] showed the impact of the blade geometry on the recoating process, by computationally varying the blade geometry in a recoating simulation. For these reasons, it was desired that the recoater be able to fit multiple blade geometries and materials, as well as multiple blades at the same time.

The velocity of powder recoating directly translates to the productivity of the machine, as powder must be deposited for each layer of the build part. Commercial machines have been cited traveling up to 250 mm/s [42]. Several numerical studies have explored the effects of the powder recoating velocity on the density of the powder bed [17], [41]. These studies usually state that a faster recoating velocity will degrade the powder bed density. For this reason, it was desired that the recoater be able to travel within a large range of velocities, preferentially up to 150 mm/s, to study the effect of the recoating velocity and to maximize productivity of HAMR.

Designing for precision aims to minimize the error (actual position minus desired position) of the machine. The precision of a machine translates to its ability to meet design tolerances, reproduce results and take accurate measurements. For typical manufacturing machines the error motion of the machine is directly correlated to the machine's tolerances, but the relationship is less well understood for PBF machines. The vertical position of the blade was deemed the most critical direction, thus requiring the least error, since the main process parameter of powder recoating is the layer height. For this reason, the error tolerance of the recoater in the z-axis was set to 15 μm. The error tolerance is representative of the smallest particles within a standard powder size distribution and it is therefore assumed that errors below this tolerance would not lead to a significant variation in the powder layer height.

The recoater design was also required to be modular. Modularity describes the degree to which components can be separated and recombined. Modularity was desired, as it enables flexibility in the research goals and requirements of HAMR. With HAMR's modular design, different types of recoaters can be installed in HAMR. The recoater must only be disconnected from the timing belts and the linear rails before it can be interchanged.

A powder recoater must be able to withstand harsh environmental conditions. Thermal management becomes a concern as the build plate is heated to elevated temperatures and heat is transmitted from the laser melting process. The largest concern, however, is the powder, which is being recoated. The powder presents very fine metallic dust, which becomes air borne during powder recoating and laser melting. This dust can cause moving components to jam. For this reason, all of the recoater's rotational and linear bearings contain environmental seals. A barrier also separates the powder from the linear rails.

3.3 Blade Positioning

Precise linear motion requires an actuator and a bearing. The actuator controls the movement and the bearing ensures that motion is constrained to the desired axis of movement. Flexures were utilized as the linear motion guide for the blade positioning system, due to their ability to provide small controlled movements. Piezoelectric stack actuators were utilized as actuators, due to their large force outputs and small space profile. The combined flexure and piezoelectric actuator positioning system has a theoretical displacement output of 200 μm.

3.3.1 Piezoelectric Actuation

Actuators provide the linear or rotary inputs required for motion along the bearing. In small scale applications, these actuators take the form of DC motors, stepper motors or piezoelectrics. Piezoelectric stack actuators (also referred to as piezos) were chosen as the actuator, since they are easy to control, stiff and enable precise movement. The piezoelectric stack actuators allow precise blade height control, powder bed compaction, and vibration.

Piezoelectric materials, of which lead zirconate titanate (PZT) is the most common, deform when a voltage is applied across them due to the piezoelectric effect. Since piezoelectrics displace to 0.1% of their height, piezoelectric crystals are often stacked upon each other. Depending on the height of the piezoelectric stack, the displacement is on the order of microns. The recoater utilizes piezoelectric stack actuators with a length of 17 mm and a cross section of 10x10 mm. The dimensions allow a 20 μm displacement when a 150 V bias is applied [Thorlabs, PK4HQP1].

The displacement of the piezoelectric stacks is also influenced by their mechanical loading condition. Mechanical forces will cause the material to linearly deform according to Hooke's law. The mechanical properties of the piezo limit how much force the stacks can generate. The maximum amount of force that a piezo can generate is called the blocking force. The blocking force of the selected piezos is 4000 N, but any force in the direction of expansion will limit the full-range of expansion for the piezo. In this application, the piezos expand to generate a force, which deforms a flexure and generates a displacement. To fully predict the displacement of the piezo, the mechanical and piezoelectric strain responses need to be coupled [44]. This is demonstrated in equation 3.1.

$$\Delta h = \varepsilon\, L = L\, S\, \sigma + d\, V \tag{3.1}$$

where Δh represents the piezo change in height, ε represents the total strain, L is the length of the piezo, S is the material compliance, σ is the material stress, d is the piezo electric constant, and V is the bias voltage across the piezo.

The direct properties of PZT are presumably proprietary and must be inferred. The compliance can be calculated using Hooke's law (Eqn 3.9) based on the blocking force of the material. This would give a compliance of $S = 29.4\ x\ 10^{-12}\ Pa^{-1}$. The electric constant can be calculated from the displacement, applied electric field and number of stacks, as $d = 133\ nm/V$. Given the stiffness of the flexures and position of the piezo discussed in Section 3.3.2, the piezo will require approximately 320 N to reach its full displacement. Assuming a linear stiffness simplifies the applied force on the piezo to 2.1 N/V. With these parameters and the geometry of the piezo, equation 3.1 can be rearranged so the expansion is only a function of the bias voltage.

$$\Delta h\,(V) = \ 122.5\ \frac{nm}{V}\ \ (V) \tag{3.2}$$

With a max bias voltage, the total displacement of the piezo becomes approximately 18.4 μm. Any other stiffness or misalignment will further affect the displacement yield of the piezo. This topic will be further discussed in Chapter 4 with the assembly of the recoater.

The positions of the piezos were chosen such that the expansion of the actuators results in a downward blade movement (Figure 3.3). This configuration was chosen to ensure the piezos provide additional stiffness to any recoating force, ensure that powering down the piezos does not result in the recoater blade being forced into the datum plate and minimize the vertical profile of the recoater. Furthermore, the configuration enables a compaction force be applied to the powder bed.

Due to this configuration, a holder must surround the piezo and ensure that displacement is only directed to rotate the flexure. The holder was designed to tightly fit the piezo and to maximize stiffness in the z-axis. Further reinforcement and contamination protection is provided with a plate which fits over the piezo holder and is secured with fasteners. The fasteners are designed to be

tightened, such that, friction ensures no lost displacement between the recoater holder and the plate.

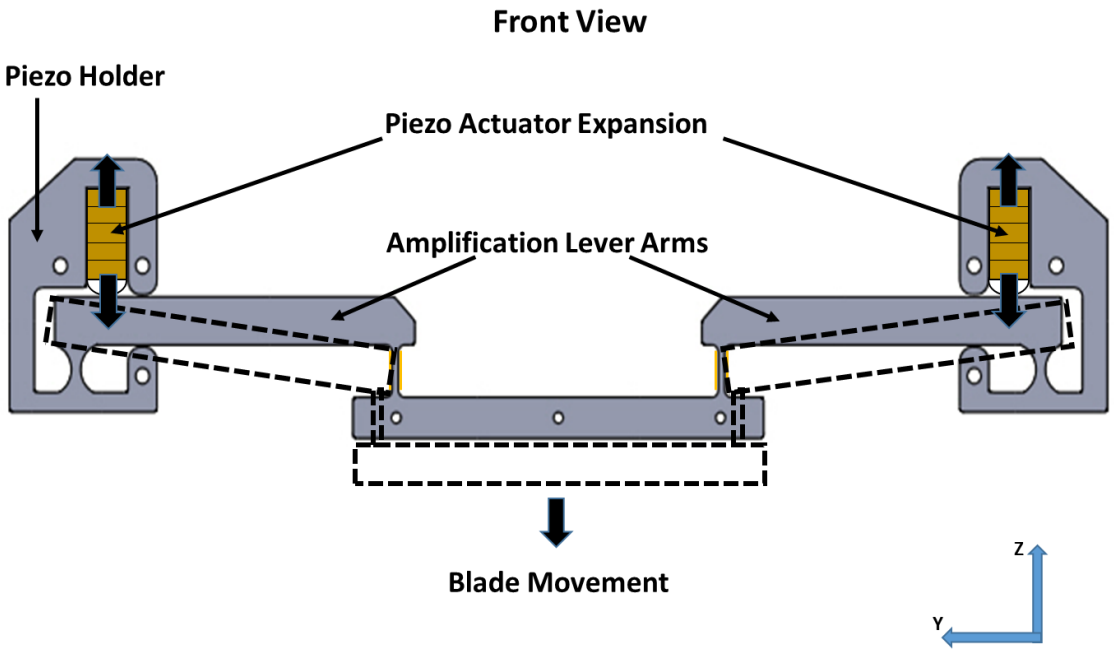

Figure 3.3: Blade positioning with the piezoelectric actuators and flexural bearings

3.3.2 Flexural Bearings

Linear motion guides or bearings are defined by their method of transferring motion, where sliding and rolling bearings are the most commonly utilized bearings. Flexural bearings were chosen as the linear motion guide as they enable precision, small scale linear motion and meet the design requirements. Flexures meet the design requirements of precise blade positioning over an extended range, blade rotational compliance, force sensing and environmental robustness.

Flexures are used in precision applications to provide small, controlled displacements or rotations. Applications of flexures can be seen in a variety of systems from satellites to linear motion stages. Flexural bearings are highly customizable to their application and are not sensitive to their environment, making them ideal for the HAMR system. Flexures are designed to provide compliance in the direction of movement and remain stiff in off axes. Displacements occur because of elastic deformation of the material. Due to the nature of the deformation, these displacements are precise and repeatable [45].

Flexures exist largely within two categories: monolithic or clamp. Monolithic flexures were chosen to avoid variation during assembly. Monolithic flexure hinges displace on the order of $1/100^{th}$ of their size and can be further subdivided based on their geometry (Figure 3.4) [45].

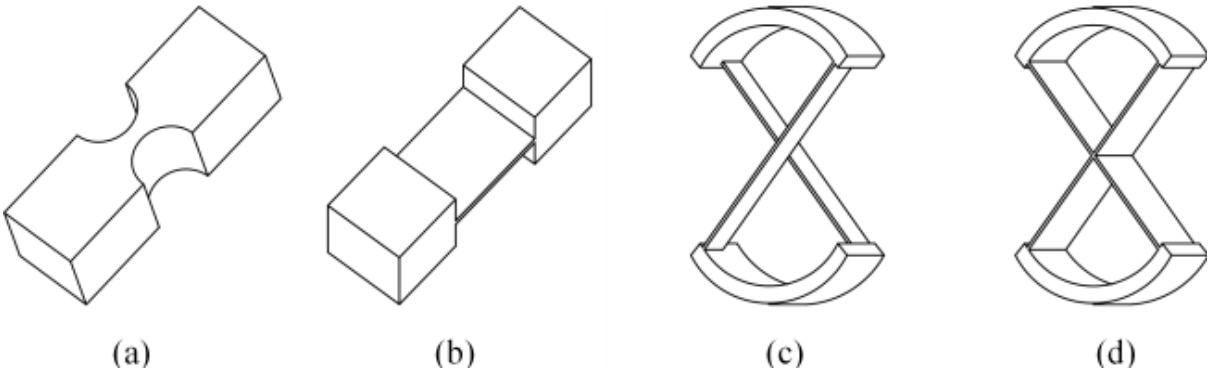

Figure 3.4: Main types of flexure hinges (a) Notch (b) Blade (c) Cross-Strip (d) Cartwheel [46]

3.3.2.1 Lever Mechanism

The design requirements of the recoater specifies a displacement at the blade of several hundred microns. Since the piezo displaces on the order of tens of microns, the flexures were also designed to amplify this displacement. Flexure amplification systems are common in large displacement piezoelectric stages. Several of the mechanisms that exist for these stages are shown in Figure 3.5. Mechanisms such as the bridge-type yield large displacements but are only capable of small loads due to the orientation of the flexures. Therefore, a simpler lever-type flexure mechanism was chosen for the recoater.

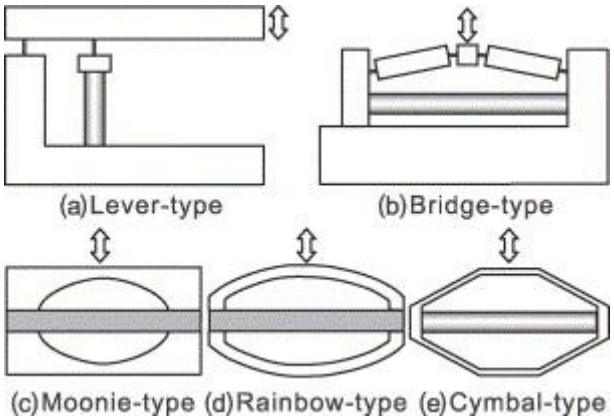

Figure 3.5: Flexure amplification mechanisms [47]

The lever system is comprised of four rotationally-compliant flexures: two notch flexures and two blade flexures. The flexures are positioned on both sides of the levers (Figure 3.6). Together this system of flexures enables blade control linearly in the z-axis and rotationally about the x-axis, θ_x. The lever is based on the idea that the piezo displacement at a set distance leads to an angular rotation about the flexure. The output displacement of the lever is the *sine* of the angle multiplied by the distance from the flexure. The key to maximizing the lever output is minimizing the distance from the piezo to the flexure, leading to a greater angular rotation, and also maximizing the length of the lever. The lever output can be simplified to Equation 3.3.

$$\delta_{out} = \frac{\delta_{in}\, l_2}{l_1} \tag{3.3}$$

where δ_{out} is the output displacement, δ_{in} is the input displacement from the piezo, l_2 is the length of the amplification lever, and l_1 is the distance from the piezo to the flexure.

Equation 3.3 was used to calculate the output of the recoater displacement. With δ_{in} = 18.4 µm, l_1 = 5 mm and l_2 = 82.5 mm, a displacement of 300 µm at the blade mount was calculated.

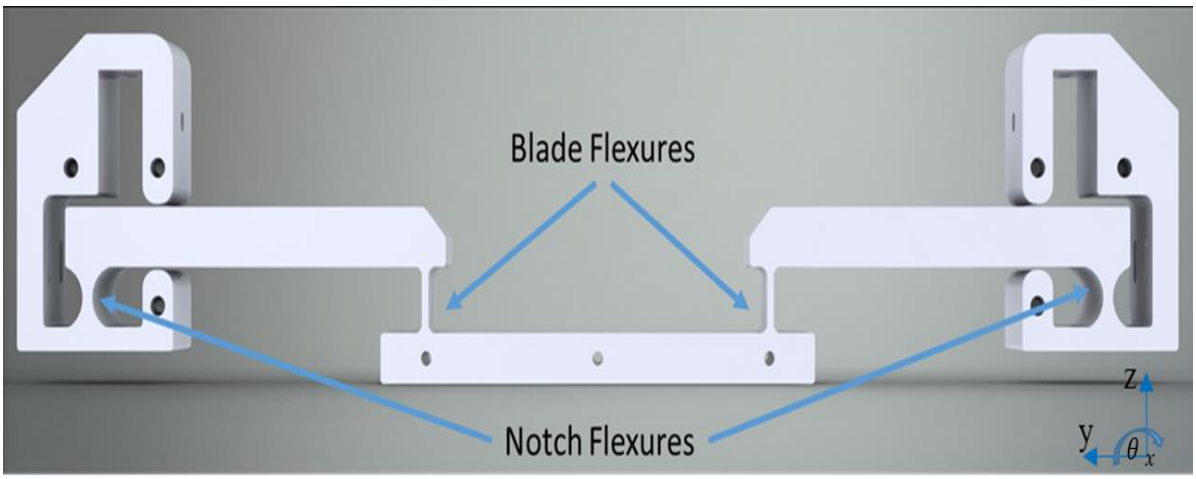

Figure 3.6: Flexure locations on recoater. Notch flexures rotate due to piezo electric expansion. Blade flexures provide rotational compliance.

Literature states that piezoelectric actuators often fall short of the geometric estimate. In piezo amplification systems, displacement may be lost between interfaces and parasitic deformation of flexures. Often Finite Element Analysis (FEA) provides a better prediction of the system performance [47]. For this reason, FEA was carried out on the recoater.

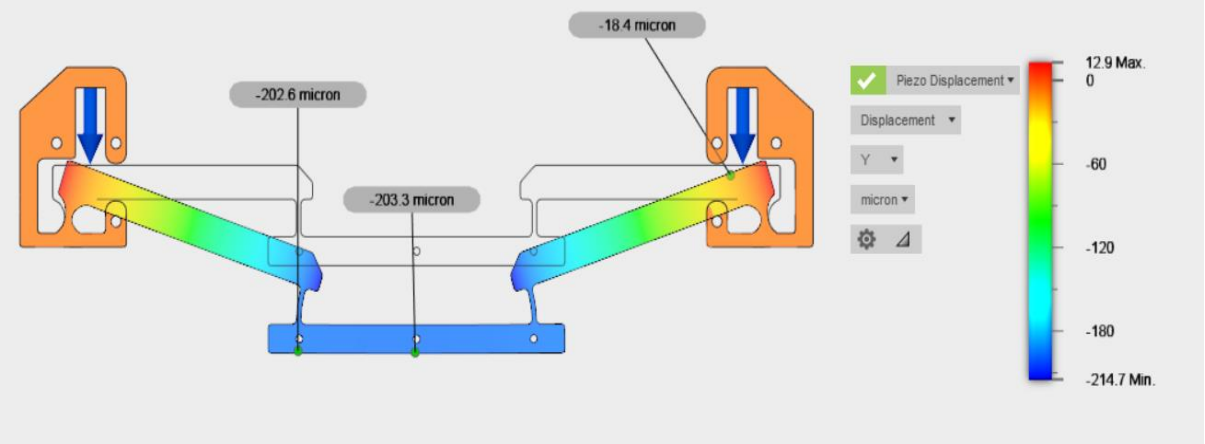

Figure 3.7: Lever system FEA

Finite Element Analysis was carried out in Autodesk Fusion 360's simulation package. To prepare the simulation, loading conditions and constraints were configured on the CAD model. Rigid constraints were placed on the eight bolt holes of the recoater and a 300 N load (the load to reach the designed rotation of the flexure) was placed on the amplification arm at the location the piezo would sit. The simulation was run, and the displacement was probed at the location on the lever arm where the load was applied and at the blade mount. The simulation resulted in an 18.4 µm displacement at the lever arm and a 200.3 µm displacement at the blade mount (Figure 3.7). The 200 µm result was taken as an acceptable displacement yield, since the value meets the design requirements.

3.3.2.2 Notch Flexure Design

The notch flexure, designed for rotational compliance about the x-axis (θ_x), links the displacement from the actuator to the blade. The circular radius on the notch flexure allows for a greater range of motion to sustain the full-range of motion of the piezos without excessively stressing the flexures. Given the maximum material and geometric properties of the flexures, the maximum angular rotation of the notch flexure, α, can be calculated with the following equation. The equation is derived fully in Precision Machine Design [45].

$$\alpha_{notch} = \frac{3MR}{2Ew[\gamma^2 - R^2]}\left\{\frac{1}{\gamma} + \left[\frac{1}{\gamma^2 - R^2}\right]\left[\frac{2R^2 + \gamma^2}{\gamma} + \frac{3R\gamma\left(\frac{\pi}{2} - \tan^{-1}\left(\frac{-R}{\sqrt{\gamma^2 - R^2}}\right)\right)}{\sqrt{\gamma^2 - R^2}}\right]\right\} \quad (3.4)$$

where M is the maximum moment, R is the radius of the notch flexure, E is the elastic modulus, w is the width and γ is geometric property defined by equation 3.5,

where t is the flexure thickness at the center of the radius (the thinnest point).

$$\gamma = \frac{t}{2} + R \tag{3.5}$$

The moment, M, could be found using the material maximum stress using equation 3.6.

$$M = \frac{1}{6} t^2 w \, \sigma_{max} \tag{3.6}$$

Given the maximum stress for 10^6 cycles of aluminum with R = 5 mm, w = 20 mm, t = 2.5 mm, a maximum rotation of 0.0044 radians was found. The placement of the piezo of the piezo 5 mm from the flexure results in a 0.004 radian rotation, which is lower than the maximum rotation, and requires 300 N of force to reach the rotation.

3.3.2.3 Blade Flexure Design

The blade flexures serve two functions. As the piezoelectric actuator expands, the amplification lever rotates about the notch flexure, changing the angle between the amplification lever and the blade mount. The flexures provide rotational compliance, ensuring the system is not over constrained during this actuation. The blade geometry of the flexures also provides a flat surface allowing strain gauge placement. The strain gauge design will be further discussed in Section 3.4, Force Sensing. The design of the blade flexures will be further detailed in this section.

The blade flexure is designed to withstand the rotation between the amplification lever and the blade mount (0.004 radians). The maximum rotation of the blade flexure is derived from equation 3.7 [45], where ℓ is the length of the blade flexure and t is the thickness.

$$\alpha_{blade} = \frac{2 \, \sigma_{max} \, \ell}{E \, t} \tag{3.7}$$

Given a thickness of 1.5 mm and length of 10 mm, the maximum rotation of the flexure is 0.019 radians. This value is lower than the maximum rotation the blade flexures are expected to encounter.

The blade flexure design was also influenced by the natural frequency and the required force for full range of motion. As the compliance of the flexure increases, the natural frequency decreases, which can be detrimental to machines subject to random vibration. The natural frequency of the flexure can be found by modeling the flexure as a simple spring and mass with Equation 3.8 The spring represents the flexure and the mass represents the blade mount and blade. Given the flexure geometry (given above) and the mass of the blade mount, the flexure has a natural frequency of 150 Hz.

$$f_n = \frac{1}{2\pi}\sqrt{\frac{k}{m}} \tag{3.8}$$

where k is the stiffness and m is the mass of the system.

3.4 Force Sensing

There is little literature on the mechanics of powder recoating in PBF. For a first order understanding of the process, powder recoating can be compared to the mechanics of powder lubricants, which are utilized to reduce wear and friction between two surfaces. While dependent on the surface and powder properties, the movement of one surface in relation to the other has been shown to generate a shear force and a normal force [48]. For this reason, it can be assumed that a blade in a PBF system experiences two orthogonal forces during recoating, a shear force in the x-direction, and a normal force in the z-direction (Figure 3.8).

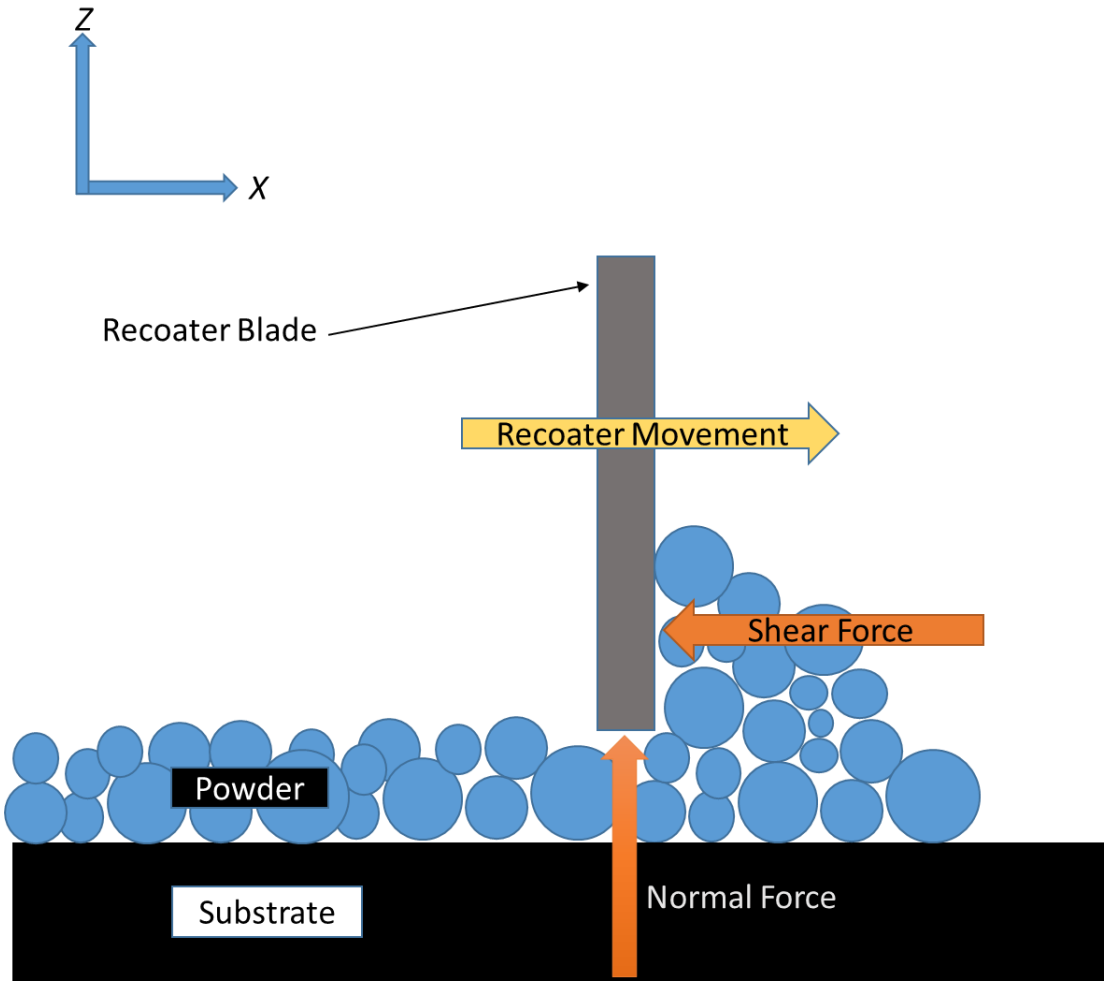

Figure 3.8: Recoater blade forces

These forces have not been measured in an experimental setup. A first order estimate can be found by modeling the powder as a plate with similar density and friction coefficients. The blade must enact enough force on the plate to overcome sliding friction, which is on the order of several *mN*. In a DEM simulation, Parteli [17] predicted forces of tens of mN per meter of a roller. These forces are reliant on several recoating parameters, including blade geometry and compaction force. If the blade is pressed into the powder bed to compact the powder, the shear and normal force will be much greater than if the blade is kept at a fixed height. Furthermore, if the front face of the blade is rounded, the blade will enact a greater normal force for the same shear force.

These force predictions showed that a high-resolution force measurement was required. Force resolution is increased with structural compliance, the strain gauge properties and amount, and the

data acquisition (DAQ) hardware. The design of these properties in the force measurement system will be discussed in this section.

3.4.1 Force Measurement

Force cannot be measured directly, but force can be deduced by measuring strain, which is the change in length divided by the original length of an object. The relationship is given by Hooke's Law.

$$\varepsilon = \frac{\sigma}{E} \tag{3.9}$$

where σ is the stress, E is the Elastic Modulus and ε is the strain. Strain is most effectively measured in an area which experiences the most stress. The most compliant, thus stressed, area in the recoater are the blade flexures. The normal force and transverse force applied to the recoater blade produce an axial and bending stress, respectively. These stresses are related to the force by the following equations:

$$\sigma_{axial} = \frac{F_{axial}}{A} \tag{3.10}$$

where A is the area cross-section of the beam, and

$$\sigma_{bending} = \frac{My}{I} \tag{3.11}$$

where M is the moment, y is the distance from the neutral axis and I is the moment of inertia. Substituting Equation 3.10 or Equation 3.11 into Equation 3.9 gives the strain due to axial and bending loads.

Strain gauges enable the measurement of strain. Strain gauges are bonded to the surface of a structure and have a zigzag pattern of metal foil. The grid maximizes the amount of foil parallel to strain and minimizes any foil orthogonal. As the structure strains, the metal foil strains as well and its electrical resistance changes.

Change in resistance are measured with a Wheatstone bridge, which uses an electric circuit to measure the change in voltage across the bridge. A Wheatstone bridge takes the form of Figure 3.9. Four arms (R_1, R_2, R_3, R_4) can be either the resistance across a strain gauge or a resistor of known resistance. An excitation voltage, V_{in}, is applied across two opposite nodes (nodes *A* and *B* in Figure 3.9). An output voltage, V_{out}, is measured across the remaining opposite nodes (nodes *C* and *D* in Figure 3.9).

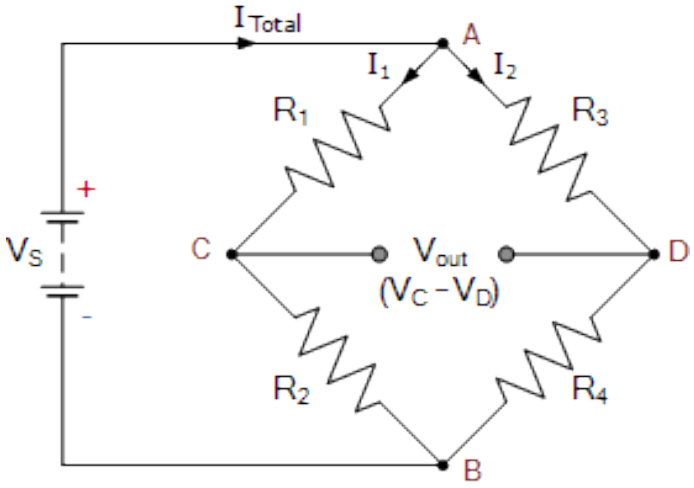

Figure 3.9: Wheatstone bridge diagram [49]

When the bridge is balanced, the voltage output is zero. The change in resistance can be measured in voltage output with the following relationship:

$$V_{out} = V_{in}\left[\frac{R_2R_3 - R_1R_4}{(R_1 + R_2)(R_2 + R_4)}\right] \tag{3.12}$$

The change in resistance of the strain gauge is determined by its gauge factor, *GF*, and is given by the relationship.

$$GF = \frac{\Delta R/R}{\varepsilon} \tag{3.13}$$

Substituting Equation 3.12 into Equation 3.13, the Wheatstone bridge's sensitivity to strain can be determined, given the strain gauge properties, their configuration and the excitation voltage. The strain sensitivity is reported in $\mu V/\mu\varepsilon$. Equations 3.9-11, in conjunction with the strain sensitivity and the analog to digital converter, determine the force sensitivity. The next section will discuss

the design choices for the strain gauge configuration, Wheatstone bridge, and the resulting force sensitivity.

3.4.2 Strain Gauge Configuration and Placement

The blade flexures are designed for strain gauge placement. A higher resolution force can be measured when the beam is more compliant, as a given force will result in more strain. The blade flexures are expected to experience three separate types of strain: a strain from the shear force (bending strain about the y-axis), the normal force (axial strain along the z-axis) and the piezoelectric expansion (bending strain about the x-axis). The placement of the strain gauges and wiring of the gauges into the Wheatstone bridge were designed to maximize the sensitivity of the shear and normal force and minimize the sensitivity to the piezo expansion. The amount of strain gauges also influences the sensitivity.

Strain rosettes were chosen to maximize sensitivity and minimize the amount of strain gauges that needed to be mounted. Strain rosettes (Omega SGD-2/350-RY33), consisting of three strain gauges 45° apart, were mounted on both sides of the blade flexures to maximize resolution. Two strain gauges mounted in the z-direction on each flexure measure axial strains from the normal force on the blade, F_z. The four strain gauges mounted at 45° to the z-axis on each flexure measure bending about the y-axis, which results from the shear force, F_x.

The wiring into the Wheatstone bridge is critical to the strain sensitivity. The axial strain gauges on one flexure are wired into the R_1 and R_2 position, making a half bridge. With the 9.5 V recommended excitation voltage, the Wheatstone bridge has a sensitivity of 9.5 μV/με. This configuration prevents strain from bending about the x-axis, as the signals will be equal and opposite between the two gauges. The four 45° off-axis strain gauges on each flexure are wired to create a full Wheatstone bridge, providing 19 μV/με of sensitivity. Since gauges on either flexure are decoupled, force readings are provided for each side of the blade, which can help determine if the blade is uneven.

The resolution is determined by the DAQ analog to digital converter. A NI- 9237 Bridge Completion DAQ (Part Number: 780264-01) delivers a 50 mV/V input range with 24-bit resolution. With the 9.5 V excitation voltage, the resolution of the DAQ is 28 nV. The resolution, in conjunction with the sensitivities, gives the strain resolution. Substituting the strain resolution

into Equation 3.9-3.11 gives the force resolution. A horizontal force resolution of 4 mN and vertical force resolution of 0.5 mN are expected with the given configuration and components. This resolution is on the same order of magnitude as predicted in the simple plate model and simulations. The strain gauge signal data collection and processing will be discussed in the following chapter.

3.5 Horizontal Linear Motion

A large horizontal motion is required to move powder from the resupply platform to the build platform. Figure 3.10 depicts the actuation system that brings the recoater from the powder supply platform to the build platform. This section will discuss the design choices for the recoater horizontal motion system.

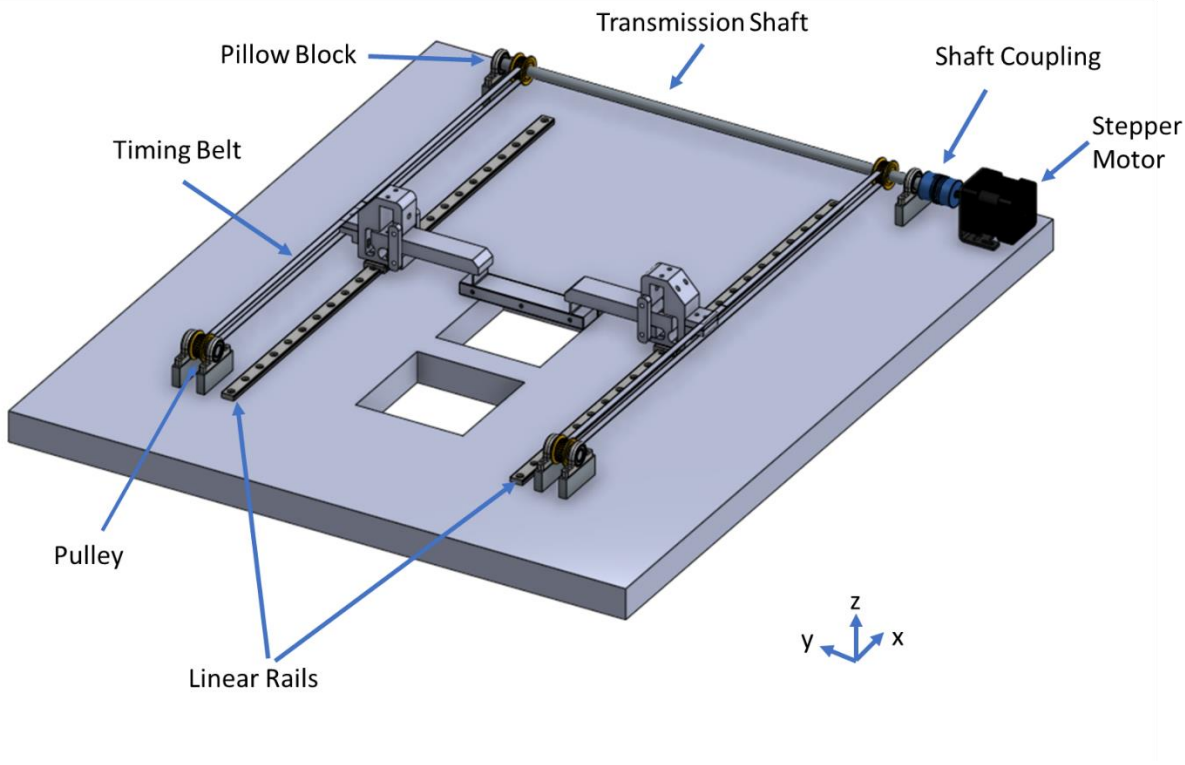

Figure 3.10: Recoater linear motion system

3.5.1 Stepper Motor and Power Transmission

The linear motion system utilizes a single stepper motor (Pololu item #1209) with a holding torque of 141 N-mm. The stepper motor must provide torque to overcome any friction in the linear motion system and to accelerate the recoater to the desired velocity. The friction in the system was assumed negligible since lubricated ball bearings are utilized for rotary and linear motion. The required force was calculated with Newton's Second Law to find the force given the acceleration required to reach the maximum velocity of 150 mm/s within 200 mm (the distance to the powder bed) and the 400-gram mass of the recoater. With a 5 mm-radius pulley, the required torque was calculated as 139 N-mm, which is within the limits of the chosen stepper motor.

The stepper motor transmits power to both sides of the recoater through a transmission shaft. Power is transmitted from the stepper motor to the transmission shaft through a shaft coupling, allowing for misalignment error in the system. A transmission shaft allows a single motor to actuate both sides of the recoater. Both sides of the recoater must be actuated to prevent moments on the linear rails and to minimize the x-position differential on both sides of the recoater. The transmission shaft was sized appropriately to avoid twist, which would cause differential inputs. The amount of twist in the transmission shaft can be found with Equation 3.14.

$$\emptyset = \frac{LT}{JG} \tag{3.14}$$

where L is the length of the shaft, T is the torque it experiences, J is the polar moment of inertia and G is the shear modulus.

With a 9 mm diameter aluminum shaft and 350 mm between timing belts at the full torque of the motor, an angle of twist of 0.003 radians was calculated which results in a 12 μm differential between the timing belts. Given the elastic properties of the timing belts, it was determined that the force generated by this displacement would not exceed the recommended moments for the linear rails. Furthermore, the force from the timing belt differential was used in the error budget (Section 3.6) to determine the error which would result from the load.

Power is transmitted from the shaft to the recoater through timing belts. The timing belts are extended across the powder supply and build platforms through pulleys mounted on both sides of the datum A plate. Clamps connect the recoater to the timing belts. The timing belts are designed to be pretensioned to minimize backlash during load reversal.

3.5.2 Linear Motion Guides

The design utilizes linear guide rails (LinTech MR5WLSUV1P-2-400-10-10) with recirculating ball bearings for linear motion. Ball bearing linear rails offer high precision and minimal internal friction. The key design points of linear rails are their maximum loads, stiffness and precision.

The rails maximum loads are provided by the manufacturer and are based on the load which would cause a permanent deformation of the ball bearings or rails. The maximum loads were on the order of thousands of newtons, therefore the design focused on the rail stiffness. Stiffness is largely influenced by the geometry of the rails, carriage and ball bearings. Due to the height constraint of the HAMR system, the height of the linear rails was minimized. The stiffness of the chosen LinTech rails were estimated based on the diameter of the ball bearings, the maximum loads, and rail width. This stiffness was then used in the error budgeting spreadsheet discussed in Section 3.6.

Linear rail precision is dictated by the surface roughness of the components and the running parallelism of the rails. The running parallelism is defined as the deviation of parallelism between a reference datum surface on the carriage blocks and the linear rail. Running parallelism is dictated by the precision of the grinding process and is typically separated into accuracy grades of normal, high and precision. Precision grade rails were purchased with a 5 μm running parallelism, which was input to the error budget in Section 3.6.

3.6 Error Budget

Error budgets are used to predict the accuracy and repeatability of machines during their operation. An error budget is formed from a kinematic model of the machine at each structural element. At each element, geometric errors and elastic deformations are modeled. The cumulative error is found by defining each structural element spatially with a coordinate system and linking the errors through Homogenous Transfer Matrices (HTM). Five coordinate systems are defined on the recoater (Figure 3.11). The coordinate systems connect to form a closed structural loop.

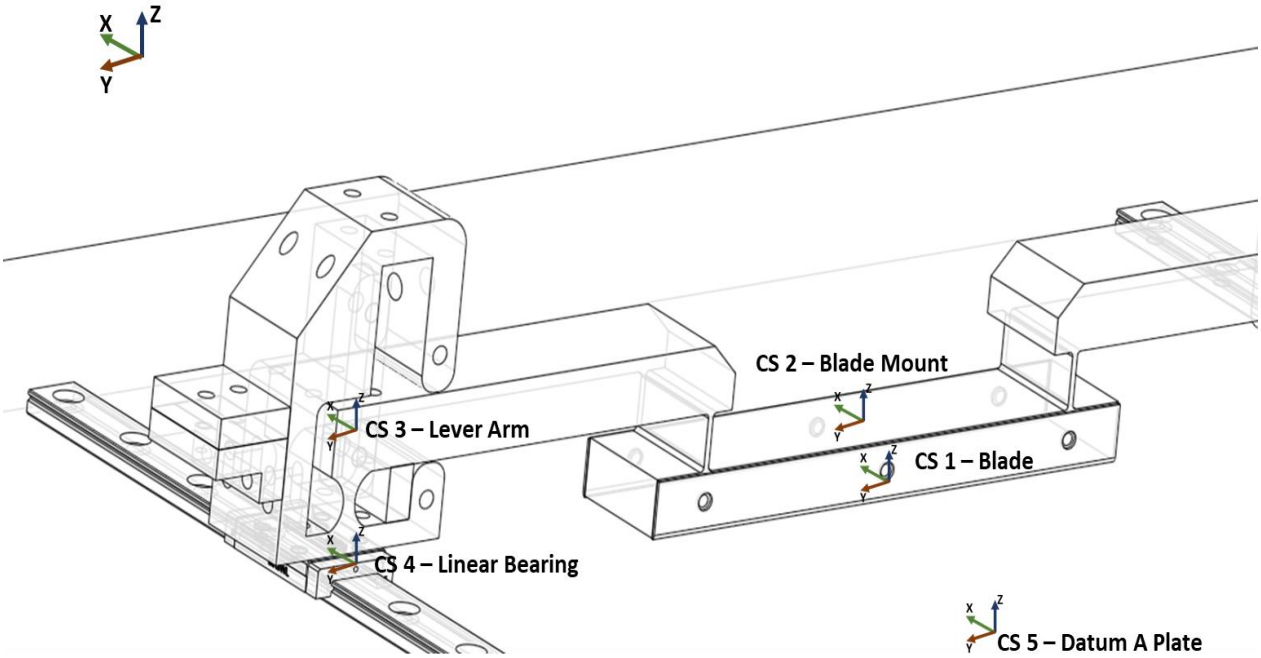

Figure 3.11: HTM Map

For each HTM, rotational and load-induced deflection and geometric errors are approximated at the structural elements and their points of attachment. The geometric errors are given based on the machining process or the process of alignment. Since the recoater blade is aligned to the Datum A plate before operation, geometric error only comes as a result of the linear bearings based on their running parallelism. The stiffness of the structural elements is approximated using first order beam bending equations. At the points of attachment, stiffness is approximated based on the number and type of fasteners. For structural elements connected by a flexure, the stiffness of the flexure is used. Given the stiffnesses and loading condition, rotational and load-induced deflections are calculated at each coordinate system.

The combination of these HTM errors gives the total error of the system. These errors can be combined as a sum, root sum square (RSS), an average of the RSS and sum or the systematic sum. Each combination predicts how the errors may accumulate in the machine and they can be seen as a best, reasonable, realistic and worst-case scenario, respectively. An error budget excel spreadsheet from Professor Alex Slocum (MIT) was used for the error budgeting. The result from the spreadsheet is shown in Table 3.2.

As stated in Section 3.2, the recoater design requires less than 15 μm of error during standard recoating, based on the smallest particle in a standard powder distribution. The error budget predicts less than 10 μm of systematic error and 20 μm of load-induced error in the z-axis, the most critical axis for recoating. The systematic error results mainly from the flatness of the linear rails, which could not be reduced further due to the manufacturer specifications. The load-induced error comes from a 10 N worst-case scenario load in the shear direction, F_x. A 10 N load is unlikely unless a collision occurs, which would likely stop the experiment. Therefore, this error was deemed acceptable.

Table 3.2: Error budget (mm)

	Recoater Error Budget in mm					
All Axes	**Number of axes**	**All axes' Geometric Errors**				**F=kX displacement**
	5	**Random**			**Systematic**	
		Sum	**RSS**	**Avg(SUM, RSS)**	**Sum**	**Sum**
	ΔX	0.0000	0.0000	0.0000	0.0003	0.0411
	ΔY	0.0051	0.0051	0.0051	0.0015	-0.0003
	ΔZ	0.0060	0.0060	0.0060	0.0093	0.0197
	Vector displacement	0.0079	0.0079	0.0079	0.0094	0.0456

This page intentionally left blank

4 MANUFACTURING, CONTROL AND TESTING OF RECOATER

This chapter describes how the instrumented recoater was brought to fruition from the design stage. This process involved manufacturing and assembling the recoater, developing software and controls for each of the devices associated with the recoater and testing each of the individual components to assess their performance.

4.1 Manufacturing and Assembly

All of the manufacturing and assembly for the recoater was done in house at MIT, using the components described. This section will describe this process, such that one could repeat the process if required. The final assembly of the recoater in HAMR is shown in Figure 4.3.

4.1.1 Recoater Manufacturing

Precision components often require tight manufacturing tolerances to meet their design requirements [45]. An OMAX MicroMax, with a repeatability of ± 2.5 µm, was used to meet the geometric tolerances required by the flexures and piezoelectric. Waterjets use a high-pressure jet of water and abrasive garnet to cut through hard materials. Due to the expansion of the high-pressure jet after the nozzle, waterjets produce a taper along the cutting plane. To minimize taper, a higher quality cut was used in critical areas (piezo holder and flexures). The machine minimizes taper by using a slower travel speed and higher-pressure output [50].

A solid block of tight-tolerance aluminum-6061 was aligned underneath the waterjet. Then, a small 20x20 mm cube was cut from the aluminum block with high quality cuts and low-quality cuts on opposing sides. The kerf of the each of the cuts was measured and input into the OMAX. The taper was measured as less than 10 µm for the higher quality cut, which was deemed as acceptable.

After the OMAX input parameters were set and the aluminum block was secured, the entire profile of the recoater was cut. Observation of the profile revealed that several aspects of the recoater

needed to be redesigned for better water jetting results, the largest of which were the blade flexures. An uneven blade flexure thickness was caused by the combination of the high-quality cut, the thin cross-section, and small-radius filets on both sides. These factors required the waterjet to constantly change velocity, especially around corners, leading to uneven cuts. The recoater profile was modified to increase the radius of all filets to a minimum of 1 mm and change all filets to constant radius filets. These changes allowed the waterjet to maintain a constant speed during cutting and yielded much better results.

The waterjet is only capable of cutting in a 2D plane. For this reason, the recoater was fixtured to a Bridgeport mill for machining on the out-of-plane holes and slots. To minimize vibration during machining, the recoater was well fixtured in a clamp and the space surrounding the flexures was filled with a hot glue gun.

4.1.2 Strain Gauge Preparation

Strain gauge mounting required four steps: surface preparation, alignment, adhesion and wiring. This section will discuss this process. The finished configuration of the strain gauges is shown in Figure 4.1.

The blade flexures required extensive preparation before the strain gauges could be mounted. Surface preparation included filing to eliminate taper from the water jetting, smoothing with fine grit sandpaper, and cleaning with isopropanol. Afterwards strain gauges were aligned to the surface and adhered using Loctite adhesive. After the glue cured and the quality was checked, wires were soldered to the solder pads on the rosettes. The wires were then strain relieved by placing a small kink in the wire then gluing the wire to the recoater. Silicone was applied over the rosettes to seal the strain gauges, ensuring powder would not affect their resistivity.

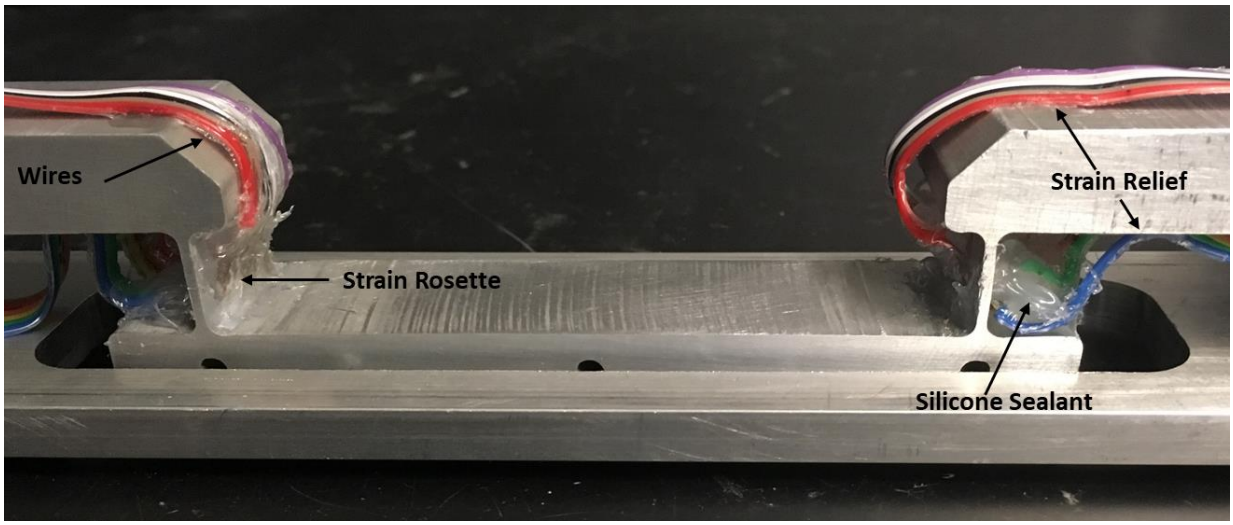

Figure 4.1: Strain gauge preparation. Strain rosettes are on both sides of the blade flexure.

4.1.3 Assembly

Assembly required adding the piezoelectric actuators, fasteners, securing plates and timing belt clamps to the recoater. Figure 4.3 shows the assembled recoating system. This section will describe this process.

The piezoelectric actuators were preloaded in the recoater piezo holders. The preload ensures the piezos always have two points of contact with the recoater and there is no lost displacement as the piezos expand. Preload was provided with the recoater holder, by oversizing the height of the object inserted using shim stock. A spreader was used to open the recoater holder so the shim could be inserted (Figure 4.2). The piezo and shim were glued in place with epoxy to prevent the components from shifting.

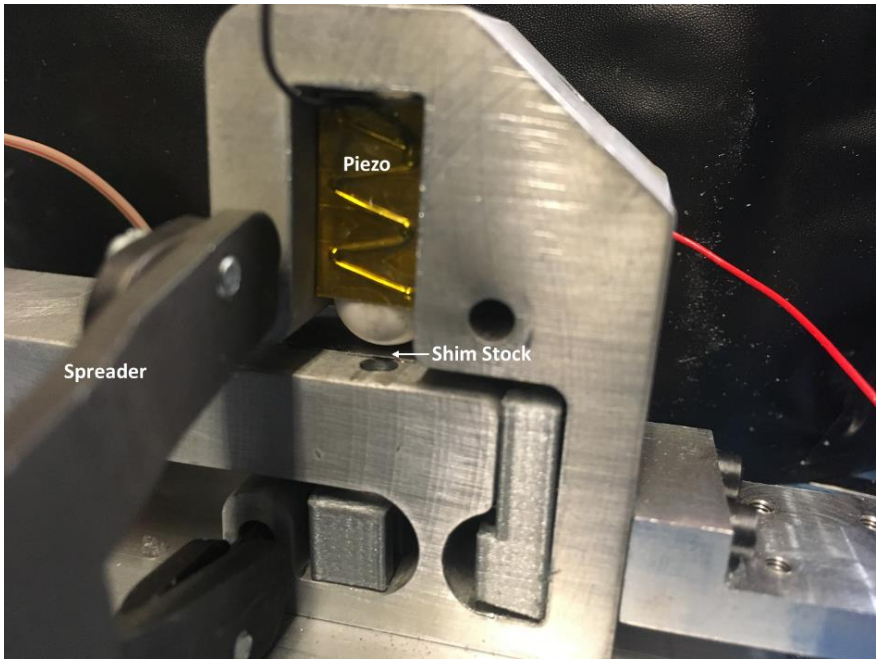

Figure 4.2: Piezo assembly in the recoater holder. Here the spreader is opening the recoater holder so the shim stock can be inserted.

To further stiffen the piezo holder and mitigate powder contamination of the recoater, 5 mm aluminum cover plates were added to both sides of the holder. Fasteners were inserted across the plates, then preloaded to the recommended seating torque provided by the manufacturer. The preload guarantees the recoater holder joint stiffness, such that the plates bear load from the piezo expansion.

The rails were aligned to the recoater through zippering. Zippering involved loosely fastening the linear guide rails to the datum plate then fastening the recoater to the linear rail carriages. As the recoater is slid linearly, the fasteners on either side are tightened. Zippering ensures that the system is not over constrained along the linear rails during recoating.

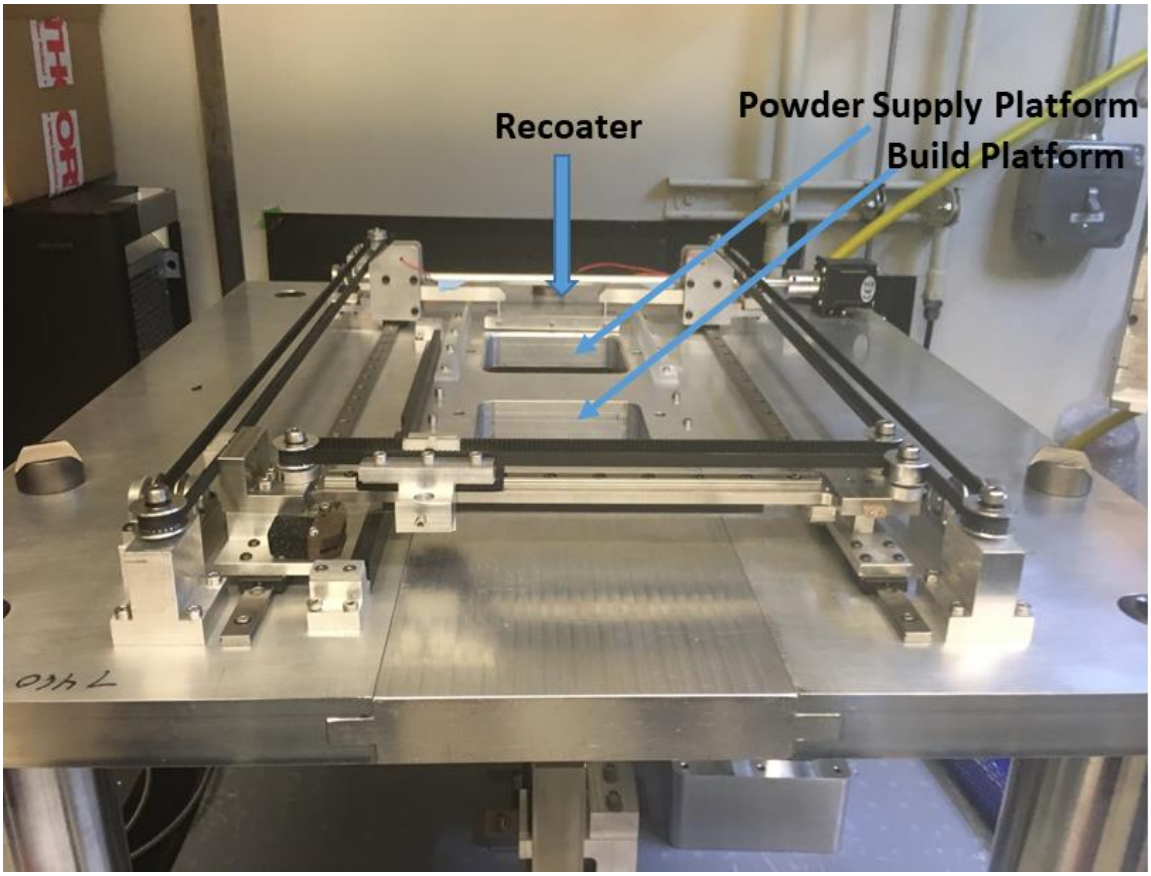

Figure 4.3: HAMR assembly

4.2 Controls and Software

There are three separate devices, which require or produce a signal, associated with the instrumented recoater. The piezoelectric stack actuators control the vertical positioning of the blade. The stepper motor controls the horizontal motion of the recoater. The strain gauges measure the shear and normal forces on the blade. All of these devices are controlled or monitored from a central computer next to HAMR. This section will describe the signal acquisition and generation hardware and software. A summary of these devices, hardware and signals can be seen in Table 4.1.

Table 4.1: Recoater electronic devices summary

Signal In/Out	Device	Hardware	Signal
Out	Piezoelectric stack actuators	NI-6211/ PiezoDrive	0-10 V/ 0-150 V
Out	Stepper motor	TinyG	G-code
In	Strain gauges	NI-9263	50 mV/V

4.2.1 Piezoelectric Actuator

The piezoelectric actuator converts a voltage input into a positive displacement. The derivation of the relationship transfer function from voltage to displacement can be seen in Chapter 3, section 3.3.

An NI-6211 controller provides a 0-10 V signal, which is amplified by the PiezoDrive to a 0-150 V signal. The recoater piezos operate with an input 0-150 V and a maximum theoretical output of 200 μm at the blade mount. Without a load, the blade positioning system operates with a transfer function of 1.3 $\mu m/V$. The transfer function was measured and reported as 0.48 $\mu m/V$ in Section 4.3.

The piezo was run open loop using this transfer function. Open loop control means no feedback loop verifies the actual position versus the commanded position. Open loop control was required, since no compact method to accurately measure the position of blade was found.

Open loop control, while simpler, complicates accurate blade positioning. The hysteresis present with piezoelectric actuators, as illustrated in Figure 4.7, makes this aspect more challenging. The hysteresis of the entire system was measured using a laser profilometer, discussed in Section 4.3. A map of the system hysteresis allows the user to account for hysteresis and accurately position the blade.

The piezoelectric controls are also complicated by system noise. A challenge of using piezoelectric actuators is that any electronic noise in the system causes the actuator to move [51]. To minimize

this noise, an ultra-low noise driver (PiezoDrive PDu150) was chosen to drive the piezoelectric actuators. This driver functions as both a signal conditioner and an amplifier, converting the 0-10 V input from the NI-6211 controller to a 0-150 V output at high resolution (20-bit). The piezo driver specifies a noise level of 26 μV. The electrical noise translates to a 57-pm mechanical noise at the actuator, which can be assumed negligible.

4.2.2 Stepper Motor

A stepper motor uses electromagnetism to control the exact position of its rotor. A pulse of electricity turns the device a precise distance. A waveform, which is a determinate amount of electric pulses at a specific rate, can be sent to the motor. The waveform allows stepper motors to be used for open loop control confidently for speed and position [45].

The TinyG, a USB based Computer Numerically Controlled controller, was used to control the stepper motor for the recoater and the ink jet. G-code, a numerical control programming language, is used to communicate with the TinyG. G-code commands contain information such as the motor to be moved, the distance to be moved and the velocity [52]. The TinyG translates then executes the G-code commands. Tuning the TinyG to machine specific parameters, such as pulley-diameter, allows for accurate movement.

A LabVIEW program (Figure 4.4) was created to communicate with the TinyG controller from the hub computer for the recoater linear motion. The LabVIEW program establishes USB communication (upper left Figure 4.4) with the TinyG and then can be used to read and write commands (right side Figure 4.4). The program enables a simpler user-interface, where the user may tune the recoater velocity (lower left Figure 4.4) then run the program. The LabVIEW program will tell the TinyG in sequence to set the home position, the recoater's current position, move the recoater 310 mm (this moves the recoater within 1 cm of the inkjet home position) at a determined velocity, then return to the home position at the same velocity. The program can also be used to calibrate the TinyG using a saved .txt file and communicate with the ink jet system.

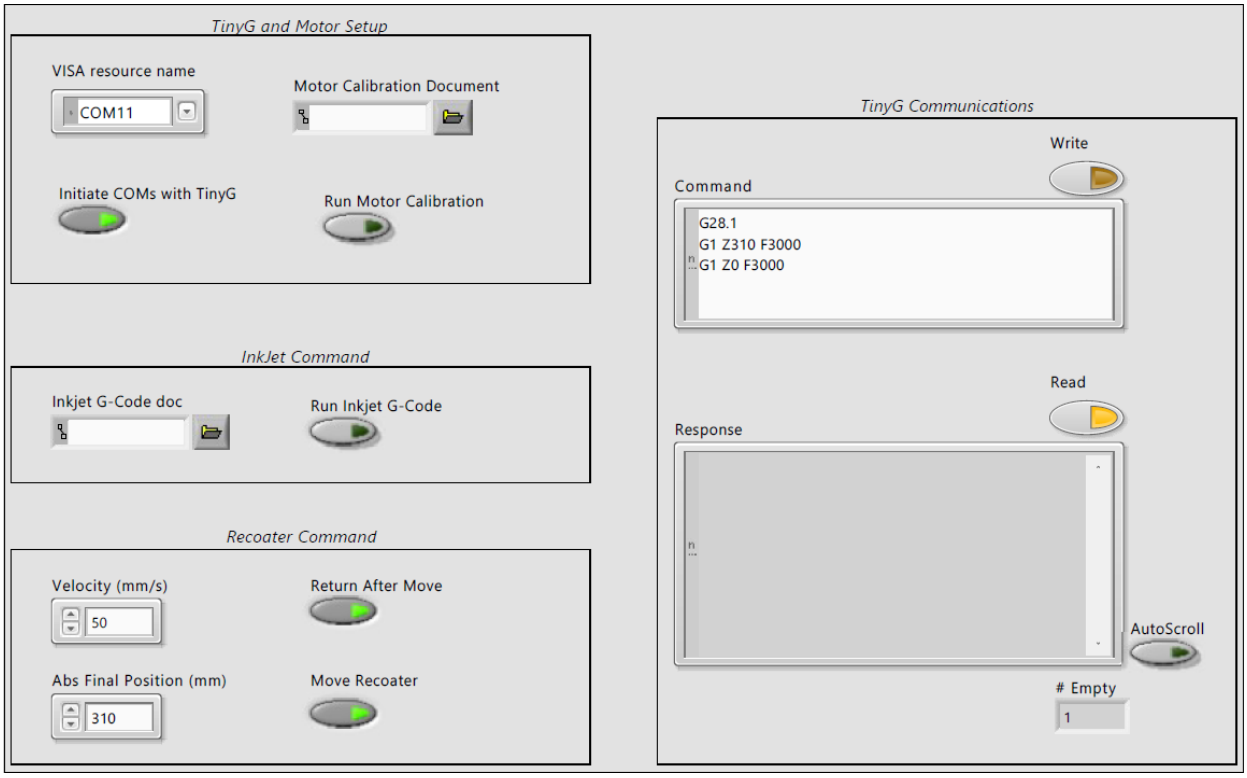

Figure 4.4: LabVIEW front panel of TinyG control

4.2.3 Strain Gauge Signal Acquisition

Twelve independent strain gauges are mounted on the recoater. Wires connect the solder pads on the strain gauges to a Wheatstone bridge. Two center-mounted gauges on each side of the recoater, four total, are attached to half bridges. Four off-axis mounted gauges on each side, eight total, are connected to full bridges.

An NI-9263 Bridge Input Module from National Instruments interfaces with each of the Wheatstone bridges to measure the voltage (strain) across the bridge. The NI-9263 provides the excitation voltage for the four bridges and measures the signal voltages across the bridges. The signal voltage is converted to a digital voltage with a 24-bit analog-to-digital converter (ADC) on the 9263. The NI-9263 is slotted into a cRIO-9076 CompactRio Controller. The cRIO-9076 is configured with a Field Programmable Gate Array (FPGA), which enables a 50 kHz data sampling rate.

The voltage data points are filtered and recorded with a LabVIEW Virtual Instrument (VI). To reduce signal noise, the points are averaged over 100 points in the FPGA. The data is then

transferred to another LabVIEW VI on the computer, which allows for more complex data processing, such as zeroing the signal, computing a moving average and recording the data to a Microsoft Excel spreadsheet.

The front panel for this LabVIEW VI is shown in Figure 4.5. The panel is separated into three boxes by functionality. In the top left box labeled setup, the user connects to the FPGA and can zero the signals. The box on the right provides charts for the voltages of each Wheatstone bridge and allows the user to set the transfer function from voltage to force. The bottom left box labeled measurement allows the user to export all four signals to an Excel document. This VI is used in Section 4.4 to take measurements for the strain gauge calibration.

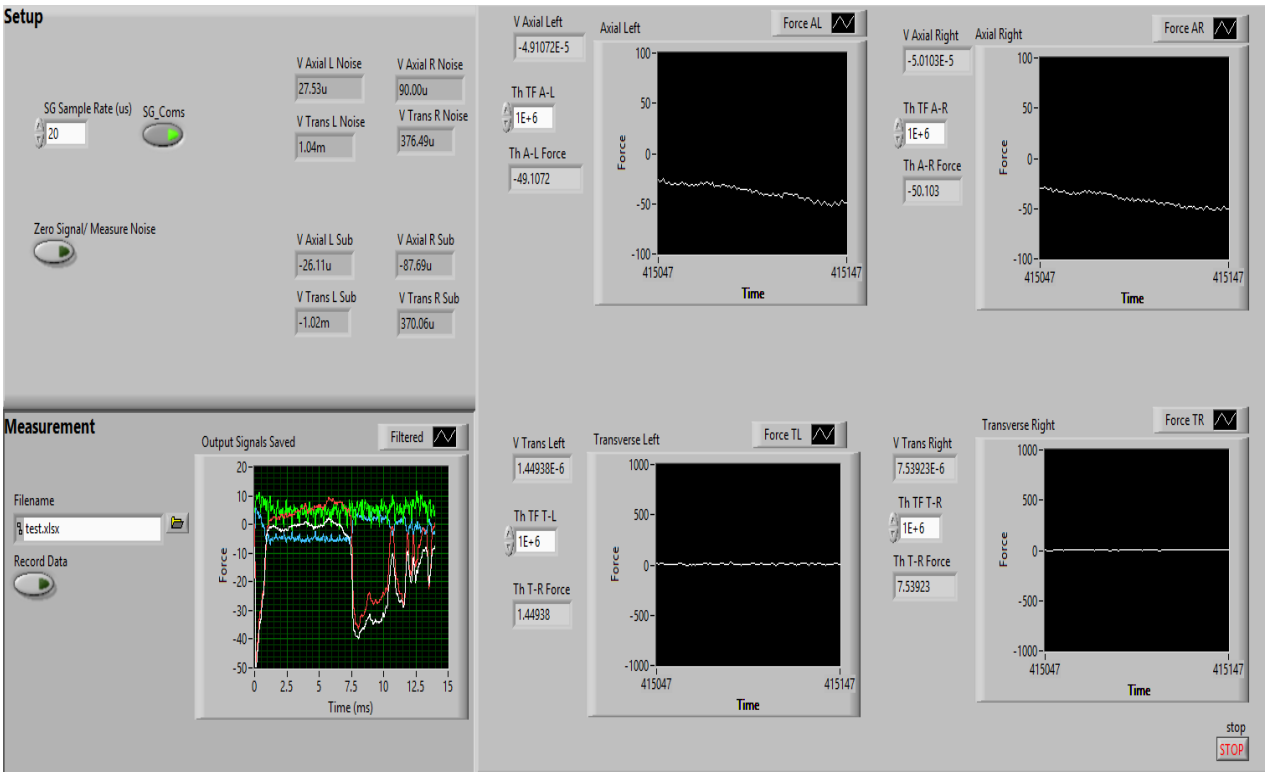

Figure 4.5: LabVIEW front panel for force measurement

4.3 Blade Positioning Validation

The blade positioning capability was tested with a Keyence 2D Laser Displacement Sensor (LJ-G5000). The device was utilized to record vertical position along a 2D path on the blade mount for each commanded piezo voltage. The 2D path allowed the average height and peak heights along the blade mount to be measured. With these values, the transfer function between input

voltage and output displacement was determined. This transfer function is necessary for spatial control of the blade mount.

4.3.1 Experimental Setup

The test configuration is shown in Figure 4.6. For the test, the recoater was fastened to a custom-built aluminum securing plate. The securing plate limited the rotation of the piezo holder such that the test configuration mimicked the operational configuration, where the recoater is secured to the linear rail carriages. The displacement sensor was adjusted within range above the blade mount, signified by a green light on the Keyence. After alignment, the output voltage to the piezos was adjusted using a potentiometer in circuit with the PiezoDrive controller. Output voltage was scaled in 20 V increments across the entire 150 V range. At each increment the average height and height on either side of the blade mount were read from the Keyence.

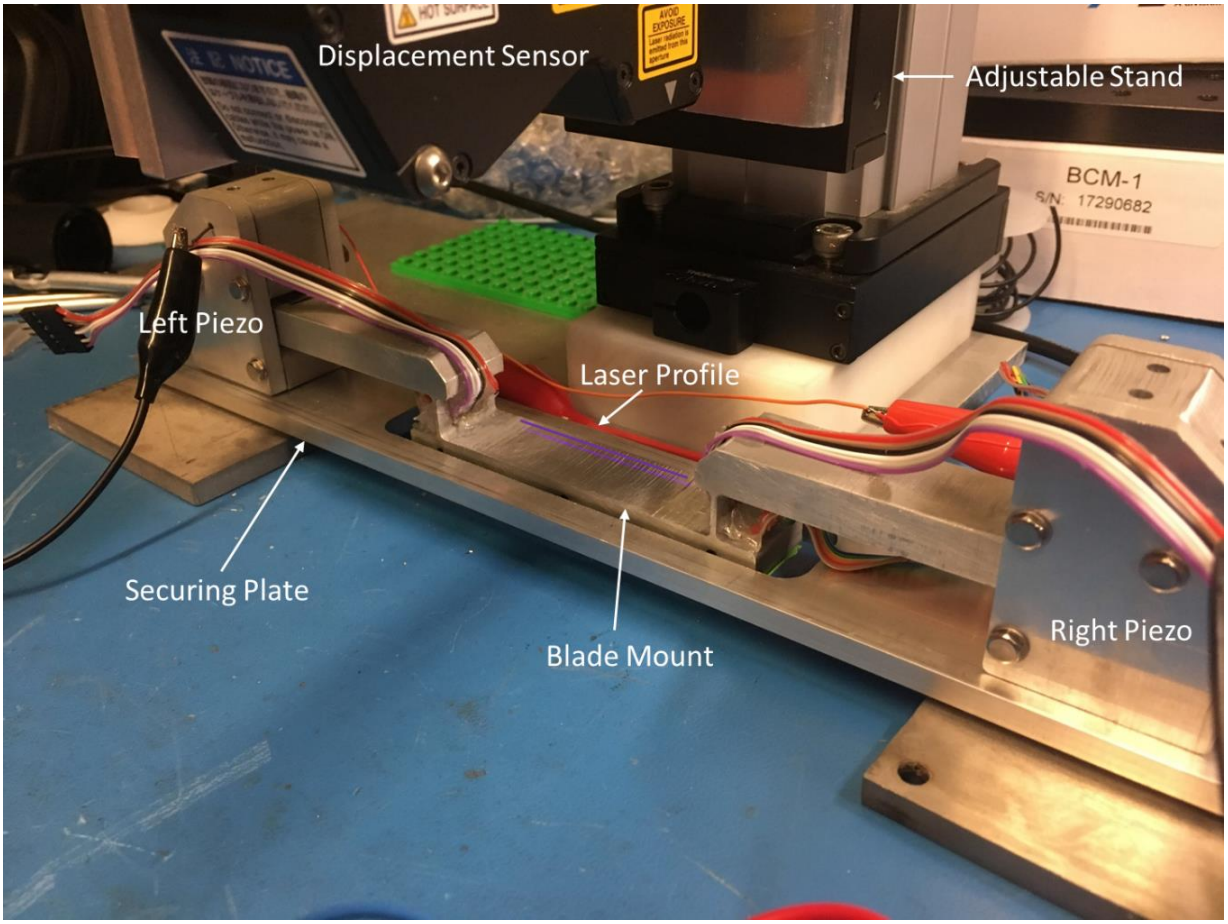

Figure 4.6: Test setup of the 2D displacement sensor

4.3.2 Blade Positioning Results

The average height of the blade mount vs. the voltage bias across the piezos is shown in Figure 4.7. Two different lines signify the blade displacement as the voltage is increased from 0-150 V and the voltage is decreased from 150-0 V. The offset between these lines illustrates the hysteresis in the system, which is common with piezoelectric stack actuators.

At the maximum displacement, the blade mount moves 69 µm. The measured displacement is a fraction of the theoretical 200 µm. Possible reasons for this discrepancy and design improvements will be discussed in Section 4.3.3. With the given displacement, the transfer function for the blade displacement is 0.4865 $\mu m/V$ as the voltage is increased and 0.4667 $\mu m/V$ as the voltage is decreased. Using these transfer functions will set the blade within a few microns of its actual position.

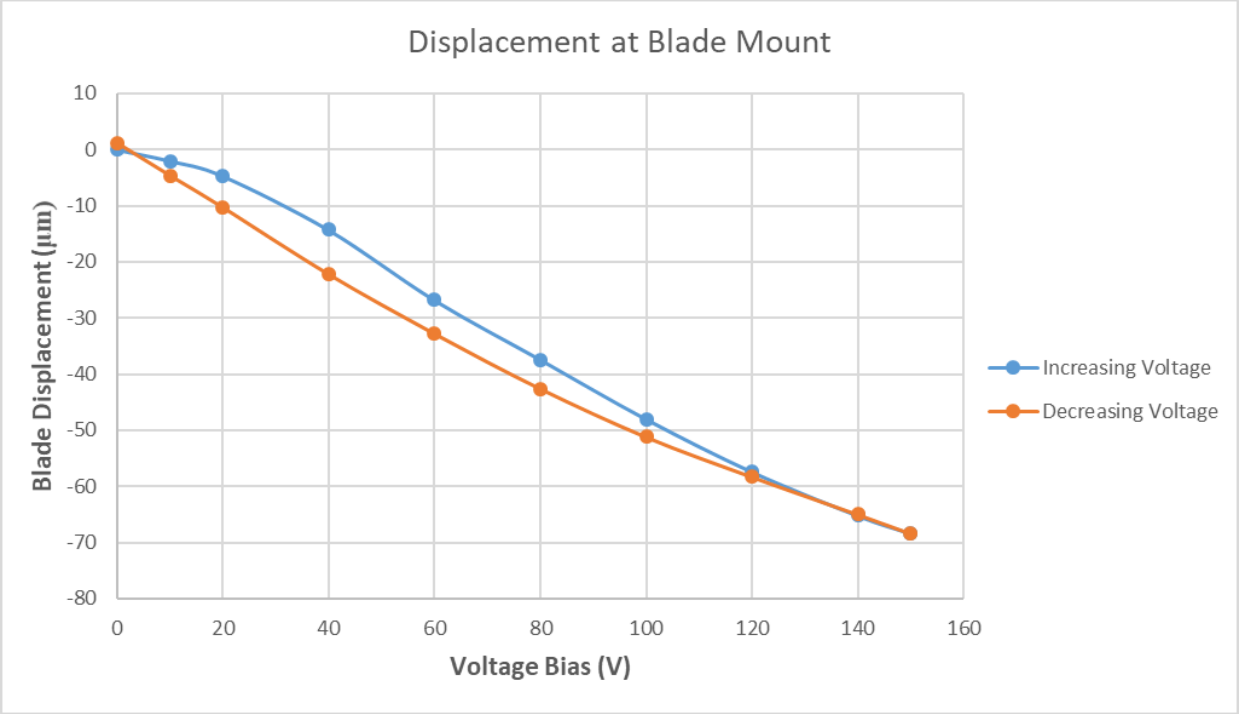

Figure 4.7: Blade displacement map

Variability in the piezos and their mounting configuration can affect the output of the piezo. Therefore, the difference between the output of the two piezos was measured. Figure 4.8 shows the displacement at the right of the blade mount versus the left. The differing output from the two piezos results in a maximum 9 µm discrepancy at 150V. The maximum output of the right piezo is 72.5 µm, whereas the left piezo is 63.8 µm

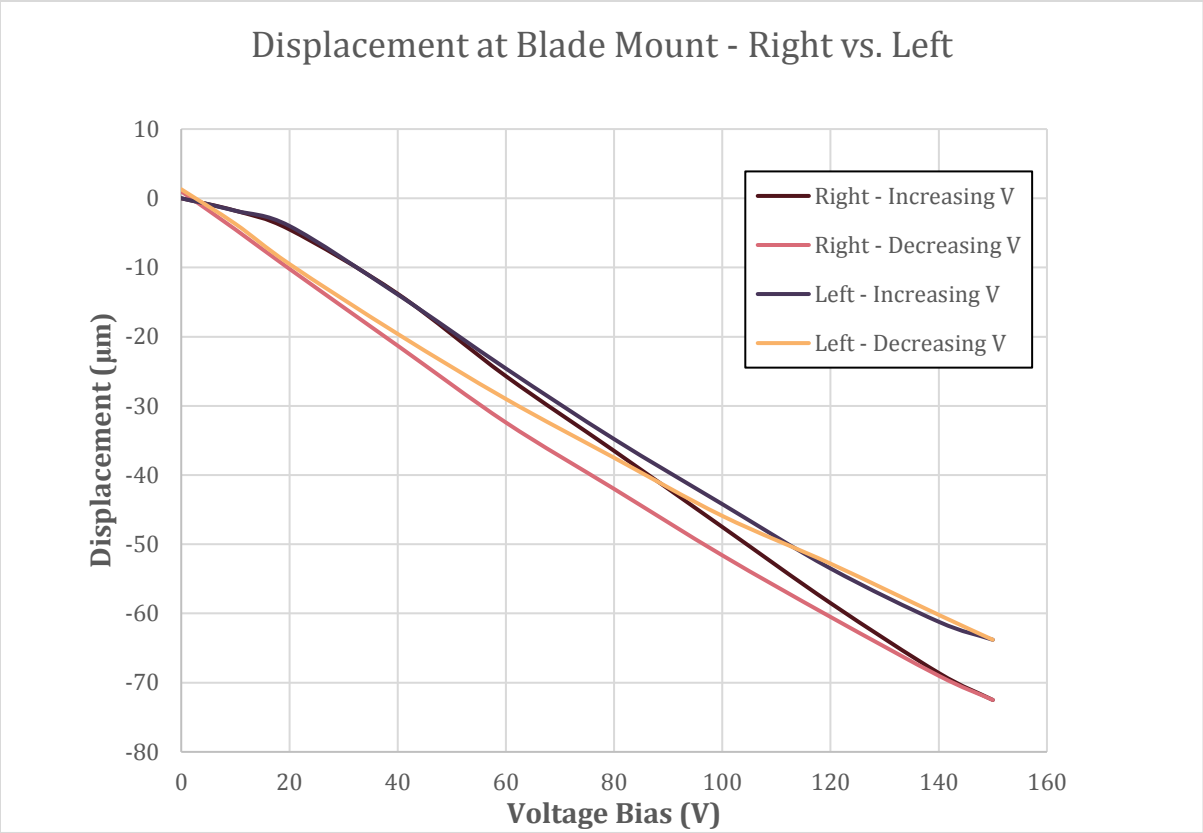

Figure 4.8: Displacement differential at the blade mount

Differential voltage inputs can be used to eliminate the discrepancy between the two piezos. The voltage inputs required for each piezo can be determined using their respective transfer functions. The transfer function of the right piezo is $0.5102\ \mu m/V$ with increasing voltage and $0.4942\ \mu m/V$ with decreasing voltage. The transfer function of the left piezo is $0.4545\ \mu m/V$ with increasing voltage and $0.4329\ \mu m/V$ with decreasing voltage. A summary of these transfer functions is presented in Table 4.2.

Table 4.2: Transfer functions for displacement at the blade mount for the blade positioning system

	Average ($\mu m/V$)	Left ($\mu m/V$)	Right ($\mu m/V$)
Increasing voltage	0.4865	0.4545	0.5102
Decreasing voltage	0.4667	0.4942	0.4329

The transfer functions for increasing and decreasing voltage are only required for relative positioning, where hysteresis plays a significant role. When setting the absolute position of the blade, the hysteresis can be ignored and only one of these transfer functions is required. The hysteresis can be overcome by simply resetting the piezo to one of its extreme values (0/150 V) and using the corresponding transfer function, depending on whether voltage is increased or decreased, to reach the desired absolute position.

4.3.3 Sources of Lost Displacement and Potential Design Improvements

Research in piezoelectric lever systems has shown that these systems often may not achieve their full theoretical displacement due to factors such as surface roughness at the piezo mounting surface, flexure deformation in off axes and misalignment of the actuator or flexures [53]. To troubleshoot the displacement, several scenarios were run in FEA.

The previous FEA model was altered such that a fixed displacement (18.4 μm) instead of a force (previously performed in Chapter 3) was applied at the lever arm. This loading condition replicates a scenario in which the piezo is over-constrained due to a fixed contact point between the piezo and lever arm. The results from the FEA are shown in Figure 4.9. Figure 4.9a displays the displacement yield at the blade mount. The displacement results were 67 μm at the blade flexure and 63.5 μm at the center of the blade mount, which are strikingly similar to the experimental performance of the instrumented recoater.

Figure 4.9b is a map of the strain in the notch flexure. The figure illustrates why the given loading scenario yields much less displacement. Since the contact point between the piezo and lever arm are fixed, the notch flexure must deform laterally, leading to elastic deformation, and thus lost displacement, in the flexure.

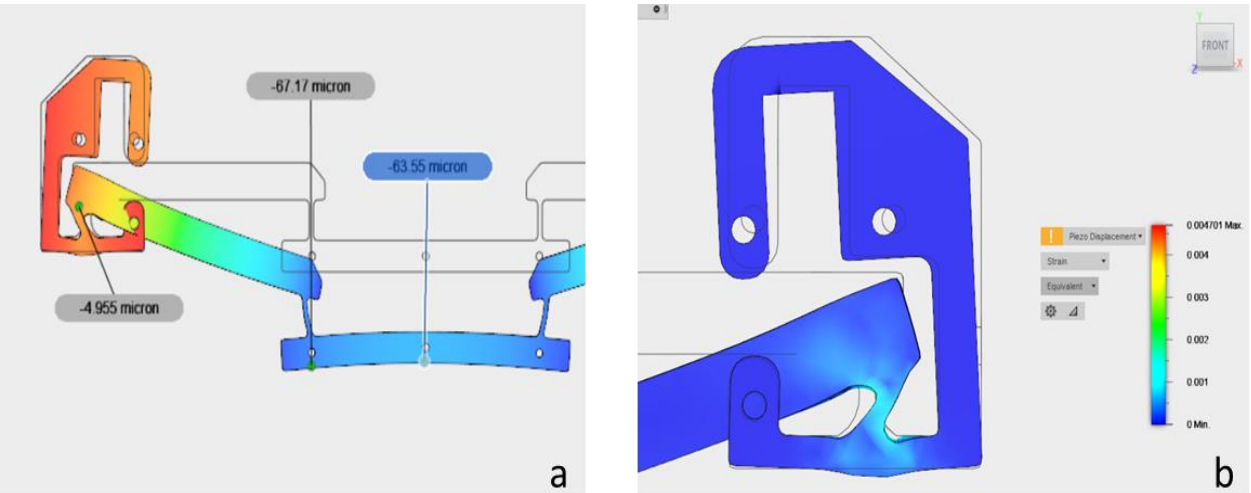

Figure 4.9: Input displacement based FEA results (a) displacement (b) strain

In the instrumented recoater, the contact between the piezo and lever arm is a ceramic hemisphere on a steel shim stock. The current configuration was chosen based on the manufacturers operation recommendation (Figure 4.10a) [54]. In theory, the configuration should not be over-constrained as it allows for changing contact point during its range of motion. As the notch flexure, thus lever arm, rotates, a new contact point is made on the piezo hemisphere.

Piezo-flexure amplification systems in literature, however, rarely utilize this type of contact [47], [55], [56]. A more common approach is another flexure in between the piezo and lever arm (Figure 4.10b). This configuration may be designed into future iterations of the recoater to increase the displacement yield, but it should be noted that adding an additional flexure would make the design much more compliant.

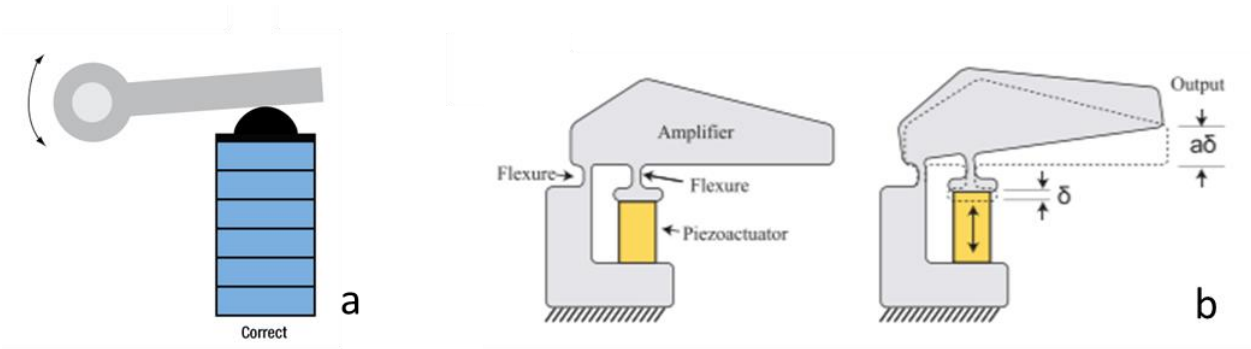

Figure 4.10: Piezo configuration [54] **(a) hemisphere contact** [54] **(b) flexure contact** [56]

4.4 Force Sensing Calibration

To calibrate the strain gauges, known loads in six loading conditions were applied and the strain was recorded. Loads were applied using precision scale calibration weights. Loading conditions applied a compressive force in the Z direction (loading condition 1-3) and a tangential force in the X direction (condition 4-6) above each one of the bolt-holes on the blade mount, since the bolts are centered beneath and between the flexures. These loading conditions allowed tangential (condition 4,6) and compressive forces (condition 1,3) to be isolated on individual flexures to account for geometric differences between them. Conditions 2 and 5 established the transmission of forces between the two flexures (Figure 4.11).

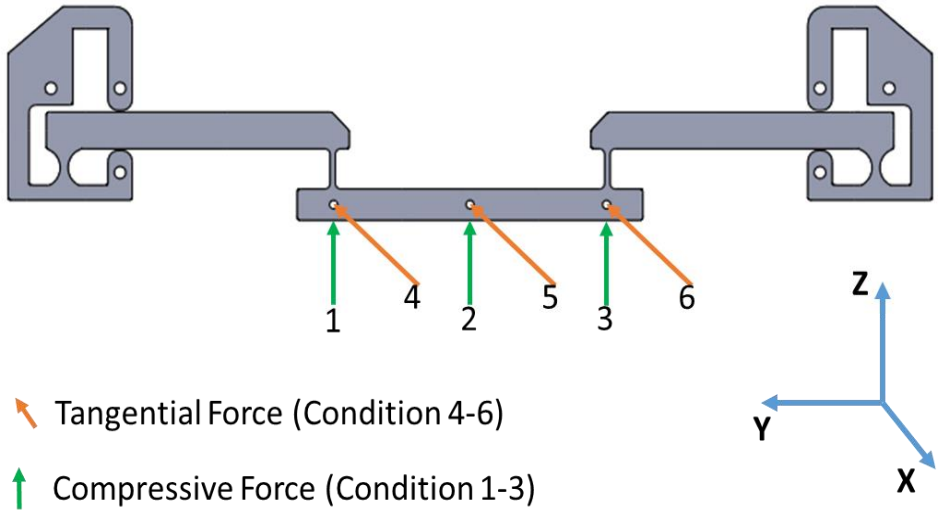

Figure 4.11: Strain calibration loading conditions

4.4.1 Theoretical vs. Actual Strain

After analyzing the normal force measurement files, it was determined that the axial measurements had lower sensitivity than expected. To troubleshoot the issue, the Wheatstone bridges were reconfigured by switching the position of the signals in the bridge, such that the bending strain instead of the axial strain was measured. The loading procedure was completed with a 20 gram weight with one flexure wired to measure axial strain and the other to measure bending strain.

A comparison of the signals is shown in Figure 4.12. The figure shows that the bending strain signal is much larger than the axial strain signal in normal loading conditions 1-3. The high bending strain is likely due to the rotational compliance at the notch flexure. When a normal load is applied to the blade mount, the mount translates, altering how the blade flexures absorb the load.

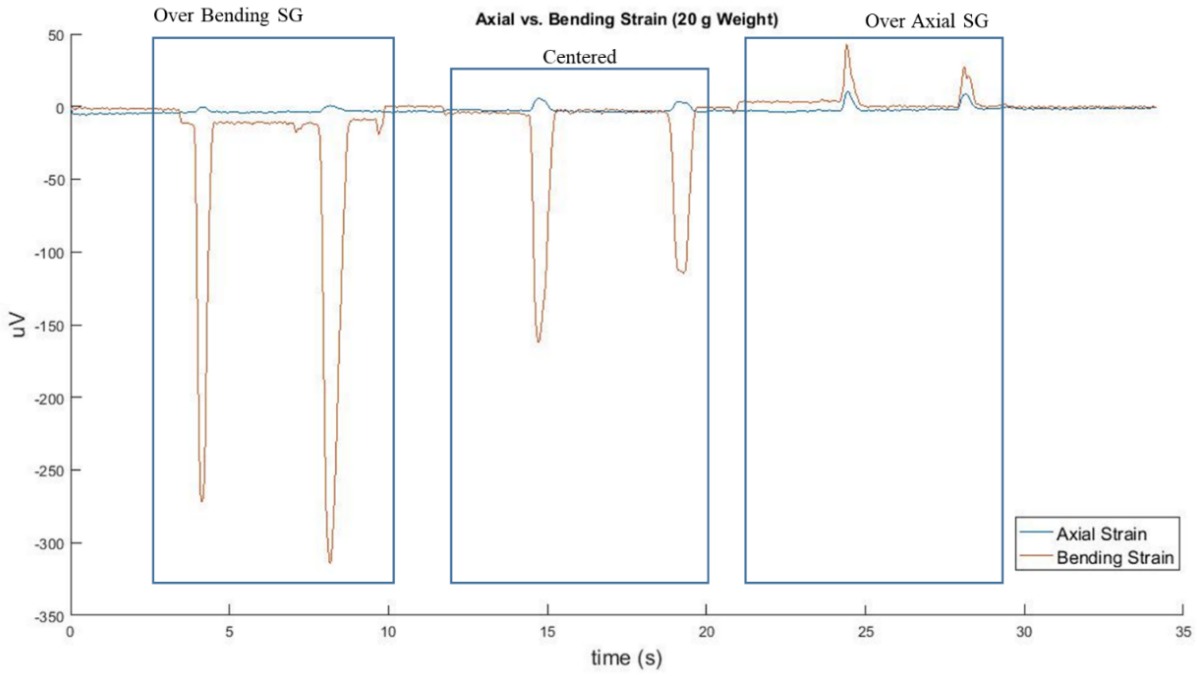

Figure 4.12: SG measurement axial vs bending

These assumptions were confirmed with an FEA simulation designed to replicate the shear and normal loading conditions. The FEA results are shown for loading condition 1 and 4 in Figure 4.13. As the figure shows, the utilization of a lever-type flexure system leads to large deformations at the notch flexures instead of the blade flexures. The blocking force of the piezoelectric actuator was designed to prevent this deformation, but this connection may not be as stiff as expected due

to reasons discussed in Section 4.3.3. The deformation explains the large bending strain in the normal force strain measurements and the load position dependence of the shear force strain. Due to this issue, the axial Wheatstone bridges were reconfigured to read bending strain and the calibration efforts were directed towards bending strain.

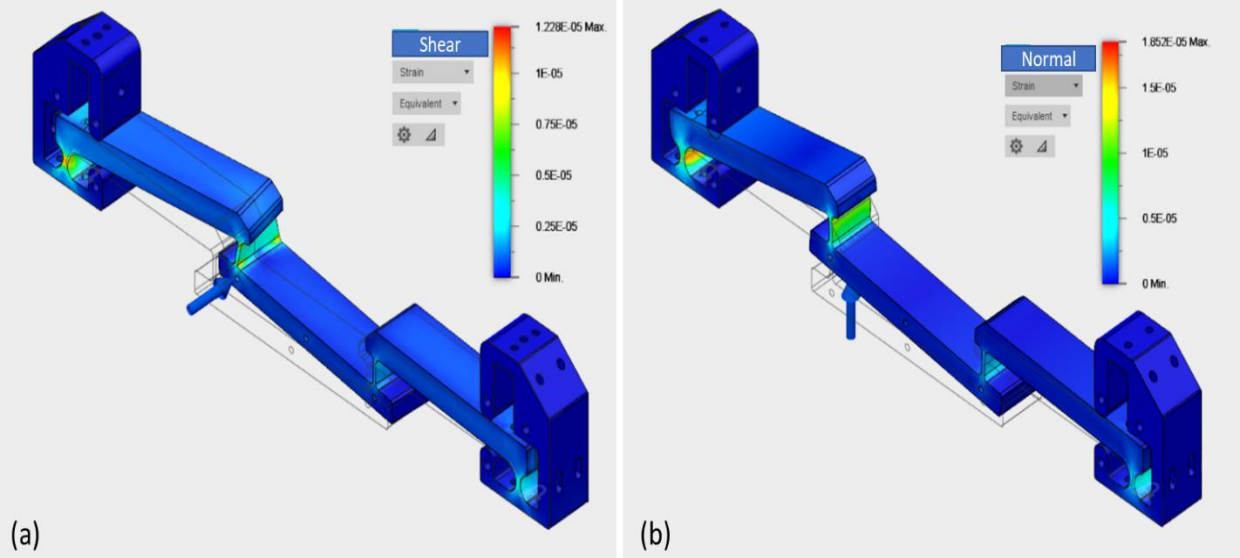

Figure 4.13: FEA for condition 1 and 4 (a) shear load (b) normal load

4.4.2 Normal Force Calibration

Data was collected using the LabVIEW program described in Section 4.2.3. The LabVIEW program was started, the signal was nulled, and the weight was moved through loading conditions 1-3 (Figure 4.11). One, 2, 5, 10, 20 and 50-gram weights were used. Figure 4.14 shows the experimental setup with the 20-gram calibration weight and the marked loading positions.

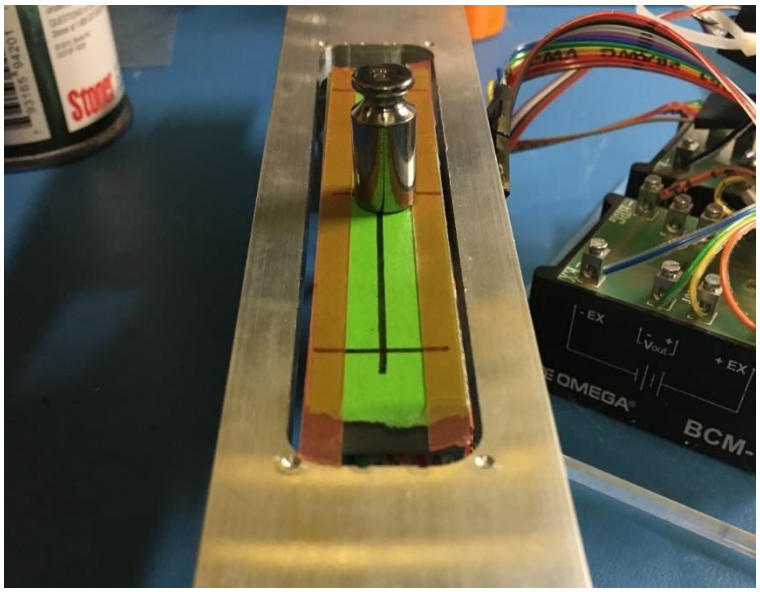

Figure 4.14: Calibration setup to measure the strain from normal loads

The voltage from the half Wheatstone bridges was plotted against the applied force. The bending strain, and thus the transfer function from voltage measured to force applied, varies based on the position of the load. The transfer functions were calculated for the three loading scenarios: the load is over the blade flexure, the load is centered, and the load is over the other blade flexure. These results are plotted in Figure 4.15. Based on the figures, it is clear that the highest force resolution is achieved when the load is placed directly on a flexure. In this scenario, a 0.01 N force can be registered.

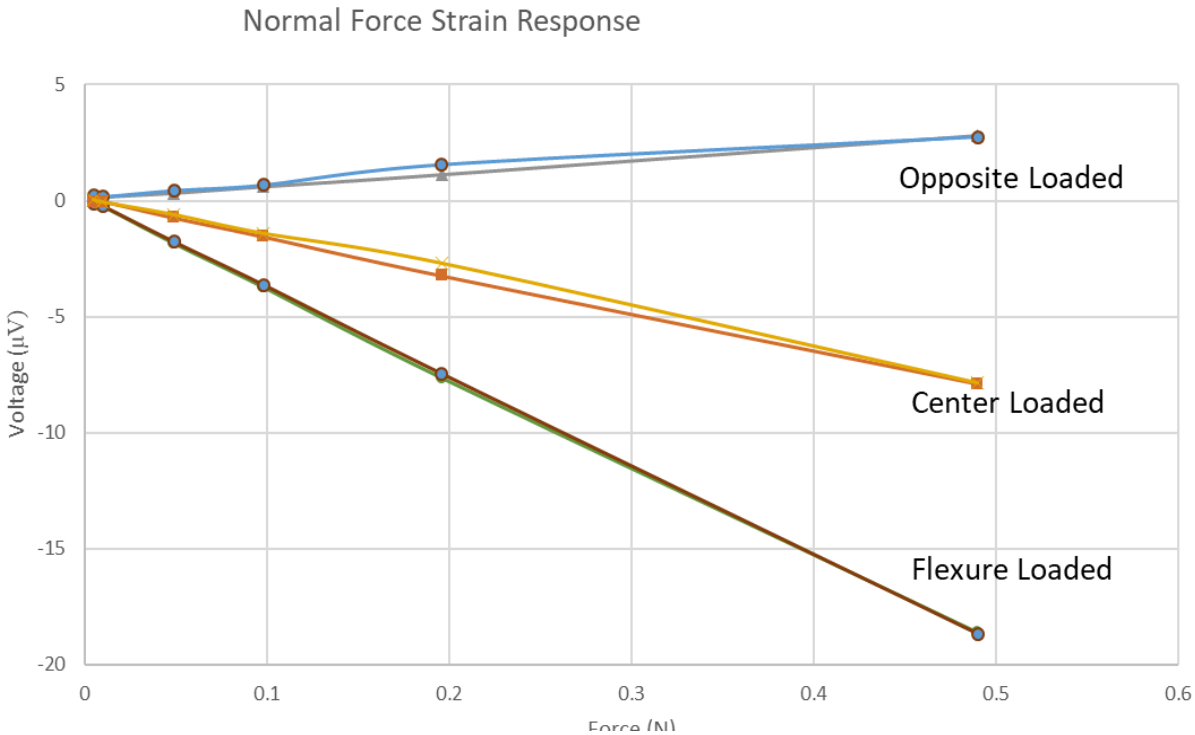

Figure 4.15: Normal force strain gauge response. The lines represent when the load is on the blade mount over the flexure, in the center and when the load is over the opposite flexure.

The transfer functions for the various loading conditions are summarized in Table 4.3. The transfer functions from voltage to force are loading condition dependent. The combined transfer function, which is the sum of the transfer functions, is independent of the loading condition and always remains the same. Therefore, for first order force measurement, the signals from both flexures can be combined and the combined transfer function can be used.

Table 4.3: Normal force transfer functions

	Left (µV/N)	**Mid (µV/N)**	**Right (µV/N)**
Transfer Function (Right Flexure)	5.6	-16.3	-38.3
Transfer Function (Left Flexure)	-38.4	-16.2	5.3
Combined Transfer Function	-32.8	-32.5	-32.9

4.4.3 Shear Force Calibration

The setup for shear force strain measurements was similar to the normal force setup, except that weights were hung from the blade mount. Fifty, 70, 90, 110, 130, 150-gram weight were used. Weights were hung on the edge of the blade mount at each of the flexures and at the center of the blade mount. Figure 4.16 illustrates the shear force calibration setup with the 150-gram weight at the center position on the blade mount.

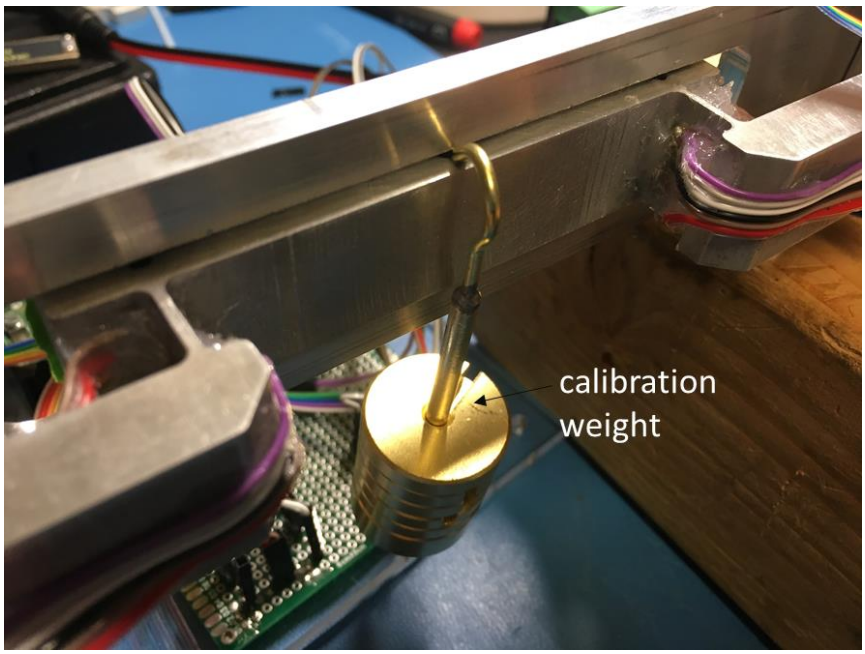

Figure 4.16: Calibration setup to measure the strain from shear loads

The voltage from the full Wheatstone bridges was plotted against the applied shear force, shown in Figure 4.17. The shear force strain response was very similar to the normal force strain response, but slightly less sensitive to applied loads. The shear load causes twisting of the blade mount as discussed in Section 4.4.1, causing the strain response to vary based on the loading condition. The strain response is highest when the flexure is loaded directly. The strain response from the direct flexure loading conditions are offset between the two flexures. The offset is likely due to geometric variations in the recoater or the mounted strain gauges.

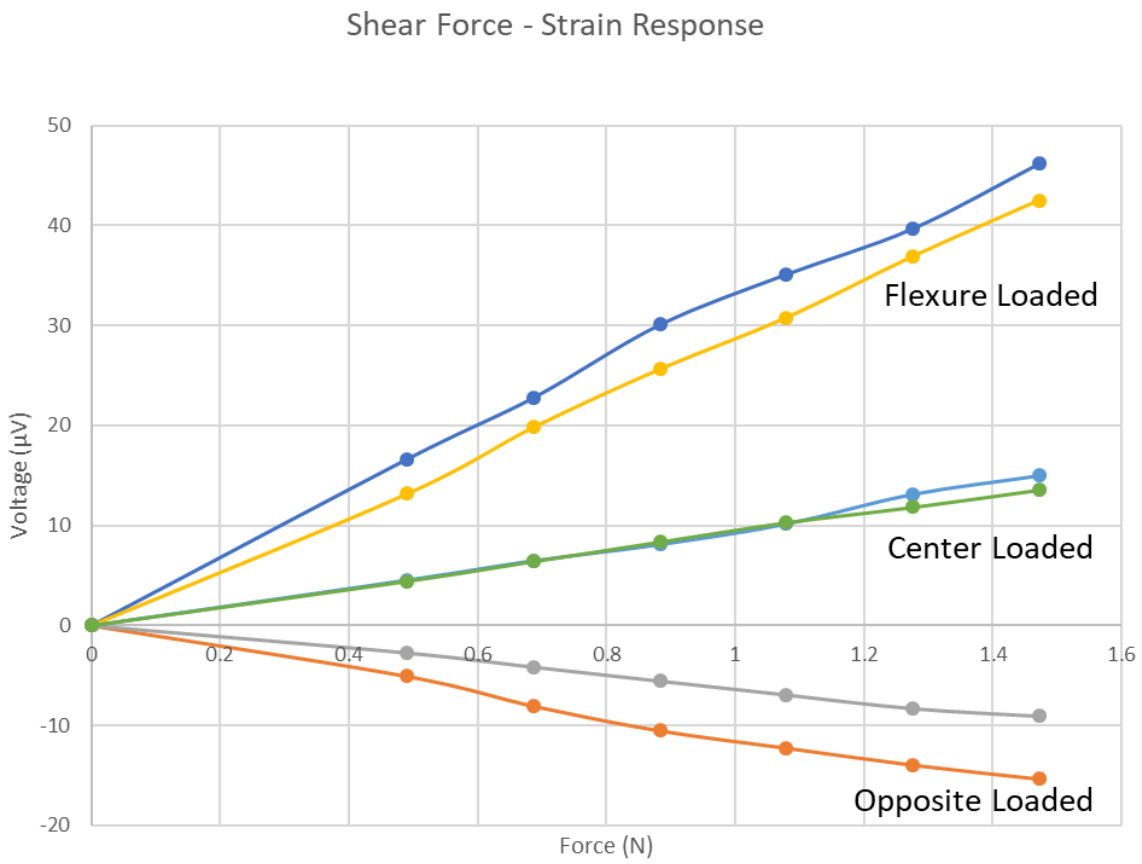

Figure 4.17: Shear force strain gauge response. The lines represent when the load is hung on the blade mount on the flexure, in the center and when the load is on the opposite flexure.

The transfer functions from the shear force calibration are shown in Table 4.4. The combined transfer function remains the same across loading conditions and should be used for first order force measurement, if the exact loading condition is not known.

Table 4.4: Shear force transfer functions.

	Left (µV/N)	**Mid (µV/N)**	**Right (µV/N)**
Transfer Function (Right Flexure)	-10.7	9.3	29.1
Transfer Function (Left Flexure)	31.1	10.2	-6.4
Combined Transfer Function	20.4	19.5	22.7

4.5 Initial Recoating Tests

SLM powder bed literature suggests that experimental powder bed data can be collected through three different methods: (1) the powder bed can be imaged optically [42], [57], allowing a qualitative assessment of the powder layer; (2)hollow cubes can be built on the build platform, allowing entrapped powder to be assessed based on its particle size distribution and packing density [58], [59]; and (3)test specimens can be built, allowing the mechanical properties, microstructure and porosity of the specimens to be assessed [18], [23]. These measurements boil down to being able to take optical images of the powder bed and 3D print user-defined structures.

Recoating tests were conducted in parallel, while the instrumented recoater was being tested and calibrated to establish these capabilities. To conduct these tests, a simplified recoater was built based on the geometric configuration of HAMR. HAMR was also fitted with lights and a DSLR (Canon T3i Rebel) camera to image the recoated build platform (Figure 4.18). The purpose of these tests was to establish 3D printing capability and configure the powder bed optical imaging.

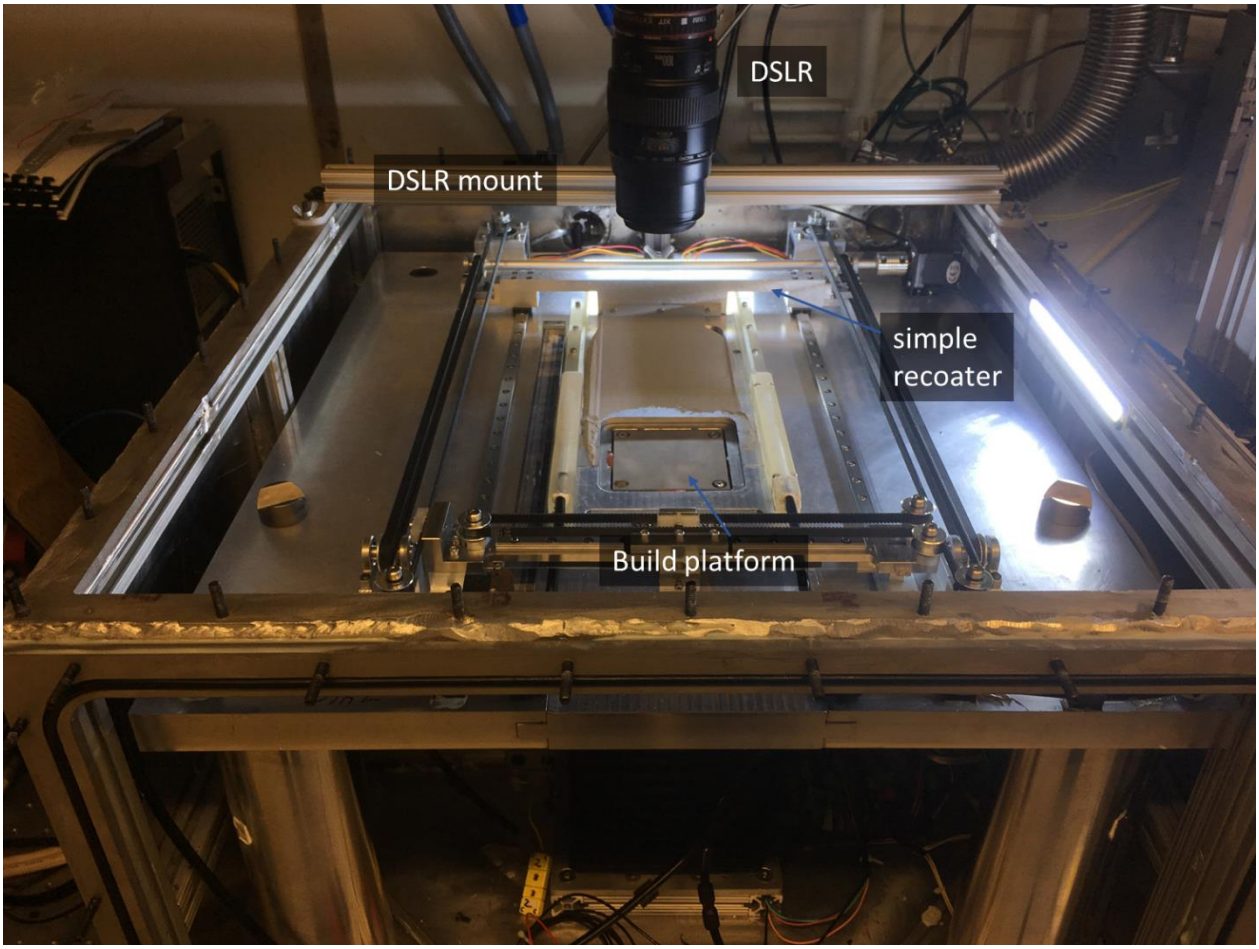

Figure 4.18: Initial recoating test setup

4.5.1 Optical Imaging

Several studies have used optical images of the powder bed to determine the surface roughness of the layer. By lighting the powder layer orthogonally from two sides, topographical information can be inferred from the image based on relative pixel intensities. Brighter pixels represent elevated particles, which cast shadows on surrounding particles at lower heights [42].

A high-resolution image was desired so as to distinguish particles. Resolution is generally a trade-off with field of view. A 20 mm x 13 mm imaging area with 3 μm resolution was achieved by using a 100 mm macro lens and a 50 mm lens extension tube on the DSLR. The resolution enabled individual particles to be distinguished. The pixel intensity from the individual particles was used to determine a qualitative height of the particles. The height could then be used to determine a

surface roughness of the powder bed and compare different the effects of changing recoating parameters.

4.5.2 3D Printing Capability

3D printing in a powder bed system is a necessity for data collection. These data may come from the mechanical properties and density of 3D printed parts or powder trapped in a hollow geometry. Therefore, the 3D printing capabilities of HAMR were demonstrated.

To 3D print parts, HAMR had to be capable of recoating powder layers, creating an inert environment and multi-layer laser control. These features were established through a series of tests. To enable multi-layer prints, a LabVIEW VI was created to automate the SLM workflow. The program configures the recirculation fan, loads the laser pattern, moves the powder and build platform, recoats a layer of powder then fires the laser with the given pattern.

A laser pattern designed for 100 μm layers was created for the 3D test. Between cubes the pattern varied several parameters. The hatch spacing, defined as the distance between lines, was varied between 40-70 μm at 10 μm increments. The laser scan speed was varied between 70-150 mm/s at 10mm/s increments. The laser power output was varied to 50, 64, 79 and 93% of the full power of the 70-Watt laser. The line directions are projected orthogonally from layer to layer to increase layer adhesion. The pattern creates 144 cubes in total (Figure 4.19).

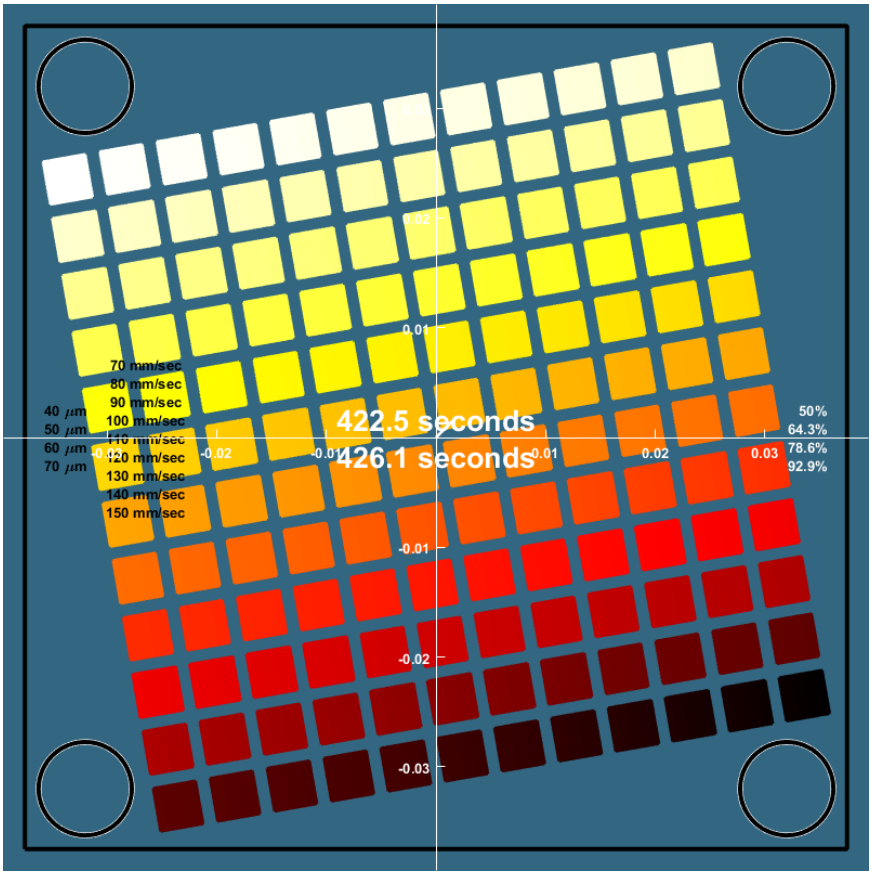

Figure 4.19: HAMR 3D print laser parameters (courtesy of Jonathan Gibbs)

The results from the scans are shown in Figure 4.20. The results were 3D, but at the cost of very thick layers. Eight layers, averaging 500 μm, were recoated then laser melted. The recoater was not able to print thinner layers, due to collisions between the steel recoating blade and the solidified parts. To prevent future collisions, blades were made out of a compliant material, silicone, which would deform rather than stop the recoater. With this change, HAMR will be able to print thinner layers required for robust structures.

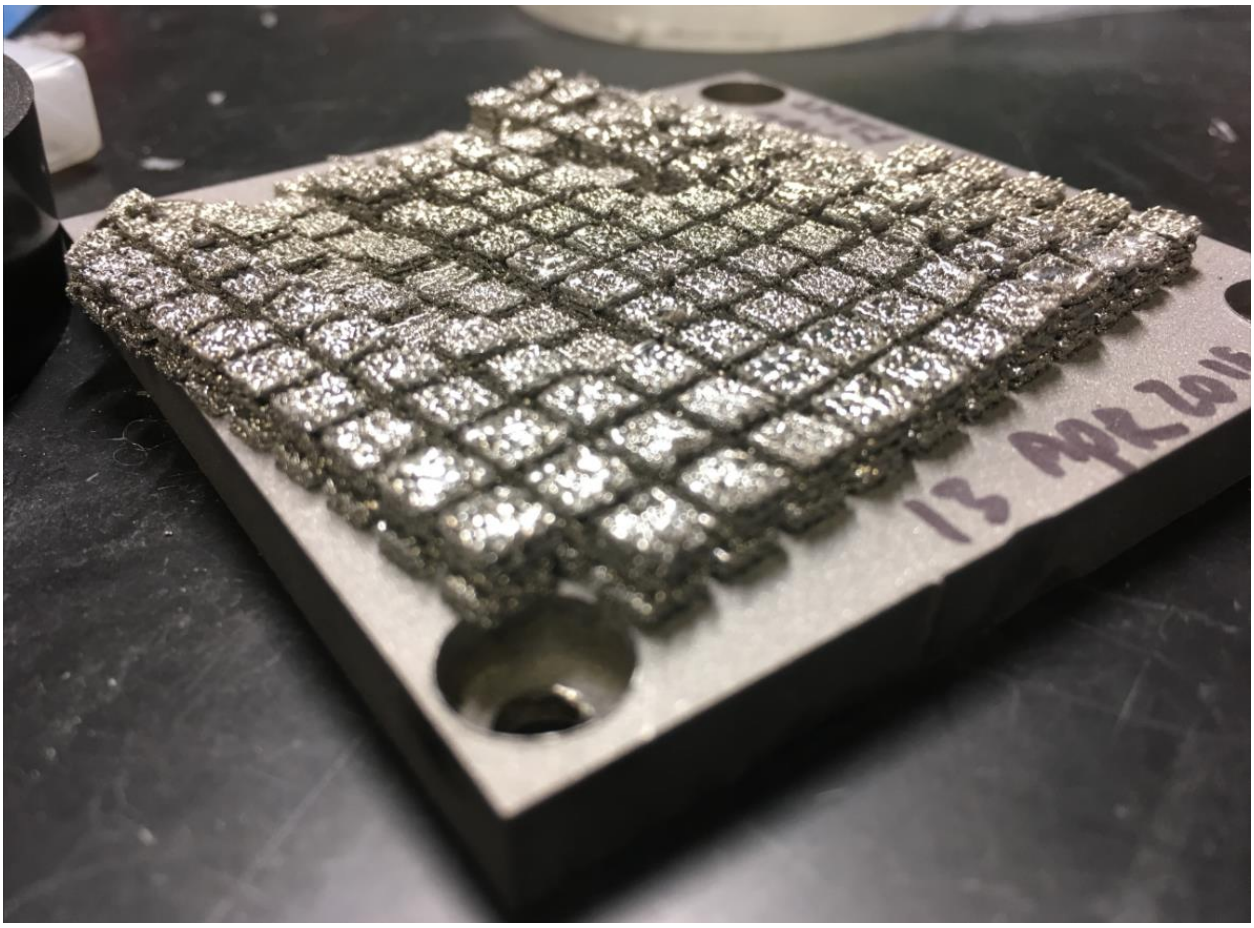

Figure 4.20: 3D print geometries

5 MODELING AND SIMULATION OF POWDER RECOATING

Simulations of powder spreading and packing were used to understand further the process of powder recoating. Powder recoating simulations allow parametric studies to be performed, which vary the blade geometry, blade height, powder size distribution and recoating speed. These studies provide valuable information about the influence of the recoating parameters on powder bed properties. Evaluating each parameter and measuring the powder bed properties would otherwise be time consuming or impossible. The goal of the study is to optimize powder bed properties, including relative density, uniformity of layer thickness, and distribution of particles by size.

Simulations are developed using the discrete element method (DEM) and have been implemented within a research code developed as part of the Bavarian Advanced Computational Initiative (Technical University of Munich). The DEM research code simulates the powder recoating process layer by layer and is novel in that the code incorporates particle cohesive forces, as will be discussed in the rest of this chapter.

5.1 The Discrete Element Method for Powder Bed Fusion

The Discrete Element Method (DEM) computes particle movement and interactions at discrete time steps. DEM models offer a higher fidelity over comparable finite element or finite volume models for granular materials but are more computationally expensive [60]. With advances in computational power, this modeling method has become more attractive, especially in the case of PBF, where the individual powder particles can be modeled.

DEM simulations can be divided into three parts: the initialization, time-stepping and post-processing. The initialization involves spatially orienting all particles and assigning them an initial velocity. The simulation is then advanced through time steps. For macroscopic models a particle encounters forces from friction, gravity and contact plasticity [61]. At each time-step, the forces on each particle is integrated to find its change in velocity and position, which is carried on to the

next time-step. After the simulation has advanced through the preallotted time-steps, the results can be post-processed. The results show the particle position and velocity at each time-step and can be used to analyze the bulk powder properties, such as mixing or flow.

Powder bed fusion DEM simulations attempt to mimic the PBF process. The simulations are initialized by filling the powder supply platform with powder particles. At each time step, the recoater blade is advanced from the powder supply platform across the build platform. After recoating, the platforms can be moved and the recoater advanced again to simulate multiple layers. At the end of the simulation, the powder bed can be analyzed by looking at the position and diameter of the particles in the powder bed, which are used to measure the packing density and powder bed uniformity.

Most powder recoating DEM papers have modified the open-source research code from the Large-scale Atomic/Molecular Massively Parallel Simulator (LAMMPS) to fit PBF [40], [41]. In this thesis, another research code, from the Bavarian Advanced Computational Initiative (BACI) [62], will be employed in collaboration with the Technical University of Munich. The BACI code enables a greater flexibility over the DEM model to implement cohesive forces, which will be discussed in the following sections.

5.2 Cohesive Forces of AM Metal Powders

Cohesion is the tendency of particles to stick together due to interparticle attractive forces. At the macroscopic scale, contact and friction forces dominate the particle interactions. With sufficiently small particles, cohesive forces are on the same order of magnitude as gravitational and inertial forces. As a rule of thumb, cohesive forces should be considered with particles below 100 μm in diameter [63]. The dominance of these forces requires they be added to the model of AM powders. For AM particles, these forces are largely due to capillary effects, Van der Waals (vdW) interactions and electrostatic forces. These forces will be discussed in this section.

5.2.1 Capillary Forces

The capillary effect occurs when granular media are partially saturated. With partially saturated materials, both liquids and gases fill the voids between particles. Saturation occurs with most granular materials in a natural environment due to the humidity in the air and can only be

completely avoided within a vacuum [64]. The humidity causes a film to envelop the individual particles. When two particles are sufficiently close, a liquid bridge forms across the two particles. The surface tension of the liquid creates an attractive force between the two particles [65]. A simplified model approximates the force, F, between two spheres as:

$$F = \pi d\gamma \cos\theta \tag{5.1}$$

where γ is the surface tension of the liquid, d is the sphere diameter, and θ is the liquid-solid contact angle.

5.2.2 Electrostatic Forces

Electrostatic forces include Coulomb force, image force, and electrostatic potential difference. These forces are caused by differences in charge potential between particles and can be summarized by:

$$F_{ec} = \frac{1}{4\pi\varepsilon_0}\frac{q_1 q_2}{r^2} \tag{5.2}$$

where q_1 and q_2 are the point charges of the particles, r is the distance between particles, and ε_0 is the permittivity of the medium [66].

5.2.3 Van der Waals Forces

Van der Waals (vdW) forces can arise from induced particle dipoles. The vdW forces can vary based induced dipoles. The vdW force is based on a difference of potential given by:

$$w(r) = -\frac{C}{r^6} \tag{5.3}$$

where *C* is an interaction parameter and *r* is the distance between the particles.

H. C. Hamaker sought to characterize this interaction potential for London dispersion forces, which is a common form of vdW force. He integrated the potential to provide an analytical form for the force between two particles. This approximation includes the Hamaker constant, *A*, which is approximated based on the atomic properties of the material. The analytical formula of the London dispersion forces is:

$$F_{vdW} = \frac{A}{6s^2} R^* \tag{5.4}$$

Where, $R^* = \frac{R_1 R_2}{R_1 + R_2}$ is the reduced radius and s is the distance between particles.

While the Hamaker constant holds true for gases, it is where other neighboring particles are present. This is due to the nature of the Hamaker derivation, which uses pairwise additivity to approximate the force. The Lifshitz theory avoids this problem through a different derivation of the Hamaker constant, using bulk properties such as the dielectric constant [67].

5.2.4 DMT vs. JKR

Several models have sought to approximate the cohesion of particles after contact has been made. These models, based on the surface energies of the particles, approximate the amount of force required to separate two particles in elastic contact. These models are important when considering agglomeration.

The DMT model assumes a Hertzian contact between two particles. Heim [64] has stated that the DMT model is more accurate for smaller rigid particles. The pull-off force is calculated by:

$$F_{DMT} = -4\pi\gamma R^* \tag{5.5}$$

where γ is the surface energy of the particle.

The JKR model is more applicable to large soft spheres such as rubbers, by accounting for cohesive forces which may increase the contact area between the two spheres [66]. The formula becomes:

$$F_{JKR} = -3\pi\gamma R^* \tag{5.6}$$

Since AM largely deals with small, rigid metal powder particles, the DMT theory will be used. It is important to note, however, that several other studies, such as Parteli et al. [17], have used the JKR theory in their simulations.

5.3 Simulation Model

The physical modeling of the powder particles combines the effects discussed in the theory section with other relevant powder parameters. This section will briefly summarize how powder parameters and effects were modeled, as a detailed description of the powder modeling can be

found in Weißbach [68]. The sizes of the powders were fitted to the lognormal size distribution provided by the powder supplier, shown in Section 5.4.1. Based on SEM images of the powders (section 5.4.2) being modeled, they are assumed spherical. The elastic deformation of the particle collisions is modeled as Hertzian contact and is implemented through a penalty contact model. Energy dissipation through dynamic collisions is accounted for with non-linear damping. The friction and rolling resistance uses a Coulomb friction contact with damping. The Van der Waals force is a linearized form of the equation 5.4. The linearization is necessary for computational stability and efficiency. The electron exchange interactions can be calculated using equation 5.5 by extrapolating the surface energy from the pull-off force. Plastic deformation is checked using a von-Mises yield criterion at each collision to ensure the material's yield strength is not exceeded.

Capillary and electrostatic forces, mentioned in Section 5.2.1, have been neglected from the model. The capillary forces are considered insignificant, since the powders are assumed dry. Powder spreading occurs in an environmental controlled SLM chamber, where the powder is dried beforehand or a vacuum environment, which also dries the powders [69]. Electrostatic forces can be neglected, since metal particles are modeled. Metal particles are conductive, which results in the same charge potential across the particles. The modeling of these powders is summarized in Table 5.1.

Table 5.1: Simulation modeling effects considered and neglected (recreated from [68]**)**

Considered Effects	
Physical Parameter/ Effect	**Implementation**
Size and size distribution	Fitted lognormal size distribution
Shape	Spherical discrete elements
Elastic deformation	Penalty contact model with linear spring, non-linear damper model
Energy dissipation during collisions	Non-linear viscous damping to model coefficient of restitution
Friction and rolling resistance	Coulomb friction with damping
Van der Waals force	Linearized regularized adhesive force
Electron exchange interactions	DMT contact model with pull-off force-based surface energies
Gravity	Gravitational force on all particles
Plastic deformation	Hertzian contact with von-Mises yield criterion to check that yield strength is not exceeded
Neglected Effects	
Effect	**Reasoning**
Electrostatic forces	Electro-conductive materials
Capillary forces	Dry environmental conditions

5.4 Characterization of Powder Particles

To maximize the accuracy of the recoating simulations, data were collected to calibrate and validate the considered effects in Table 5.1. The morphology, size distribution, surface roughness and pull-off force were measured with a scanning electron microscope (SEM), laser diffraction particle size analyzer, optical profilometer and atomic force microscope (AFM), respectively. Analyzing the morphology validated the assumption that the particles were spherical. A representative simulation size distribution was created based on the distribution measurement. The surface roughness and pull-off force were used to validate first-order calibrations of the surface energy and will be used in future simulations for more precise calibration.

5.4.1 Size Distribution

Three size distributions were purchased from AP&C powders for characterization and AOR experiments (Section 5.5). Titanium 6Al-4V powders were produced by plasma atomization then sieved to produce size distributions with banded limits of 0-25, 15-45 and 45-106 μm. These size distributions are often referred to as fine (0-25 μm), medium or standard (15-45 μm) and course (45-106 μm). The supplier provided size distribution data using a laser diffraction particle size analyser for each of the powder lots. These data were replotted to produce Figure 5.1.

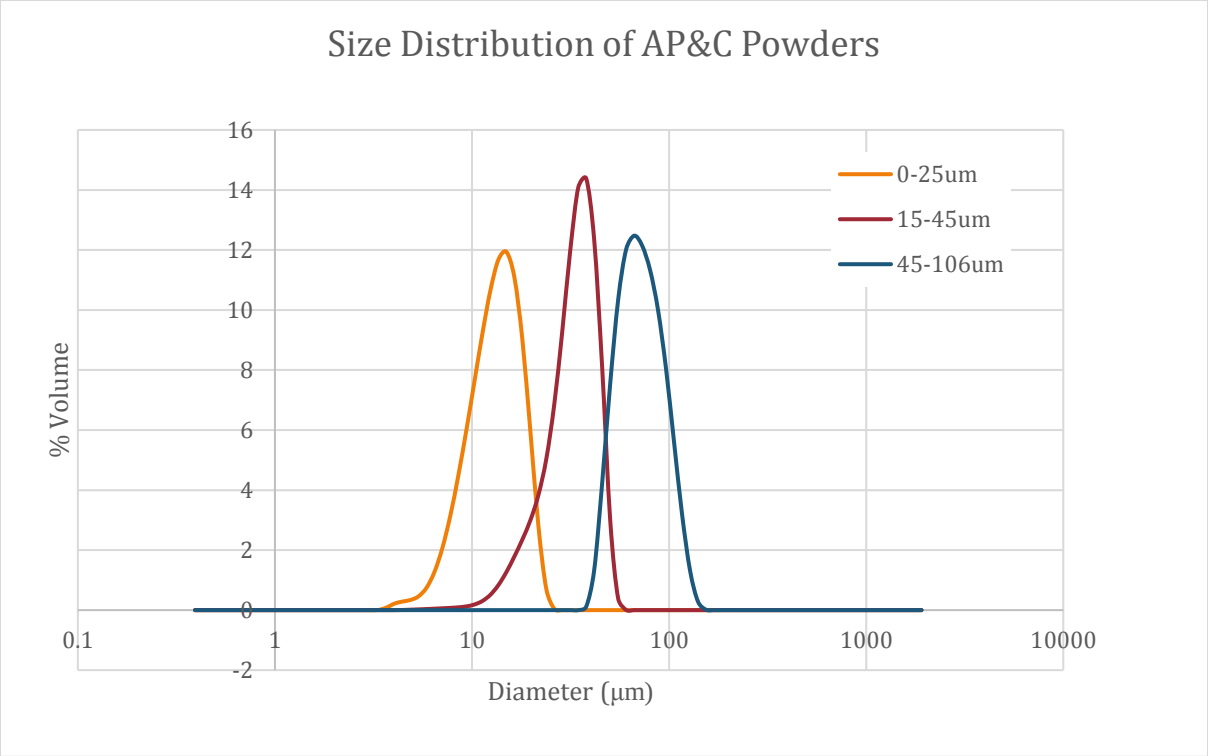

Figure 5.1: Size distribution by %volume [70]

Figure 5.1 shows that each of the powders follow a lognormal standard distribution by % volume. The distributions have the same shape but are shifted by the mean diameter of the powder particles. With these distributions, the mean particle diameter provides a good indicator of the powder distribution. The mean particle diameters for the three distributions were 14 μm for the fine powder, 34 μm for the medium-sized powder, and 72 μm for the course powder.

5.4.2 Morphology

Plasma-atomized powders contain the high sphericity particles in comparison with powders produced by other techniques. The sphericity of the powders was confirmed with SEM images. Exemplary images from the SEM are shown in Figure 5.2. The images show highly spherical particles across a wide range of sizes and show particles with low surface roughness.

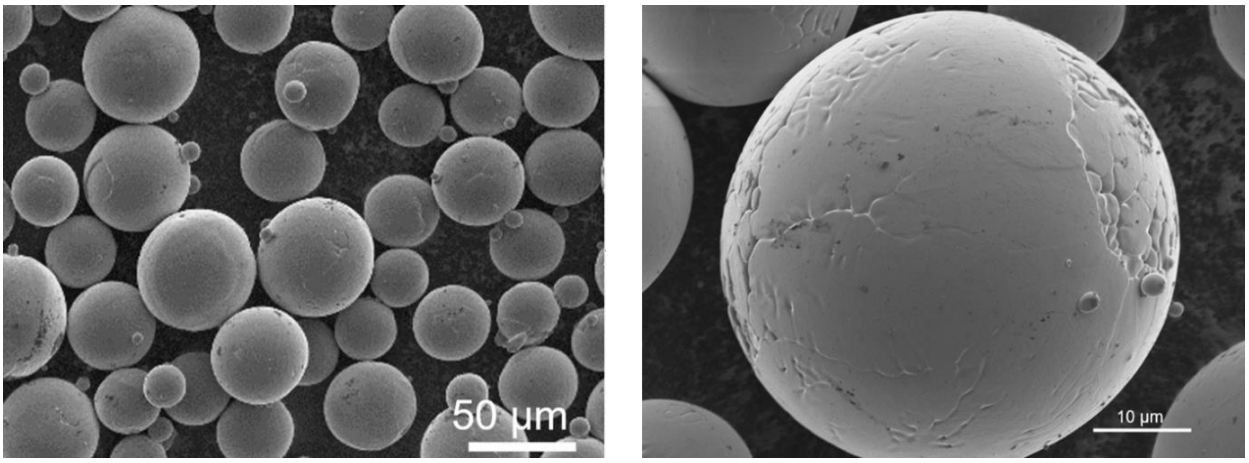

Figure 5.2: SEM images of the course powder morphology (courtesy of Yu Zuo) [71]

5.4.3 Surface Roughness

The surface roughness is generally measured as the root-mean-square (the square root of the mean square) of the surface of a particle. These measurements are commonly made with an atomic force microscope (AFM), using a contact mode tip, and are generally on the order of several to tens of nanometers for smooth particles [72]. As far as the author is aware, no literature exists measuring the surface roughness of AM metal particles. Heim [64] created gold particles using a technique similar to gas atomization and measured a surface roughness between 6-15 nm.

First order surface roughness measurements were made using an optical profilometer. A Zygo NewView 5000 profilometer was used to generate point clouds of Ti-6Al-4V metal particles, which were then fit to a sphere, allowing particle surface roughness to be calculated. The surface roughness for three particles was measured to be in between 92-122 nm (Table 5.2).

Table 5.2: Ti-6Al-4V surface roughness calculated with optical profilometer

Particle Diameter (µm)	**Particle Surface Roughness (nm)**
61	122
40	94
53	92

5.4.4 Pull-Off Force

Pull off force can be used to calculate the surface energy of the powder particles and thus calculate the cohesive force between particles. Walton [66] described a large discrepancy between the theoretical and measured pull off force, likely due to the surface roughness of the particles. The pharmaceutical industry has published several papers in which these experiments are conducted, but few studies of metal powders have been conducted. Heim [64] measured the mean normalized gold-gold adhesion force (F_{ad}/R) as 0.038 N/m, but these values vary within a wide range for particles of the same size.

Collaboration with Professor Robert Carpick and Dr. Harman Khare (UPenn) was established for measuring the cohesive forces of AM particles. Particles were segregated into three different size regimes: small (approximately 15 μm), medium (approximately 30 μm), and large (approximately 50 μm). Particles within each size category were glued onto a glass slide. AFM cantilevers were functionalized with large and small particles. The glass slides and AFM tips were used to measure particle-particle pull-off force in ambient conditions.

Approximately 100 pull-off force values were recorded and plotted against the effective radius of the particles, as shown in Figure 5.3. The data is not yet calibrated to the actual cantilever stiffness, but calibration will only scale these values by a fraction of their current value and values are within the same range as Heim's values for gold particles. The pull-off force scales linearly with the size of the particle, as predicted by the DMT model and reported by experimentalists in the literature. The data also show a large scatter for similarly sized particles, which is likely caused by varied particle surface roughness and varied AFM preload. Future work is planned to control the data for these factors.

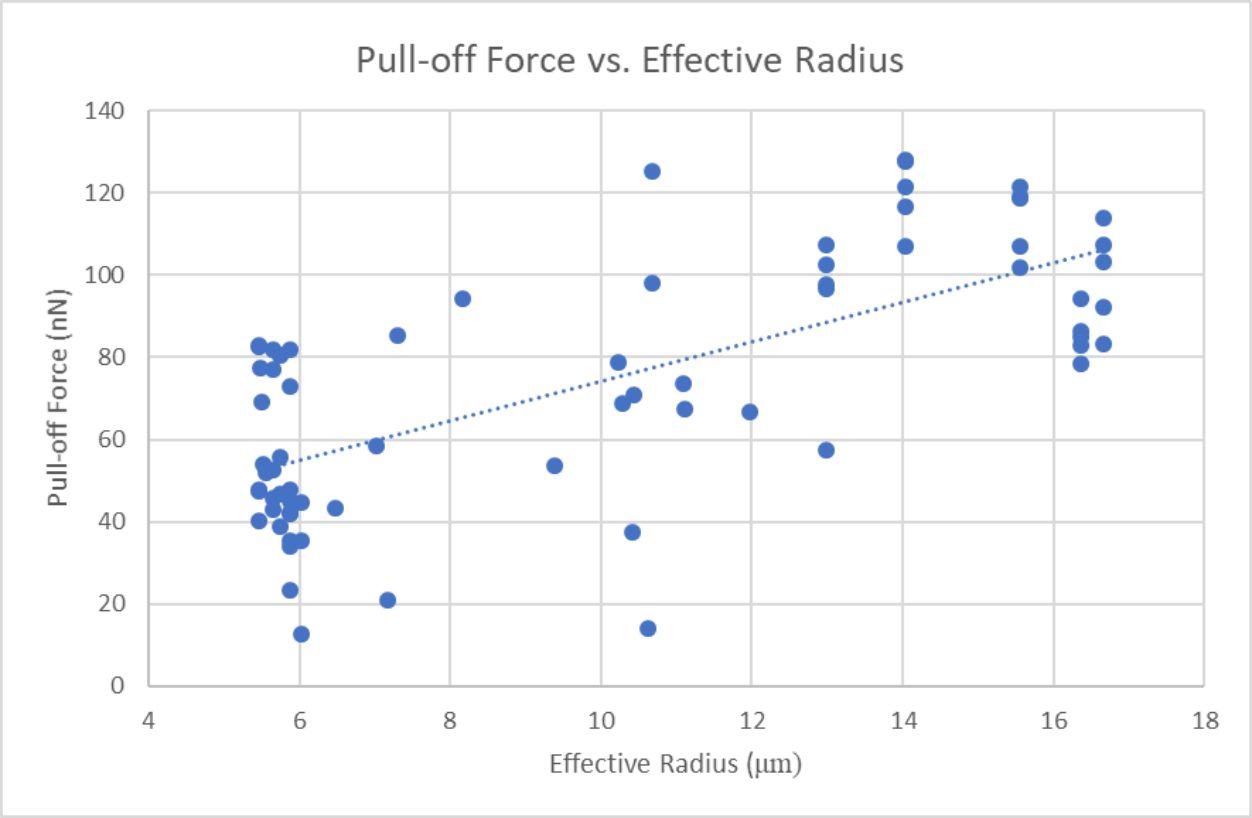

Figure 5.3: Interparticle pull-off forces for varied particle sizes

The surface energy was calculated based on the pull-off force and effective radius using the DMT model (Equation 5.5). The surface energy between particles should be consistent across particles, as the value is based on material properties. A histogram of the surface energy values is shown in Figure 5.4. Future simulations will incorporate these surface energies and their stochastic variation.

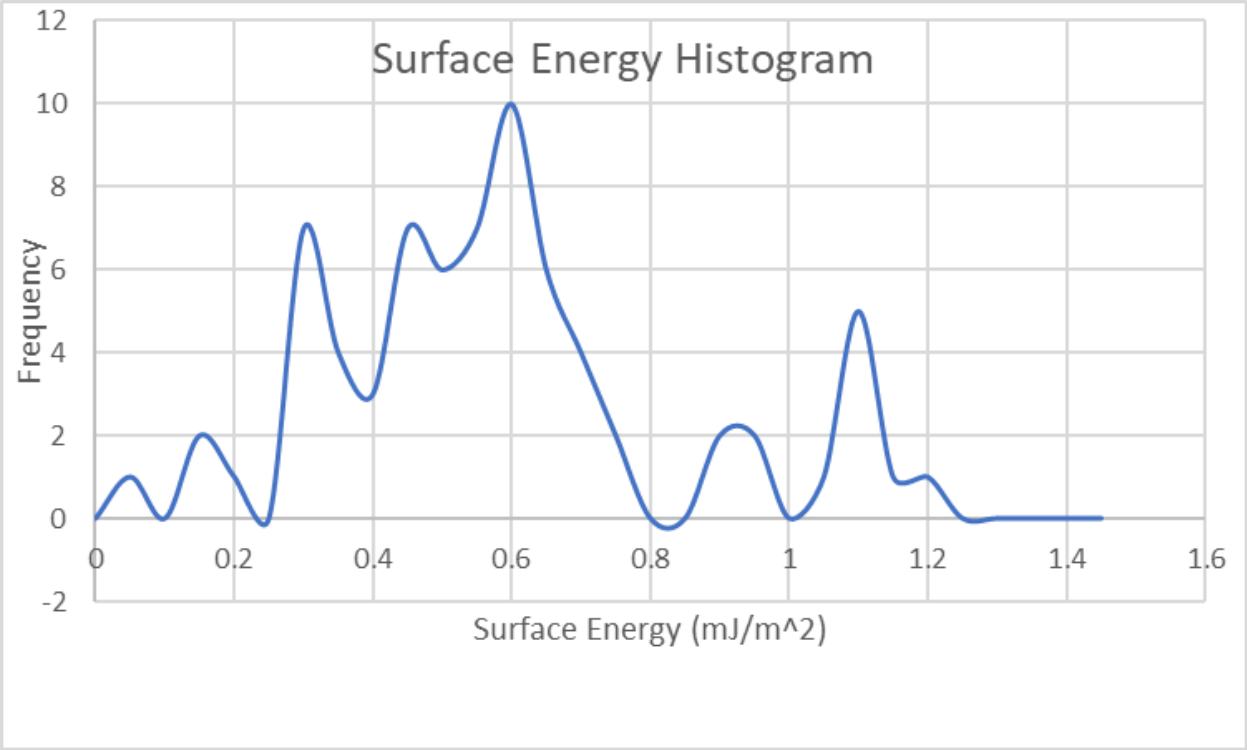

Figure 5.4: Surface energy of titanium particles

5.5 AOR Simulation Calibration

Measuring the powder properties on the particle scale is both time consuming and expensive, therefore other methods were employed in parallel to estimate first-order simulation parameters. A common technique is to create a simulation model to match an experimental setup then compare the simulation results with experimental results and adjust the input parameters such that the results agree. Simulation results were fitted to results from angle of repose (AOR) tests to find the appropriate surface energies for three size distribution of powder. This thesis will cover the AOR Calibration process superficially, as the process was covered in depth in the publication by Meier *et al* [73].

The angle of repose measures the steepest angle at which powder settles onto a horizontal plane. Several computational papers have used the AOR to calibrate their code [74]. Literature has verified that the AOR provides a good indication of the powder properties [75].

5.5.1 Experimental Setup

An experimental setup was designed to accurately measure the angle of repose for three different Ti-6Al-4V powder size distributions: 0-25 μm, 15-45 μm, and 45-106 μm, discussed in Section 5.4.1. The setup consisted of a funnel of 60° pitch and a 1 mm opening diameter placed a fixed distance above a 10x10 mm platform. The funnel was encased in a holder, which allowed a glass slide to be moved underneath the funnel outlet to allow for controlled powder flow. An adjustable stand allowed adjustment of the distance between the funnel and powder platform. An excess powder bin ensured overflow powder was contained. A USB microscope camera captured both dynamic video of the powder flow and static images of the powder settling on the platform. Figure 5.5 illustrates the experimental setup.

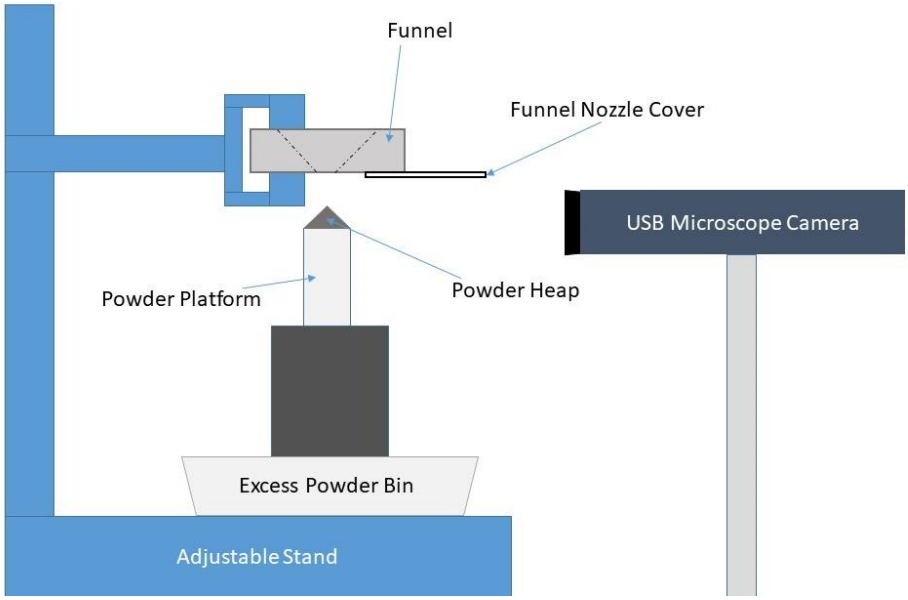

Figure 5.5: AOR experimental setup

The AOR setup was assembled in a fume hood for safety concerns. The USB microscope was aligned on one side of the powder platform and focused. The funnel was adjusted to a minimal distance above the peak of the powder heap to minimize the dynamic energy of the powder flow. This minimum distance was found by initially creating a powder heap, then adjusting the height of the funnel. The powder platform was aligned underneath the funnel using a light shined through the funnel opening, creating a focused beam that was visually adjusted to the center of the platform.

The funnel nozzle cover was slid underneath the funnel to block the outlet. Then powder was poured to fill the funnel halfway, approximately 15 mm from the funnel outlet. After the USB camera began filming, the funnel nozzle cover was removed. Due to the small nozzle diameter, the two finer powder size distributions required agitation to start powder flow. The amount of agitation required increased as the powder particle size decreased.

5.5.2 AOR Measurement

The angle of repose of the powder was measured using the image processing software, ImageJ. The angle was measured as the angle from the powder platform to the steepest slope on the powder heap. The measurement was made on both sides of the heap and averaged. Figure 5.6 shows exemplary static images taken from AOR experiments for the three different size distributions. A notable increase in AOR was observed for the powders with decreasing size distribution. An AOR of 34, 41 and 66 degrees was measured for Figure 5.6 a, b and c, respectively.

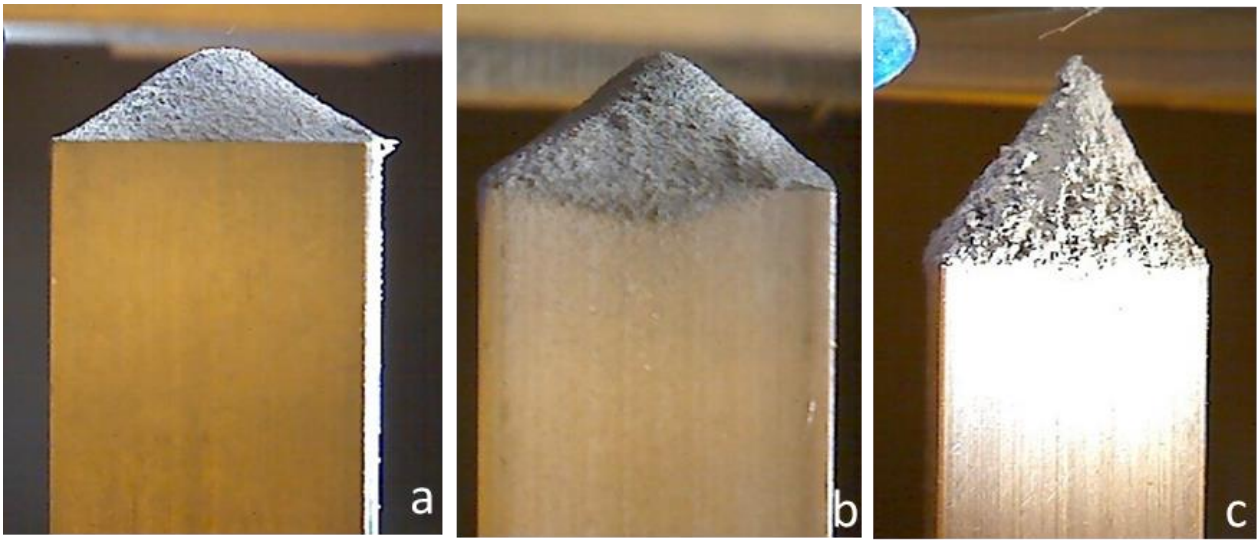

Figure 5.6: Angle of Repose of three different powder size distributions. (a) 45-106 µm, 34° (b) 15-45 µm, 41° (c) 0-25 µm, 66°

The AOR experiment was conducted sixteen times for each powder size distribution to determine the variability of the AOR. For the 0-25, 15-45 and 45-106 µm powders, means of 63, 43 and 33° and standard deviations of 1.7, 2.2 and 1.6, respectively, were found. These results are plotted in

a box-and-whisker chart in Figure 5.7, where the legend shows the mean diameter of the three powder size distributions.

The standard deviations show that the AOR only varies within a few degrees, meaning the results are viable for simulation calibration. The results are proven reliable given that the measurements are in good agreement with other experimentalists' values. Sun [42] measured an AOR of 32°for a Ti-6Al-4V, 45-106 μm powder, which is within one degree of AOR measured for the AP&C course powder.

Figure 5.7: AOR - 10 mm side length platform

A smaller platform was desired to increase the computational efficiency of the model. Literature cites that the AOR of a given powder is dependent on the powder's geometric boundary conditions [76]. Therefore, one would expect the AOR to vary with varying platform size. For this reason, the measurement was repeated three times on a 5 mm and 2.5 mm side length platform to measure the sensitivity to the platform size.

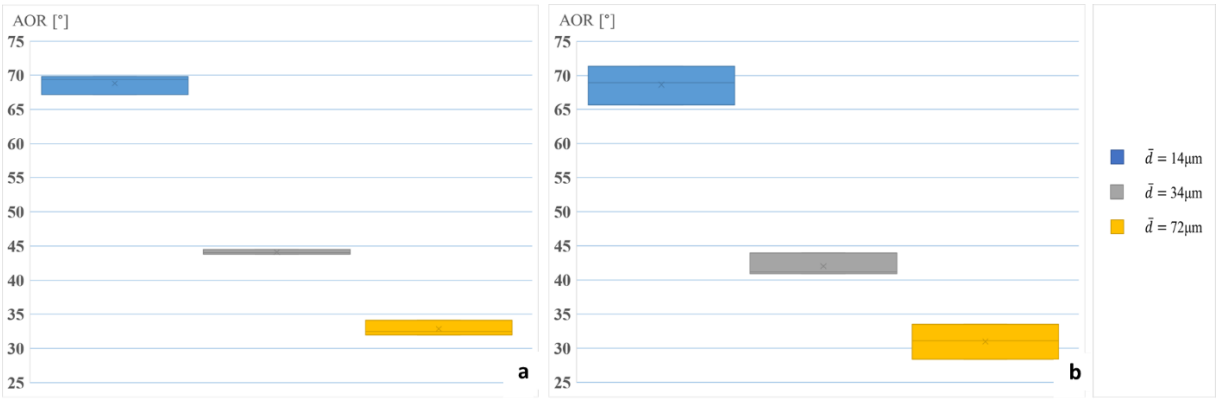

Figure 5.8: AOR measurements on square platforms with side lengths (a) 5 mm (b) 2.5 mm

Figure 5.8 shows the AOR for square platforms with a side length of 5 mm and 2.5 mm. The figure shows that the AOR is not drastically sensitive to the three platform geometries. The mean AOR between all of the powders, except the finest powder, remains within 1-2° between the different configurations. The largest difference can be seen with the smallest size distribution of powder, where there is a noticeable increase in the AOR from a mean of 63° to 68° with the smaller platforms. A larger variability can be seen as well with the finest powder. The increase in mean and variability can be explained by the increased influence of cohesive forces due to the smaller particles. Since these results were proven reliable with a small variance, the mean AOR from these experiments was used to calibrate the model, as discussed in the next section.

5.5.3 Parameter Fitting with AOR Simulation

A simulation model was created to match the funnel and platform in the AOR experimental setup. The simulation was initialized with the funnel full of power and the outlet in contact with the powder platform. With each time-step, the funnel was raised to minimize the distance that the powder falls thus minimizing the dynamics of the process, and at each time-step powder came out of the funnel. The simulation was complete once the powder was in a steady state condition. Post processing involved fitting a triangle to a still image of the powder heap.

The AOR simulation was run for multiple surface energy values from zero to 0.4 mJ/mm^2. By matching the experimental and simulation AOR, a surface energy value was found to represent the cohesiveness of a given powder. Figure 5.9 shows exemplary images from the AOR simulations

and their comparison to the AOR experiments. As the figure shows, there is good agreement between the simulations and experiments.

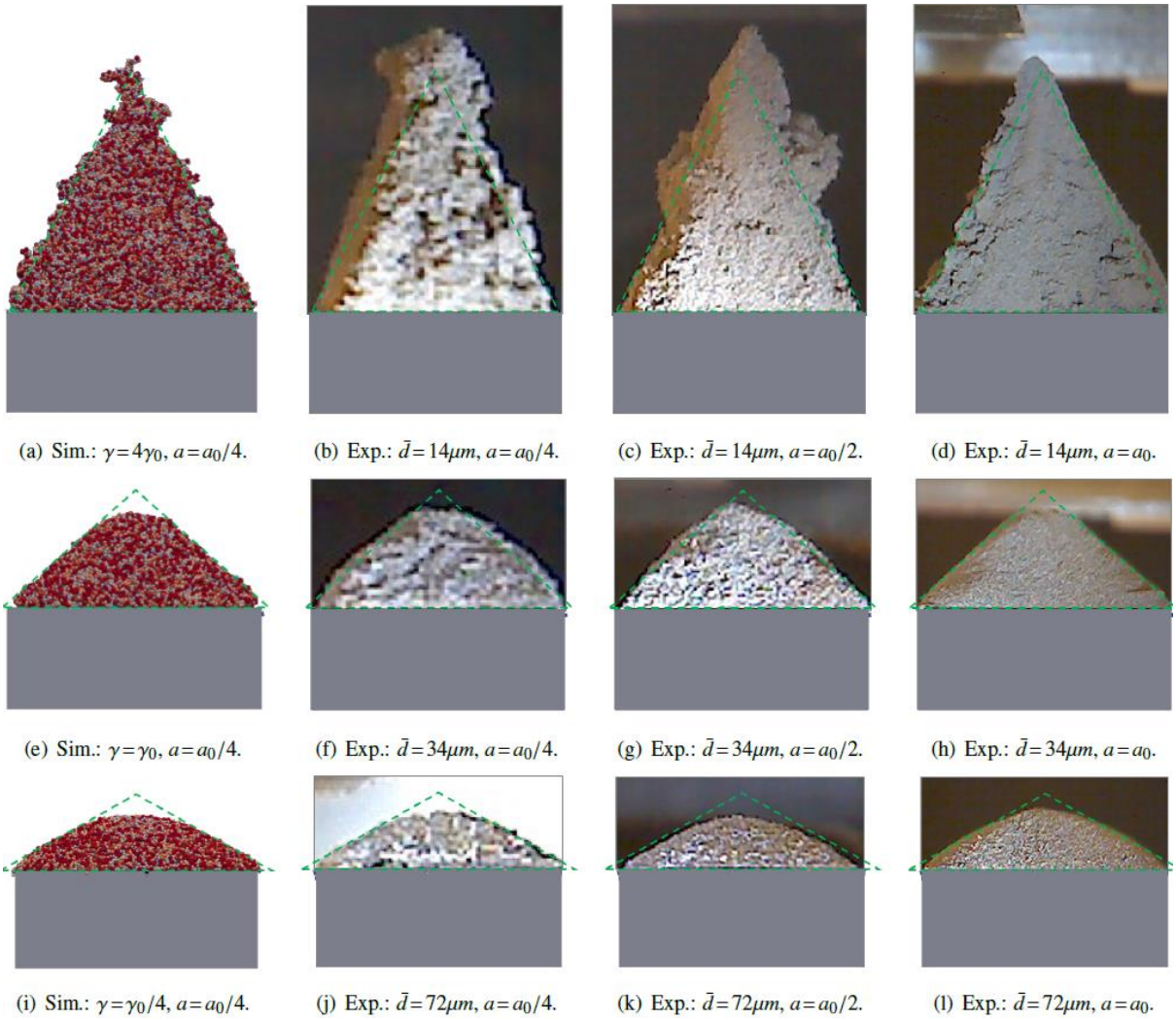

Figure 5.9: Numerical vs. experimental funnel results [73]

A surface energy of $\gamma = \gamma_0 = 0.1$ mJ/mm^2 was used to represent the medium size powder. A surface energy of $\gamma = 4\gamma_0$ was used to represent the fine powder, and a surface energy of $\gamma = 0.25\gamma_0$ was used to represent the course powder. These values show that there is a direct correlation between the simulation surface energy and particle size distribution and the simulations can replicate the behavior of the powder size distribution by fine tuning the surface energy. The relationship between the surface energies and mean particle sizes are summarized in Table 5.3. A ratio of the adhesion force to gravity force for each of the powders is also given in the table. The ratio demonstrates the increasing influence of adhesion over gravity as particles become smaller.

Table 5.3: Surface energies based on the equivalent mean particle diameter and the ratio of the force-to-gravity ratio (Reproduced from [73]**).**

$\bar{\boldsymbol{d}} = \boldsymbol{d_0}, \quad \boldsymbol{\gamma}/\boldsymbol{\gamma_0}$:	**0**	**0.25**	**1**	**4**
$\gamma = \gamma_0, \quad \bar{d}/d_0$:	∞	2	1	0.5
F_γ/F_G:	0	3.25	13	52

5.6 Recoating Simulation Exemplary Results

The AOR surface energy values were used to calibrate the AM recoating simulations for the powder size distributions. The recoating simulations were used to analyze the effect of the main recoating parameters of layer thickness and recoating velocity, while varying the surface energy of the powder. The effect of changing these variables was measured with the packing fraction and surface uniformity of the powder layers. This thesis covers only the exemplary results from the recoating simulations, as the process was covered in depth in the publication by Meier *et al* [24].

The simulation has the same architecture described in Section 5.1 and shown in Figure 5.10. Powder is distributed in a powder platform then spread over a build platform in discrete numerical time-steps. After a layer is spread, the simulation results were post-processed to find the packing fraction, ϕ, and layer uniformity, z. The packing fraction was measured by discretizing the powder bed into volumes, measuring the total volume of powder in the discrete volume, then dividing the powder volume by the total volume. The surface uniformity was found by measuring the variation in powder bed height.

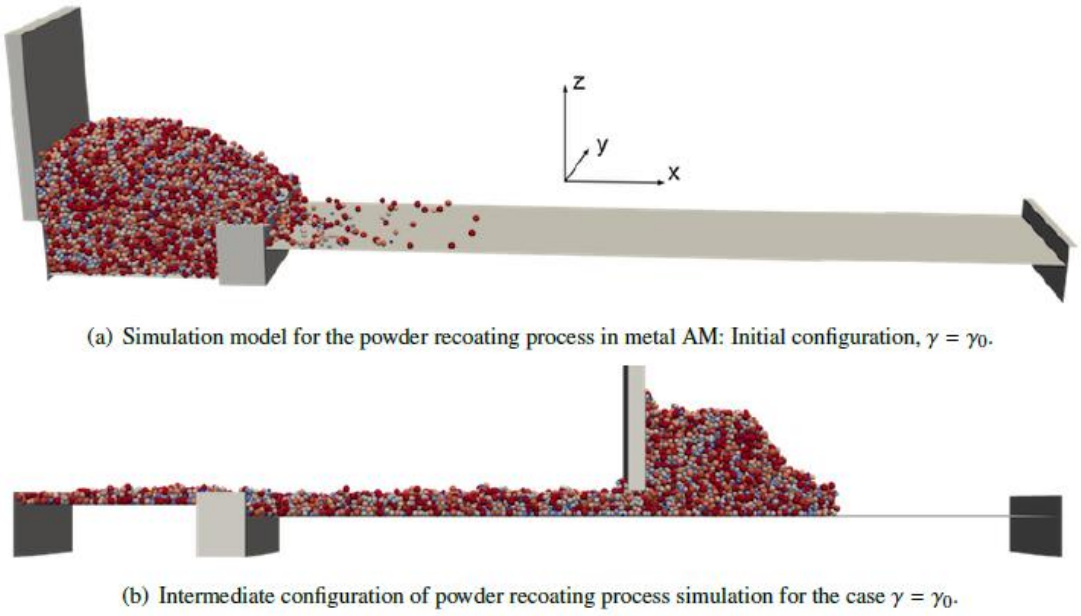

(a) Simulation model for the powder recoating process in metal AM: Initial configuration, $\gamma = \gamma_0$.

(b) Intermediate configuration of powder recoating process simulation for the case $\gamma = \gamma_0$.

Figure 5.10: BACI recoating simulation architecture [24]

Changing the layer thickness proved to have a significant effect on the packing fraction and layer uniformity. The layer thicknesses, t_0, were based on the maximum particle diameter, d_{max}, in the powder size distribution. Simulations were repeated for t_0 equal to one, two, three and four times d_{max} using the four powder cohesion values given in Table 5.3. As a general trend, the packing fraction and surface uniformity decrease with thinner layers and more cohesive powders. Between the d_{max} and $2d_{max}$ layers, there is a large jump in the packing fraction and surface uniformity. Further thickening of the layers beyond $2d_{max}$ has a diminishing return. Increasing cohesion on the other hand, leads to a gradual decline in the uniformity and packing fraction. The overall effect of cohesion is large. The difference between the least and most cohesive powder accounts for a 10-20% change in the powder bed properties. Figure 5.11 summarizes the simulation results.

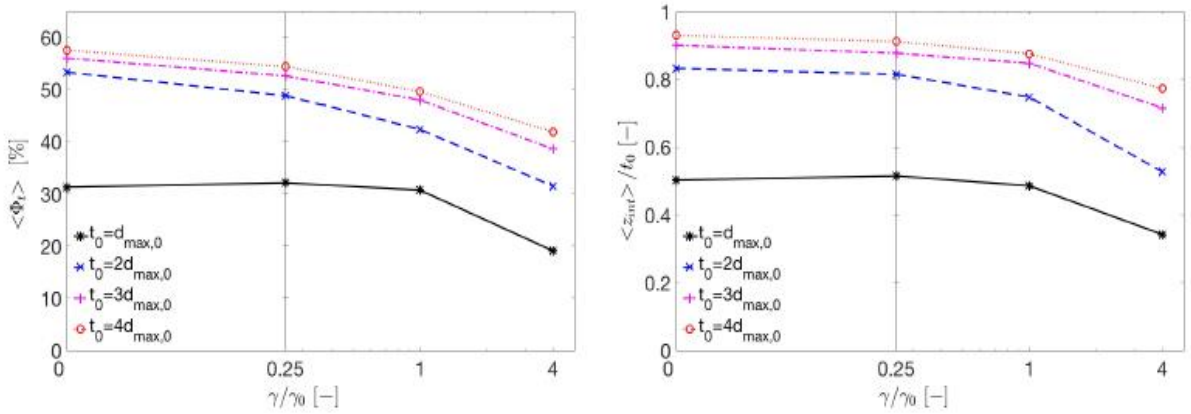

(a) Mean value of packing fraction field $\Phi_t(x, y)$. (b) Mean value of surface profile field $z_{int}(x, y)$.

Figure 5.11: Influence of layer thickness on the (a) packing fraction and (b) surface roughness for varied powder cohesion [24]

The recoating velocity also had a significant effect on the powder layer. The blade velocity, V_B, was based on multiples of V_0 = 10 mm/s. Simulations were run for V_B equal to 1, 2.5, 5 and 10 times V_0 to scale the capabilities of commercial additive manufacturing machines. As expected, an increasing blade velocity has a deteriorating effect on the packing fraction and surface uniformity of the powder bed. While increased cohesion also deteriorates the powder bed properties, the cohesion actually improves the surface uniformity at the V_B=10V_0. This means that the velocity of the blade could be tailored to the powder being used, to provide the optimum productivity and powder bed properties. These results are summarized in Figure 5.12.

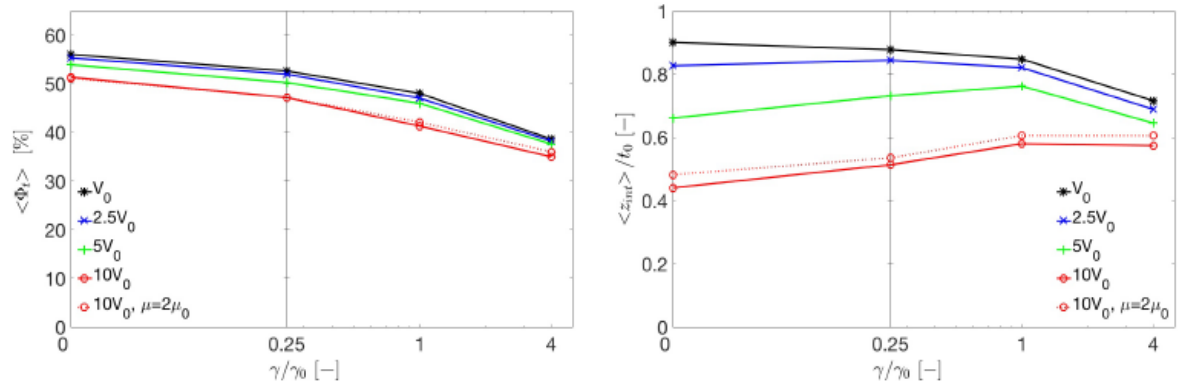

(a) Mean value of packing fraction field $\Phi_t(x, y)$. (b) Mean value of surface profile field $z_{int}(x, y)$.

Figure 5.12: Influence of blade velocity on the (a) packing fraction and (b) surface roughness for varied powder cohesion [24]

These results effectively demonstrate the importance of including cohesion, in relation to the main independent and dependent variables in powder recoating. These simulations provide a good framework for future work. Future simulations will be improved with better calibration using AFM measurements. Furthermore, future simulations will cover more methods to optimize the process using the recoater blade geometry and movement.

This page intentionally left blank

6 CONCLUSION AND FUTURE WORK

The main goal of this thesis was to explore a framework for studying powder recoating in powder bed fusion. In this thesis, a computational and experimental framework were established. First, a custom, instrumented powder recoater was designed for an SLM system (HAMR) with the capability to measure forces, control the blade height, control the recoating velocity and use custom blade geometries. Second, the instrumented recoater and the HAMR system were tested. Third, a DEM model, which included interparticle cohesive forces, was calibrated to three different powder size distributions. The main insights and contributions from this thesis, as well as possible research avenues using the experimental and computation testbeds, are discussed below.

6.1 Insights and Contributions

The main insights and contributions of this thesis are:

- An instrumented powder recoater was built with the capability to measure forces, control blade height, control recoating velocity and use custom blade geometries.
- A low-profile blade positioning system was developed using piezoelectric stack actuators and a lever-type flexure hinge system. The blade positioning system enables a maximum displacement of 69 μm.
- Depending on the actuation mode, the blade positioning system can also be used to apply a force or vibration to the powder bed to compact the powder bed.
- The recoater was instrumented with four strain rosettes to provide force sensing in the shear and normal directions of the recoater. With adequate signal condition, the system forces can detect forces in the millinewton range.
- High resolution powder bed imaging was demonstrated using a DSLR camera.
- The 3D printing capability of a research SLM system (HAMR) was demonstrated.

- A DEM model was calibrated with three size distributions of Ti-6Al-4V powder using angle of repose experiments. A surface energy of 0.1 mJ/mm^2 was found.
- The calibrated surface energy was within an order of magnitude of values found from AFM pull-off force measurements.
- The DEM model was implemented in a powder recoating simulation. It was found that the cohesive forces had a large impact on powder bed properties.

6.2 Future Work

One of the largest barriers to conducting SLM research is having a means to do so. Many experimentalists resort to purchasing commercial platforms for research. As part of this thesis, the powder recoating system for an SLM testbed was designed and tested. A great degree of control over SLM processing parameters is enabled by building an academic research platform. A greater degree of control over powder recoating is enabled with the custom built, instrumented powder recoater. Each one of the capabilities of the recoater offer an interesting avenue of research. The influence of compaction force, blade height, blade vibration and blade geometry can be studied. Furthermore, the dynamic forces of the recoating process can be measured to gain a greater understanding of the mechanics of the process and enhance DEM model calibration.

The computational work also opens new research possibilities. Previous models have not considered the cohesive forces between particles. The computational work demonstrates the importance of cohesion and a means to incorporate cohesion into a model. The work allows higher fidelity models to be created and allows researchers to discover how the effects of cohesion can be overcome.

The process of powder bed fusion additive manufacturing promises to be a revolutionary technology. Powder recoating research will help to accelerate the process by furthering the research communities understanding of SLM.

REFERENCES

[1] I. Gibson, D. W. Rosen, B. Stucker, and others, *Additive manufacturing technologies*. 2010.

[2] "3D Printing Transforms the Economics of Manufacturing," *The Economist*, 2017.

[3] V. Kinzburskiy, "GT2016-56084 Central Institute of Aviation Motors," pp. 1–7, 2016.

[4] W. E. Frazier, "Metal additive manufacturing: A review," *Journal of Materials Engineering and Performance*. 2014.

[5] W. King, A. T. Anderson, R. M. Ferencz, N. E. Hodge, C. Kamath, and S. A. Khairallah, "Overview of modelling and simulation of metal powder bed fusion process at Lawrence Livermore National Laboratory," *Mater. Sci. Technol.*, vol. 31, no. 8, pp. 957–968, 2015.

[6] I. Yadroitsev, A. Gusarov, I. Yadroitsava, and I. Smurov, "Single track formation in selective laser melting of metal powders," *J. Mater. Process. Technol.*, vol. 210, no. 12, pp. 1624–1631, 2010.

[7] M. Seifi, A. Salem, J. Beuth, O. Harrysson, and J. J. Lewandowski, "Overview of Materials Qualification Needs for Metal Additive Manufacturing," *Jom*, vol. 68, no. 3, pp. 747–764, 2016.

[8] H. Gong, D. Christiansen, J. Beuth, and J. J. Lewandowski, "Melt Pool Characterization for Selective Laser Melting of Ti-6Al-4V Pre-alloyed Powder," *Solid Free. Fabr. Symp.*, pp. 256–267, 2014.

[9] B. K. Foster, E. W. Reutzel, A. R. Nassar, B. T. Hall, S. W. Brown, and C. J. Dickman, "Optical, layerwise monitoring of powder bed fusion," *Solid Free. Fabr. Proc.*, pp. 295–307, 2015.

[10] J. H. Tan, W. L. E. Wong, and K. W. Dalgarno, "An overview of powder granulometry on feedstock and part performance in the selective laser melting process," *Addit. Manuf.*, vol. 18, pp. 228–255, 2017.

[11] A. Gebhardt, "Understanding Additive Manufacturing Rapid Prototyping - Rapid Tooling - Rapid Manufacturing," *Carl Hanser, München*, p. 591, 2012.

[12] S. Baker, “Design and Fabrication of an Open-Architecture Selective Laser Melting System,” MIT, 2016.

[13] A. T. Sutton, C. S. Kriewall, M. C. Leu, and J. W. Newkirk, “Powders for Additive Manufacturing Processes: Characterization Techniques and Effects on Part Properties,” *Solid Free. Fabr. Proc.*, pp. 1004–1030, 2016.

[14] S. Meteyer, X. Xu, N. Perry, and Y. F. Zhao, “Energy and material flow analysis of binder-jetting additive manufacturing processes,” *Procedia CIRP*, vol. 15, pp. 19–25, 2014.

[15] C. Meier, R. W. Penny, Y. Zou, J. S. Gibbs, and A. J. Hart, “Thermophysical Phenomena in Metal Additive Manufacturing by Selective Laser Melting: Fundamentals, Modeling, Simulation and Experimentation,” pp. 1–63, 2017.

[16] H. W. Mindt, M. Megahed, N. P. Lavery, M. A. Holmes, and S. G. R. Brown, “Powder Bed Layer Characteristics: The Overseen First-Order Process Input,” *Metall. Mater. Trans. A Phys. Metall. Mater. Sci.*, vol. 47, no. 8, pp. 3811–3822, 2016.

[17] E. J. R. Parteli and T. Pöschel, “Particle-based simulation of powder application in additive manufacturing,” *Powder Technol.*, vol. 288, pp. 96–102, 2016.

[18] J. Zielinski, S. Vervoort, H.-W. Mindt, and M. Megahed, “Influence of Powder Bed Characteristics on Material Quality in Additive Manufacturing,” *BHM Berg- und Hüttenmännische Monatshefte*, vol. 162, no. 5, pp. 192–198, 2017.

[19] M. J. Matthews, G. Guss, S. A. Khairallah, A. M. Rubenchik, P. J. Depond, and W. E. King, “Denudation of metal powder layers in laser powder bed fusion processes,” *Acta Mater.*, vol. 114, pp. 33–42, 2016.

[20] G. Egger, P. E. Gygax, R. Glardon, and N. P. Karapatis, “Optimization of powder layer density in selective laser sintering,” *10th Solid Free. Fabr. Symp.*, pp. 255–263, 1999.

[21] Z. Xiang, M. Yin, Z. Deng, X. Mei, and G. Yin, “Simulation of Forming Process of Powder Bed for Additive Manufacturing,” *J. Manuf. Sci. Eng.*, vol. 138, no. 8, p. 81002, 2016.

[22] Y. S. Lee and W. Zhang, “Mesoscopic Simulation of Heat Transfer and Fluid Flow in Laser Powder Bed Additive Manufacturing,” *Int. Solid Free Form Fabr. Symp. Austin*, pp. 1154–1165, 2015.

[23] A. B. Spierings, N. Herres, and G. Levy, “Influence of the particle size distribution on surface quality and mechanical properties in AM steel parts,” *Rapid Prototyp. J.*, vol. 17, no. 3, pp. 195–202, 2011.

[24] C. Meier, R. Weissbach, J. Weinberg, W. A. Wall, and A. J. Hart, “On the Role of Cohesion and the Choice of Process Parameters in Metal Additive Manufacturing Powder Recoating,” 2018.

[25] A. Rosato, K. J. Strandburg, F. Prinz, and R. H. Swendsen, “Why the Brazil nuts are on top: Size segregation of particulate matter by shaking,” *Phys. Rev. Lett.*, vol. 58, no. 10, pp. 1038–1040, 1987.

[26] C. D. Boley, S. A. Khairallah, and A. M. Rubenchik, “Calculation of laser absorption by metal powders in additive manufacturing,” *Appl. Opt.*, vol. 54, no. 9, p. 2477, 2015.

[27] J. Dawes, R. Bowerman, and R. Trepleton, “Introduction to the Additive Manufacturing Powder Metallurgy Supply Chain,” *Johnson Matthey Technol. Rev.*, vol. 59, no. 3, pp. 243–256, 2015.

[28] B. Al-Mangour, *Powder Metallurgy of Stainless Steel: State-of-the Art, Challenges, and Development*, no. January 2015. 2015.

[29] L. V. M. Antony and R. G. Reddy, “Processes for production of high-purity metal powders,” *Jom*, vol. 55, no. 3, pp. 14–18, 2003.

[30] C. T. Schade, T. F. Murphy, and C. Walton, “Development of atomized powders for additive manufacturing,” *World Congr. Powder Metall. Part. Mater. PM 2014, May 18, 2014 - May 22, 2014*, pp. 215–226, 2014.

[31] Metal Powder Industries Federation, “Making Metal Powder.”

[32] D. Gu, Z. Wang, Y. Shen, Q. Li, and Y. Li, “In-situ TiC particle reinforced Ti-Al matrix composites: Powder preparation by mechanical alloying and Selective Laser Melting behavior,” *Appl. Surf. Sci.*, vol. 255, no. 22, pp. 9230–9240, 2009.

[33] R. Li, Y. Shi, Z. Wang, L. Wang, J. Liu, and W. Jiang, “Densification behavior of gas and water atomized 316L stainless steel powder during selective laser melting,” *Appl. Surf. Sci.*, vol. 256, no. 13, pp. 4350–4356, 2010.

[34] B. Van Der Schueren and J. P. Kruth, “Powder deposition in selective metal powder sintering,” *Rapid Prototyp. J.*, vol. 1, no. 3, pp. 23–31, 1995.

[35] P. Bidare, R. R. J. Maier, R. J. Beck, J. D. Shephard, and A. J. Moore, “An open-architecture metal powder bed fusion system for in-situ process measurements,” *Addit. Manuf.*, vol. 16, pp. 177–185, 2017.

[36] DMG MORI, “LaserTec 30 SLM.” [Online]. Available: https://us.dmgmori.com/products/machines/advanced-technology/additive-manufacturing/powder-bed/lasertec-30-slm.

[37] N. K. Roy and M. A. Cullinan, “μ-SLS of Metals: Design of the powder spreader, powder bed actuators and optics for the system,” *Solid Free. Fabr. Symp.*, pp. 134–155, 2015.

[38] H. Exner and A. Streek, “High resolution laser micro sintering / melting using q-switched and high brilliant laser radiation,” no. January 2017, p. 93530P, 2015.

[39] E. B. Herbold, O. Walton, and M. A. Homel, “Simulation of Powder Layer Deposition in Additive Manufacturing Processes Using the Discrete Element Method,” 2015.

[40] S. Haeri, Y. Wang, O. Ghita, and J. Sun, “Discrete element simulation and experimental study of powder spreading process in additive manufacturing,” *Powder Technol.*, vol. 306, pp. 45–54, 2017.

[41] S. Haeri, “Optimisation of blade type spreaders for powder bed preparation in Additive Manufacturing using DEM simulations,” *Powder Technol.*, vol. 321, pp. 94–104, 2017.

[42] Y. Y. Sun, S. Gulizia, C. H. Oh, C. Doblin, Y. F. Yang, and M. Qian, “Manipulation and Characterization of a Novel Titanium Powder Precursor for Additive Manufacturing Applications,” *Jom*, vol. 67, no. 3, pp. 564–572, 2015.

[43] M. Grasso and B. M. Colosimo, “Process defects and in situ monitoring methods in metal powder bed fusion: A review,” *Meas. Sci. Technol.*, vol. 28, no. 4, p. aa5c4f, 2017.

[44] T. Fey *et al.*, “Mechanical and electrical strain response of a piezoelectric auxetic PZT lattice structure,” *Smart Mater. Struct.*, vol. 25, no. 1, 2015.

[45] A. Slocum, *Precision Machine Design*. Society of Manufacturing, 1992.

[46] J. Wu, S. Cai, J. Cui, and J. Tan, “A generalized analytical compliance model for cartwheel

flexure hinges," *Rev. Sci. Instrum.*, vol. 86, no. 10, 2015.

[47] S.-M. Y. Hong-Wen Maa,∗ and Z. Z. Li-QuanWanga, "Analysis of the displacement amplification ratio of brige-type flexure hinge," *Mech. Mach. Theory*, vol. 87, pp. 45–56, 2006.

[48] E. Y. A. Wornyoh, V. K. Jasti, and C. Fred Higgs, "A Review of Dry Particulate Lubrication: Powder and Granular Materials," *J. Tribol.*, vol. 129, no. 2, p. 438, 2007.

[49] Electronics Tutorial, "Wheatstone Bridge Circuit." [Online]. Available: https://www.electronics-tutorials.ws/.

[50] OMAX, "OMAX MicroMAX JetMachining Center." [Online]. Available: omax.com.

[51] K. Uchino, "Ceramic actuators principles and applications," *MRS Bull.*, vol. 18, no. 4, pp. 42–48, 1993.

[52] Synthesos, "TinyG-Affordable Industrial Grade Motion Control," 2017. [Online]. Available: https://github.com/synthetos/TinyG/.

[53] J. H. Kim, S. H. Kim, and Y. K. Kwaka, "Development of a piezoelectric actuator using a three-dimensional bridge-type hinge mechanism," *Rev. Sci. Instrum.*, vol. 74, no. 5, pp. 2918–2924, 2003.

[54] Thorlabs, "Discrete Piezoelectric Stacks," 2018. [Online]. Available: https://www.thorlabs.com/newgrouppage9.cfm?objectgroup_id=8040.

[55] H. J. Lee, H. C. Kim, H. Y. Kim, and D. G. Gweon, "Optimal design and experiment of a three-axis out-of-plane nano positioning stage using a new compact bridge-type displacement amplifier," *Rev. Sci. Instrum.*, vol. 84, no. 11, 2013.

[56] Y. K. Yong, S. O. R. Moheimani, B. J. Kenton, and K. K. Leang, "Invited Review Article: High-speed flexure-guided nanopositioning: Mechanical design and control issues," *Rev. Sci. Instrum.*, vol. 83, no. 12, p. 121101, 2012.

[57] T. Craeghs, S. Clijsters, E. Yasa, and J.-P. Kruth, "Online quality control of selective laser melting," *Solid Free. Fabr. Proc.*, pp. 212–226, 2011.

[58] G. Jacob, A. Donmez, J. Slotwinski, and S. Moylan, "Measurement of powder bed density in powder bed fusion additive manufacturing processes," *Meas. Sci. Technol.*, vol. 27, no.

11, 2018.

[59] B. Liu, R. Wildman, C. Tuck, I. Ashcroft, and R. Hague, “Investigation the Effect of Particle Size Distribution on Processing Parameters Optimisation in Selective Laser Melting Process,” *Sff*, no. mm, pp. 227–238, 2011.

[60] C. H. Rycroft, K. Kamrin, and M. Z. Bazant, “Assessing continuum postulates in simulations of granular flow,” *J. Mech. Phys. Solids*, vol. 57, no. 5, pp. 828–839, 2009.

[61] J. Ghaboussi and R. Barbosa, “Three- dimensional discrete element method for granular materials,” *Int. J. Numer. Anal. Methods Geomech.*, vol. 14, no. 7, pp. 451–472, 1990.

[62] N. Fehn, “Diskrete-Element-Methoden fur die Partikelkontakt-Simulation,” Technical University of Munich, 2014.

[63] R. L. Brown and J. C. Richards, “Kinematics of the flow of dry powders and bulk solids,” *Rheol. Acta*, vol. 4, no. 3, pp. 153–165, 1965.

[64] L. O. Heim, S. Ecke, M. Preuss, and H. J. Butt, “Adhesion forces between individual gold and polystyrene particles,” *J. Adhes. Sci. Technol.*, vol. 16, no. 7, pp. 829–843, 2002.

[65] K. K. Rao and P. R. Nott, *An introduction to granular flow*, vol. 9780521571. 2008.

[66] O. R. Walton, “Review of adhesion fundamentals for micron-scale particles,” *KONA Powder Part. J.*, vol. 26, no. March, pp. 129–141, 2008.

[67] E. M. Lifshitz, “The Theory of Molecular Attractive Forces between Solids,” *Soviet Physics*, vol. 2, no. 1. pp. 73–83, 1956.

[68] R. Weißbach, “Modeling and Simulation of the Recoating Process in Powder Bed Metal Additive Manufacturing Reimar Weißbach,” Technical University of Munich, 2017.

[69] X. P. Li, K. M. O’Donnell, and T. B. Sercombe, “Selective laser melting of Al-12Si alloy: Enhanced densification via powder drying,” *Addit. Manuf.*, vol. 10, pp. 10–14, 2016.

[70] AP&C, “Titanium Alloy Powders.” [Online]. Available: http://advancedpowders.com.

[71] Y. Zou, “MechanoSynthesis Correspondence.”

[72] J. Drelich, “Adhesion forces measured between particles and substrates with nano-roughness,” *Minerals & Metallurgical Processing*, vol. 23, no. 4. p. 226, 2006.

[73] C. Meier, R. Weissbach, J. Weinberg, W. A. Wall, and A. J. Hart, “Modeling and Characterization of Cohesion in Fine Metal Powders with a Focus on Additive Manufacturing Process Simulations,” *Submitt. Publ.*, pp. 1–18, 2018.

[74] Y. C. Zhou, B. H. Xu, a B. Yu, and P. Zulli, “A numerical and experimental study of the angle of repose of granular particles.,” *Powder Technol*, vol. 125, p. 45–54+, 2002.

[75] L. F. Francis, *Powder Processes*. 2016.

[76] A. Castellanos, *The relationship between attractive interparticle forces and bulk behaviour in dry and uncharged fine powders*, vol. 54, no. 4. 2005.